Universidade de Aveiro Departamento de Engenharia Mecânica
2021

Diogo Couto Heitor

Mechanical Behaviour of Aluminium Alloy Foams Modelled with X-Ray Microcomputed Tomography

Comportamento Mecânico de Espumas de Ligas de Alumínio Modeladas com Recurso a Micro-Tomografia Computorizada de Raios-X

Universidade de Aveiro Departamento de Engenharia Mecânica
2021

Diogo Couto Heitor

Mechanical Behaviour of Aluminium Alloy Foams Modelled with X-Ray Microcomputed Tomography

Comportamento Mecânico de Espumas de Ligas de Alumínio Modeladas com Recurso a Micro-Tomografia Computorizada de Raios-X

Dissertação apresentada à Universidade de Aveiro para cumprimento dos requisitos necessários à obtenção do grau de Mestre em Engenharia Mecânica, realizada sob orientação científica de Doutora Isabel Maria Alexandrino Duarte, Investigadora Auxiliar do Departamento de Engenharia Mecânica da Universidade de Aveiro, e de Prof. Doutor João Alexandre Dias de Oliveira, Professor Auxiliar do Departamento de Engenharia Mecânica da Universidade de Aveiro.

Este trabalho teve o apoio financeiro dos projetos UIDB/00481/2020 e UIDP/00481/2020 - FCT - Fundação para Ciência e Tecnologia; e CENTRO-01-0145-FEDER-022083 - Programa Operacional Regional do Centro (Centro2020), no âmbito do Acordo de Parceria Portugal 2020, através do Fundo Europeu de Desenvolvimento Regional.

o júri / the jury

presidente / president

Doutora Paula Alexandrina de Aguiar Pereira Marques
Investigadora Principal em Regime Laboral da Universidade de Aveiro

Professor Doutor Matej Vesenjak
Full Professor, University Of Maribor, Eslovénia

Prof. Doutor João Alexandre Dias de Oliveira
Professor Auxiliar da Universidade de Aveiro (co-orientador)

agradecimentos / acknowledgements

À Doutora Isabel Maria Alexandrino Duarte e ao Prof. Doutor João Alexandre Dias de Oliveira por todo o apoio fornecido durante a elaboração desta dissertação. Mostraram-se sempre disponíveis apesar das condições de pandemia global. A sua vontade de ajudar e de elevar o meu trabalho transpareceram sempre. São, com toda a certeza, exemplos para mim tanto a nível profissional como a nível pessoal.

À minha família, Angelina, Joaquim e Ana Rita, por me ajudarem a atingir todos os meus objetivos, com muita paciência. São das pessoas mais importantes para mim e um dos motivos pelos quais sou a pessoa que sou hoje.

À Camila por ser uma pessoa forte, justa e por estar sempre presente na minha vida. Dá-me todos os dias força para me esforçar e ser uma melhor pessoa.

A todos os amigos e colegas que conheci durante o meu percurso académico, seja na Universidade de Aveiro ou na Technische Universität Hamburg.

Ao meu Tio, António Heitor, por ser uma pessoa exemplar e muito divertida. Ficará sempre na memória de todos.

keywords Aluminium Alloy Foams, Geometrical and Mechanical Characterization, X-Ray Microcomputed Tomography, Finite Elements Method, Segmentation

abstract In recent years, there has been an increase in interest in cellular materials for structural applications, especially cellular metals (e.g., metal foams made of aluminium and its alloys). These closed-cell and open-cell foams usually have complex cellular structures resulting from the foaming process and their mechanical properties are governed by their cellular structures and by the properties of the base material. However, their mechanical characterization is difficult and most of the times can result in the destruction of the foam specimen. In this study, X-ray microcomputed tomography (μCT) was used together with finite element modelling to develop numerical models to estimate the elastic moduli and evaluate the effects of processing of the information obtained with the μCT scans in the final results. Such a technique complements experimental testing and brings great versatility. In order to accomplish this task, different thresholding techniques (segmentation) were applied to the 2D slices, which are the result of μCT scans, with special focus on a manual global technique with the mass as a quality indicator. Then, some reconstruction algorithms (e.g. Marching Cubes 33) were used to create 3D tessellated models in the STL format, which were oversampled (excessive number of faces) and with errors. Therefore, a simplification/clean-up procedure was applied to solve those issues, being analysed in terms of mass maintenance, shape maintenance with the Hausdorff algorithm and face quality, i.e., face aspect ratio. Two different procedures were evaluated, with and without small structural imperfections, so that the impact of the procedures could be analysed as well as the effect of the presence of small defects. The results obtained were evaluated and compared to several analytical and theoretical models, models based on representative unit-cells and experimental results in terms of the relation between the relative density and the relative Young's modulus. Results demonstrated that the developed procedures were very good at minimizing changes in mass and shape of the geometries while providing good face quality, i.e., face aspect ratio. The models were also shown to be able to predict the properties of metallic foams in accordance with the findings of other researchers. In addition, the process of obtaining the models and the presence of small structural imperfections were shown to have a great impact on the final results.

palavras-chave

Espumas de Ligas de Alumínio, Caracterização Mecânica e Geométrica, Micro-Tomografia Computorizada de Raios-X, Método dos Elementos Finitos, Segmentação

resumo

Nos últimos anos, tem-se verificado um aumento do interesse na área dos materiais celulares, mais especificamente metais celulares, para aplicações estruturais (por exemplo, espumas metálicas de alumínios e as suas ligas). Estas espumas de célula aberta e fechada têm, normalmente, uma estrutura celular complexa resultante do processo de espumação e as suas propriedades mecânicas dependem das suas estruturas celulares e das propriedades do material base. No entanto, a caracterização mecânicas destes materiais é díficil e resulta, regularmente, na destruição dos specimens de espuma. Neste estudo, Micro-Tomografia Computorizada de Raios-X (μCT) foi aplicada juntamente com modelação por elementos finitos para desenvolver modelos númericos que conseguem estimar os módulos de elasticidade e avaliar os efeitos do processamento da informação obtida pelos scans de μCT nos resultados finais. Esta técnica complementa os procedimentos experimentais e traz uma grande versatilidade. Para se completar a tarefa proposta, diferentes métodos de segmentação foram aplicados às fatias 2D, que são resultantes dos scans de μCT, com especial atenção num método de segmentação manual global que utiliza a massa como indicador de qualidade. Depois disso, alguns algoritmos de reconstrução, por exemplo, Marching Cubes 33, foram aplicados para criar modelos 3D de faces triangulares no formato STL que demonstram sobreamostragem (excessiva quantidade de faces) e alguns erros. Por essa razão, um procedimento de simplificação/limpeza foi aplicado para resolver estes problemas, sendo analisados em termos de preservação de massa, preservação de forma com o algoritmo de Hausdorff e qualidade das faces, ou seja, razão de proporção. Dois procedimentos diferentes foram avaliados, um com e outro sem pequenos defeitos estruturais para que se consiga analisar não só o impacto do processamento dos modelos assim como o efeito da presença de pequenos defeitos. Os resultados obtidos foram comparados com vários modelos analíticos e teóricos, modelos baseados em células unitárias representativas e resultados experimentais com base na relação entre a densidade relativa e o módulo de Young relativo. Os resultados demonstraram que os procedimentos desenvolvidos são bons a preservar a massa e forma das geometrias deixando as faces com boa qualidade. Verificou-se também que os modelos foram capazes de prever as propriedades das espumas metálicas em concordância com o trabalho de outros investigadores. Adicionalmente, mostrou-se que o processo de obtenção dos modelos e a presença de pequenas imperfeições estruturais tem um impacto relevante nos resultados finais.

Contents

I Introduction and Background **1**

1 Framework **3**
1.1 Introduction . . . 3
1.2 Objectives . . . 4
1.3 Overview . . . 5

2 Aluminium Foams **7**
2.1 Foam Properties . . . 8
2.1.1 Mechanical Properties . . . 10
2.1.1.1 Linear Elasticity . . . 11
2.1.1.2 Plastic Collapse and Plateau Region . . . 11
2.1.1.3 Densification and Failure Mechanisms . . . 12

II Development of X-Ray Microtomography based Model **13**

3 X-Ray Microcomputed tomography and 2D Slice Analysis **15**
3.1 X-Ray Microcomputed tomography . . . 15
3.1.1 Foam Specimens . . . 16
3.2 Images as Discrete Functions . . . 19
3.2.1 Region/Volume of Interest . . . 20
3.2.2 Thresholding Techniques . . . 20
3.2.2.1 Otsu Thresholding Technique . . . 22
3.2.2.2 Adaptive Thresholding Techniques . . . 22
3.2.2.3 Global Manual Thresholding Technique . . . 23
3.2.2.4 Results . . . 25
3.2.3 Morphological Operations . . . 27
3.2.3.1 Closing Operation . . . 28
3.2.4 Despeckle . . . 30

4 3D Geometry Simplification and Analysis **33**
4.1 STL Format . . . 34
4.1.1 Missing Faces or Gaps . . . 36
4.1.2 Degenerate Faces . . . 36
4.1.3 Overlapping Faces or Self-intersecting Faces . . . 36

4.1.4 Non-manifold Conditions . . . 36
4.2 Reconstruction Algorithms . . . 37
4.2.1 Marching Cubes 33 . . . 37
4.2.2 Double-Time Cubes . . . 37
4.2.3 Method Selection . . . 38
4.3 Main Simplification Algorithms . . . 39
4.3.1 Quadric Edge Collapse Decimation . . . 39
4.3.2 Taubin Smooth . . . 40
4.3.3 Close Holes . . . 41
4.3.4 Discrete Curvature Calculation . . . 42
4.4 Simplification Procedure . . . 43
4.4.1 Procedure 1: Plain Simplification . . . 44
4.4.2 Procedure 2: Elimination of Cell Wall Holes . . . 46
4.5 Results . . . 46
4.5.1 Mass/Volume and Surface Area . . . 47
4.5.2 Distance Between Meshes . . . 48
4.5.3 File Size . . . 53

III Numerical Modelling, Analysis and Results 55

5 Numerical Modelling and Analysis 57
5.1 Analytical Models . . . 57
5.2 FEA Meshing . . . 58
5.3 Boundary Conditions and Properties . . . 60
5.4 Mesh Refinement . . . 62
5.4.1 Cubic Open-cell Mesh Convergence Analysis . . . 62
5.4.2 Closed-cell Mesh Convergence Analysis . . . 62
5.4.2.1 Procedure 1 . . . 63
5.4.2.2 Procedure 2 . . . 64
5.5 Mechanical Behaviour and Effective Properties . . . 64
5.5.1 Open-cell Foam . . . 65
5.5.2 Closed-cell Foam . . . 66
5.5.2.1 Octants . . . 66
5.5.2.2 Influence of the Elimination of Defects . . . 67
5.5.2.3 Influence of the Closing Morphological Operation . . . 68
5.5.3 Experimental Results . . . 70
5.5.4 Representative Unit-cell Models . . . 71
5.5.5 Anisotropy Analysis . . . 73

6 Final Remarks 77
6.1 Future work . . . 79

A Complementary Information 81
A.1 Foam Production Methods . . . 81
A.1.1 Closed-cell Foam Production . . . 81

A.1.2 Open-cell Foam Production 83
A.1.3 Influence of the Production Method on Pore Distribution 83
A.2 Otsu Thresholding Technique 84
A.3 Equipment 87
A.4 Face Quality 87
A.5 Representative Unit-Cells (RUC) 88
A.6 Marching Cubes 33 88

Bibliography **89**

Intentionally blank page.

List of Tables

2.1 Cellular structure (topology) influencing parameters [24]. 10

3.1 Properties of the closed-cell (CC), cubic open-cell (Cubic OC) and cylindrical open-cell (Cylindrical OC) foam specimens made of aluminium alloys. 19
3.2 Ideal thresholds for the closed-cell foam specimen with different morphological operations. The error (%) in volume with regard to the real foam is also given. 31

4.1 Comparison between the Double-time Cubes and the Marching Cubes 33 algorithms. The error in volume with respect to the real values is provided between brackets. The error in surface area is calculated with the values obtained with *CTAn*. 38

5.1 Theoretical Models for open-cell and closed-cell foams. 58
5.2 Numerical Models for open-cell and closed-cell foams. 58
5.3 Values of Young's modulus (Pa) and Poisson's ratio in all three directions for the closed-cell foam specimen with both procedures and for the cubic open-cell foam specimen. 74

Intentionally blank page.

List of Figures

1.1 Schematic of the general procedure. 6

2.1 Closed-cell (left) and open-cell foam specimens [33, 34]. 8
2.2 Types of cellular materials [37]. 9
2.3 Stress strain curve of a metallic foam [26]. 10
2.4 Representation of an ideal unit cell (left) and of a bent unit cell (right) [38]. 12

3.1 Schematic of the X-ray microcomputed tomography (µCT) equipment and an open-cell aluminium foam (height: 20.4 mm; diameter: 18.9 mm) (a) and showing and showing raw scans/projections, segmented images, reconstructed structure, and real photo [25]. 17
3.2 One 2D slice of the closed-cell foam (left) and distorted foam which is evidence of damage to the foam (right). 18
3.3 2D slices of the closed-cell foam (a) cubic open-cell foam (b) and cylindrical open-cell foam (c) specimens. 18
3.4 Discrete digital image $\mathbf{I}(u, v)$ on an 8-bit scale [46]. 20
3.5 Example of region of interest of closed-cell foam. Corners contain some speckles that are negligible, therefore, not included. 20
3.6 Example of different threshold values for the binarization of a grey scale image of rice obtained through MATLAB (www.mathworks.com). 21
3.7 Application of the Otsu thresholding technique in 3D for the closed-cell foam specimen, which yields a threshold k of 70. 22
3.8 Application of the Mean-C technique on the 2D slices of an open-cell foam (Radius of 2 and constant of 15). Original on the left and binary after AT thresholding on the right. 24
3.9 Threshold sensitivity analysis for the cubic open-cell foam specimen. . . . 26
3.10 Threshold sensitivity analysis for the cylindrical open-cell foam specimen. 26
3.11 Threshold sensitivity analysis for the closed-cell foam specimen. 27
3.12 Structuring elements. Dots are 1's, empty spaces are 0's, red spot is the pixel in study. (a) N4; (b) N8 [46]. 28
3.13 Example of dilation (a) and erosion (b) [46]. 29
3.14 Sensitivity Analysis for different radii of the structuring element. 30
3.15 Ideal threshold with no morphological operation (left) and ideal threshold for a morphological operation of radius 6 (0.09 mm) (right) for the closed-cell foam specimen. 31

4.1 Conversion of binary slices to fully processed 3D model. 34
4.2 Orientation of a face (left) and vertex-to-vertex rule (right). 35
4.3 Overlapping faces or self-intersecting faces [55]. 36

4.4 Non-manifold conditions. (a) Edge; (b) Face; (c) Point (vertex) [55]. . . . 37
4.5 Edge Collapse [62]. . . . 40
4.6 Comparison of surface quality before (left) and after smoothing (right) for the closed-cell foam specimen. Histograms bars are adjusted to a max size. . . . 41
4.7 (a) First face generated. (b) Second face generated. (c) Third face generated. (d) Fourth face generated [55]. . . . 42
4.8 Procedure pipeline. The step represented in red is only added for Procedure 2 (clean small defects and cracks). . . . 45
4.9 Procedure 1 with defects (Left) and Procedure 2 without defects (Right). 47
4.10 Error of the volume and surface area with respect to the density of faces for the closed-cell foam (left) and the cubic open-cell foam (right). . . . 48
4.11 Mean of the two-sided Hausdorff distance of the cut closed-cell foam (left) and of the cubic open-cell foam (right) plotted with respect to the face density. . . . 50
4.12 Visual representation of the Hausdorff distance of the cut closed-cell foam with 500 thousand faces, i.e., 286 faces per mm^3 and a 99% reduction. . . 50
4.13 Visual representation of the Hausdorff distance of the cubic open-cell foam with 500 thousand faces, i.e., 50 faces per mm^3 and a 98% reduction. . . . 51
4.14 Distance from reference mesh of the cut closed-cell foam (left) and of the cubic open-cell foam (right) plotted with respect to the face density. . . . 52
4.15 Visual representation of the distance from a reference mesh of the cut closed-cell foam with 500 thousand faces, i.e., 286 faces per mm^3 and a 99% reduction. . . . 52
4.16 Visual representation of the distance from a reference mesh of the cubic open-cell foam with 500 thousand faces, i.e., 286 faces per mm^3 and a 99% reduction. . . . 53
4.17 File size and face density of the open-cell foam and the closed-cell foam. . 53

5.1 Input and Analysis paths. . . . 59
5.2 2D representation of the SID boundary conditions [20]. . . . 61
5.3 Convergence analysis of the error of the Young's modulus for the cubic open-cell foam. . . . 63
5.4 Convergence analysis of the error of the Young's modulus for the closed-cell foam prepared with Procedure 1. . . . 64
5.5 Convergence analysis of the error of the Young's modulus for the closed-cell foam prepared with Procedure 2 (No defects) compared with Procedure 1. . . . 65
5.6 Relative Young's modulus for the cubic open-cell foam for an imposed displacement with symmetry boundary conditions. . . . 66
5.7 Stress distribution (Equivalent Von Mises) for the cubic open-cell foam for a compression analysis. . . . 67
5.8 Relative Young's modulus for the closed-cell foam and the different octants. 68
5.9 Relative Young's modulus for closed-cell foam prepared with Procedure 1 (defects) and Procedure 2 (no defects). . . . 69

5.10 Stress distribution (Equivalent Von Mises) for the closed-cell foam for a compression analysis. Procedure 1 (plain simplification) on the left and Procedure 2 (no defects) on the right. 69
5.11 Analysis of the Young's Modulus with respect to the radius of the closing operation. 70
5.12 Relative Young's modulus of closed-cell foam models and experimental results [68, 94, 95]. 71
5.13 Relative Young's modulus of open-cell foam models and experimental results [26]. 72
5.14 Relative Young's modulus of closed-cell foam μCT based models and RUC models [19, 96]. 73
5.15 Relative Young's modulus of open-cell foam μCT based models and RUC models [19, 96]. 74
5.16 3D Anisotropy maps for (a) the closed-cell foam specimen with Procedure 1, (b) the closed-cell foam specimen with Procedure 2 and (c) the cubic open-cell foam specimen. 75

A.1 Schematic of commercially relevant production methods of metal foams including trade names and companies [1]. 82
A.2 Indirect foaming or powder metallurgy methods [102]. 83
A.3 Exemplary images of the different foams' classes, which illustrate the level of order and structural control [30]. a) Alporas foam; b) P-MSF foam; c) APM foam; d) M-Pore foam; e) Structwire; Additevely manufactured 3D lattice structure. 85
A.4 SkyScan 1275 (Bruker μCT, Belgium) from TEMA. 87
A.5 Measurements for the quality factor [65]. 88
A.6 Different types of representative unit-cells. 88
A.7 Marching Cubes grid [57]. 89
A.8 Original look up table on the left (MC) and new MC33 look up table on the right [17]. 90

Intentionally blank page.

Part I

Introduction and Background

Chapter 1

Framework

1.1 Introduction

In the past few years, there's been an increase in interest in the field of cellular materials due to their interesting properties and low weight, for example, cork and wood, polymeric foams and metal foams. They can be produced and altered to satisfy certain requirements and can perform well in different types of applications and scenarios, for example, structural support, sound isolation, as heat exchangers, etc [1, 2]. In this dissertation, the focus is in the specific branch of metal foams (aluminium alloy foams) and their mechanical properties and structural applications.

There have been some attempts to include aluminium alloy foams in mechanical design, such as crash-absorbing elements in vehicles, parts for milling machines and train prototypes, all taking advantage of the strength-to-weight ratio of the foams and their ability to absorb energy. Nevertheless, these are just the initial steps in the introduction of this type of material in the industry, seeing that their production is usually inconsistent, to an extent. The final properties depend on the internal cellular structure which, in turn depend greatly on the manufacturing. The conventional methods (direct and indirect foaming methods) are usually used to prepare stochastic foams, i.e., foams with a random cell distribution, but new technologies (e.g., 3D printing) can already produce periodic cellular structures [1, 3, 4]. Here, the focus is on stochastic foams with both closed cells (no or minimal connectivity between pores) and open cells (interconnected pores). Due to their random and imperfect nature, small defects, small holes and cracks are very likely to form, which can cause significant changes to the strength of the material and render it useless for some applications. Therefore, the characterization of aluminium alloy foams takes on great importance for scientists and engineers all over the world, specially to try to reduce their unpredictability and risk.

Generally, the characterization of metallic foams is done using experimental compression analyses, in which a specimen of a foam is compressed and its properties are extrapolated, but it is an expensive process and each specimen is destroyed and can no longer be used. As a result, many analytical models and models based on Representative Unit-Cells (RUC) have been developed to predict the mechanical behaviour of cellular solids [5]. However, they are just approximations, are usually periodic and don't take micro-defects and small cracks into consideration. So, in this dissertation, X-ray Microcomputed Tomography (μCT) scans are used to evaluate the mechanical properties of aluminium alloy foams, with special emphasis on the Young's modulus, which bring

much more detail and result, in theory, in a more exact analysis. These sorts of methods are commonly used in the medical industry and are being introduced in the field of cellular materials, despite the research on the topic still being limited and there being little standardization [6–14]. The scans are performed in a μCT machine. It outputs several 2D projection images of the specimen in study, which are later used to create 2D reconstructed images (slices). These images must then be analysed and go through a process of segmentation (thresholding/binarization), for example, either applying the Otsu method, adaptive methods or even manually selecting values based on the mass of the real specimen [15, 16]. This is one of the main topics of this dissertation with special emphasis on the latter, which has the distinguishing factor with regards to work done by other authors. Due to limitations regarding national/world health, i.e., COVID-19 pandemic, the scans were not performed personally, the 2D reconstructed images were directly provided by other authors/colleagues.

Using the 2D slices, the 3D geometry can be reconstructed using, for example, the Marching Cubes 33 algorithm which approximates the surface of foam with a mesh of triangles (usually in a STL file) [17]. However, since the 2D slices are discrete, i.e., they are not continuous, there are always some errors and it is usually over sampled (excessive number of nodes/faces). For these reasons, it must be corrected and simplified so that it can be used in the following stages. However, the simplification procedure has a very large influence on the results. For that reason, a path of minimization of changes to the geometry is followed in order to produce more accurate results. In addition, two different procedures are tested. One that closes and corrects most defects and cracks in the cell walls of the foams and another which maintains them. The study of both procedures enables a comparison which can show the influence of the defects on the mechanical properties. To ensure the quality of the simplification procedures, the preservation of mass/volume and the preservation of the shape (Hausdorff distance algorithm [18]) of the 3D models is analysed. Lastly, the reconstructed 3D geometries can be introduced in Finite Element Method (FEM) analysis software and be subjected to different types of loading conditions [19, 20]. Unlike other methods, for instance, using theoretical/analytical models or Representative Unit Cells (RUC), the real shape of each specimen is used, which can include the small defects and the high variability of pore sizes, providing more accurate results for each specific foam, despite the much larger complexity of the process. Numerical methods, such as the ones presented in this dissertation, are a useful tool to supplement the mechanical characterization of various types of cellular metals. They can be used before experimental testing to reduce the number of specimens and experimental tests by predicting the mechanical response or after to validate computer models and reduce the number of further experimental tests. In some cases, computer simulations provide additional insight into the deformation behaviour of cellular metals since they also provide data for material points inside the specimens. In the end, the results can then be compared to real foams and other methods, giving insight on the process itself and its usefulness in the field of cellular solids.

1.2 Objectives

The first main of objective of this work is to develop and analyse a numerical model that predicts the mechanical behaviour of aluminium alloy foams from real images collected

with an X-Ray μCT scanner. The second is to evaluate the influence of the processing of the images given by the scans and of the reconstruction and simplification of the 3D models on the results. Such processes are complex and involve many small steps which can have a great impact on the results. For this reason, the necessity of process standardization is also discussed. In order to achieve the main goals and clarify the process, the following specific tasks were defined:

1. Study X-ray Microtomography and the main involved parameters;
2. Evaluate different methods of image thresholding/segmentation (binarization) and their effects;
3. Develop and implement a quality indicator based on the mass/volume of a specimen for the thresholding;
4. Study the process of cleaning the 2D reconstructed images (slices);
5. Analyse the different 3D reconstruction algorithms based on images/point clouds;
6. Develop simplification procedures for the 3D models which can reduce their computational requirements while maintaining their shape and correcting errors;
7. Study the finite element meshing of 3D models based on boundary meshes in the STL format;
8. Develop a numerical model with the obtained 3D models;
9. Evaluate the impact of the presence of small defects and cracks in the 3D models;
10. Evaluate and compare results with other numerical/analytical models and experimental results.

1.3 Overview

The proposed methods in the following chapters present solutions to obtain models based on μCT scans from the beginning of the scans until the results for two types of aluminium alloy foams: open-cell; and closed-cell. They are based on the work of Sharma et al. but with a deeper focus on the procedures themselves and how they affect the results [7]. In addition, the structural properties are analysed elastically. The main focus is the characterization of the effective properties, such as the Young's modulus, with respect to the relative density.

Figure 1.1 represents the workflow and structure of the document. Three distinct parts can be observed in it, which are preceded by an introduction to metallic foams in Chapter 2: 2D Slice/Image Acquisition and Processing; 3D Geometry Simplification and Analysis; and Numerical Modelling and Analysis. In Chapter 3, a foam specimen is scanned using a μCT device, which provides raw 8-bit, i.e., grey scale, 2D projection images[1]. Then, they are used to obtain the 2D slices/images, also in 8-bit and several intensities of grey, which represent the entire structure of the foam in a layered format.

[1]This step is not included in Fig. 1.1 because it was performed by the colleagues which provided the 2D slices.

The slices are submitted to segmentation/thresholding methods to determine what is part of the background and what is part of the foam itself. Several methods are tested and compared, and the mass is used as a quality indicator to ensure that the final geometry is similar to reality. These methods output the same slices but now in binary (black and white). Then, several operations could be applied which clean the 2D slices, i.e., make them smoother and eliminate small defects and speckles, such as morphological operations and the despeckle operation. However, they are not mandatory and their application might be reserved to some special cases.

In Chapter 4, the focus is the creation, analysis and processing of the 3D tessellated models. Firstly, the binary slices must be introduced in a surface reconstruction algorithm. In this case, the Marching Cubes 33 (MC33) and Double-Time Cubes (DTC) are discussed. After the reconstruction, the virtual foam, which is in the STL format, must be simplified and corrected. This is one of the most important and difficult steps of the process. There are many algorithms which could be applied in different ways, therefore, making the selection of the most relevant ones a difficult task. In addition, with the purpose of analysing the effect of the process on the final results, two different procedures for processing the foams are studied. One which eliminates (almost) all defects/cracks on the model and another which leaves them as is. The quality of the simplification is tested in terms of mass preservation and shape preservation (Hausdorff algorithm).

Lastly, Chapter 5 is focused around the numerical modelling of the obtained structures and their analysis. First, the STL files which contain the foam models are meshed for Finite Element Analysis (FEA). Afterwards, the boundary conditions are defined in accordance with the intended purpose. Finally, the mesh refinement is analysed and the final tests are performed. At this point, the numerical results have been obtained and they can be evaluated and compared.

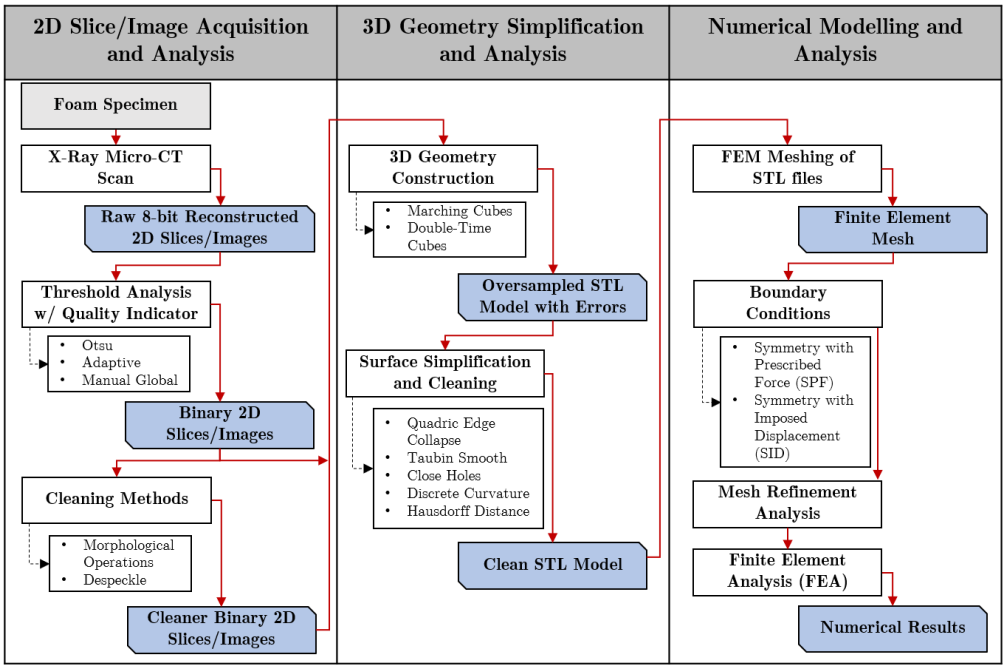

Figure 1.1: Schematic of the general procedure.

Chapter 2

Aluminium Foams

Metal foams are lightweight cellular structures inspired by naturally occurring arrangements such as wood, bones and sea sponges [21]. These natural cellular materials are light, but simultaneously exhibit remarkable properties for engineering applications, for instance, the bone, which shows low density or weight and high strength, and cork, which has good thermal isolation. In fact, such characteristics have influenced and inspired scientists to develop similar artificial, man-made cellular materials. The development of this type of structure enables, today, their usage in a wide range of industrial, commercial, biomedical and military applications, providing significant contributes in weight reduction and material savings as well as excellent performance in vibration damping, sound attenuation, energy absorption, good filtration capability, catalytic properties and insulation [1, 2, 5, 22, 23]. Moreover, cellular metals have a high stiffness-to-weight ratio and are non-flammable and recyclable, very important characteristics regarding safety and sustainability [24].

These materials are constituted by an interconnected porous network of solid struts and plates, which form the edges and faces of the pores/cells, and have a porosity greater than 70% [25]. In the case of aluminium alloy cellular materials, or aluminium foams, the main phase (matrix) is continuous, solid and constituted by the alloy, while the cells are gaseous (air) and discontinuous or continuous, depending on the cell type. In the literature, some of these materials are designated differently, for example, "sponge" or "foam". Nevertheless, the term foam is preferred here. It relates to a specific type of porous material which is produced through the solidification of a liquid foam, in which bubbles are dispersed [2]. In addition to the natural versus artificial classification, cellular materials can be further categorized by cell type, cell size, variability in cell size (stochastic or periodic) and porosity. With regards to the cell type, there are two main categories: open-cell and closed-cell, which correspond to the inter-connectivity between pores or isolation from each other by cell walls, respectively (Fig. 2.1) [26]. There is a clear distinction for the kind of application suited to each type of foam. The open-cell foams have very good functional properties and are widely used as filters, electrodes, heat exchangers and biomedical implants. Closed-cell foams, specially made of metal, have interesting properties for structural applications where high efficiency or energy absorption under impact or sound, together with noise and vibration damping, are required. Some examples are trains, cars, aircrafts, and equipment [1, 25, 27, 28]. Another important topic is the variability in cell sizes, i.e., the size of pores, which can be divided into two groups: stochastic, referring to a random distribution of sizes, and

periodic foams, which are regular and characterized by a unit cell. The first group, which is the focus of this dissertation, includes foams which are very irregular and have small imperfections, making them harder to characterize, for example, open-cell or closed-cell foams. In contrast, periodic foams, such as lattice truss and prismatic structures, are very predictable and have been made possible because of more advanced production methods, for instance, 3D printing [29–31]. Furthermore, the syntactic foam type is a new recent cellular material which stands in the middle ground between the two mentioned above. It is produced with the incorporation of hollow spheres into the matrix, making it a pseudo-stochastic foam with an easily reproducible unit cell [32]. Reinforced foams are also becoming more relevant, combining stochastic foams and polymers or with the introduction of nanoparticles to create composite and nanocomposite foams (Fig. 2.2).

Figure 2.1: Closed-cell (left) and open-cell foam specimens [33, 34].

In the case of stochastic open and closed-cell foams, several production methods could be considered, however, only a few are commercially viable at the moment. Investment casting is commonly used to produce open-cell foams by taking advantage of polymeric foams as a "mould". In contrast, closed-cell foams are produced by a direct method, namely melt metallurgy, which uses molten metal and ceramic particles combined with the introduction of a gas to form pores, or an indirect method, particularly powder metallurgy in which metallic powder combined with a foaming agent are molten to form the final foam [34, 35]. In addition, more complex structures have been developed in the last years which involve such methods, like foam filled tubes and sandwich panels with a foam core (See Section A.1 for more information regarding the commercially relevant production methods of metal foams). They have shown to be good options for the transport industry presenting a good trade-off between weight and strength [1, 27, 28, 36].

2.1 Foam Properties

Metal foams are very complex materials with a unique set of properties which depend on three main factors [38]:

(i) the properties of the base material, in this case, aluminium;

(ii) the cellular structure, topology;

(iii) the relative density.

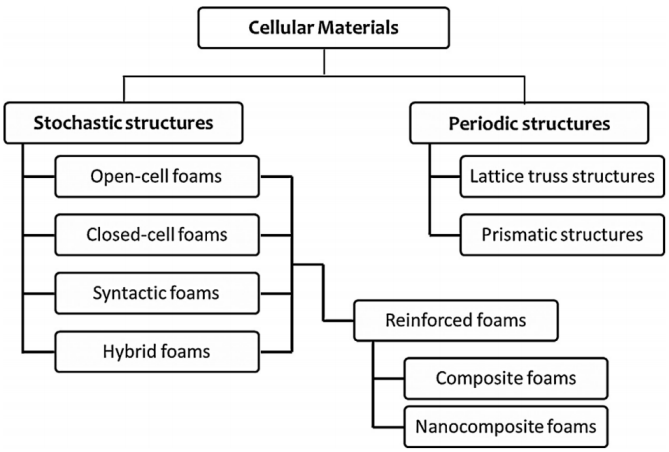

Figure 2.2: Types of cellular materials [37].

The base material gives the foams their basic properties. It has a great influence on the final behaviour of the foam in regard to stiffness, ductility, ability to absorb energy, thermal and electrical conductivities, etc. The idea is that these parameters are different when comparing a foam with the solid material, but are still quite dependant on the base material.

The cellular structure of a foam, or topology, has a great impact on its final properties. The topology analyses the cells/pores and their characteristics, the struts and cell walls, the distribution of mass along the cell walls and edges and the microstructure (micro pores and defects), many of which are greatly influenced by the production methods. It can be defined by a high amount of parameters, hence the difficulty of characterizing such materials. Out of these, some are regarded as more important and can be divided in three categories: cellular architecture, pores and metallic skeleton (Table 2.1) [5, 24].

Lastly, the relative density can be controlled with the manufacturing process and is many times used to describe other properties of the material [5]. Since an engineer cannot be expected to check the architecture of every foam in order to evaluate its characteristics, simpler methods using the relative density, $\overline{\rho}$, which is easier to calculate, were developed [19]. Therefore, it can be seen that there is a strong relation between the relative density and many properties [26]. The Young's modulus is one of those cases and is one of the main points of discussion in this document. It is one of the most important parameters and is defined as the result of the division of the foam density, ρ, by the density of the solid of the base material, ρ_s, which constitutes the walls of the cell,

$$\overline{\rho} = \frac{\rho}{\rho_s}. \tag{2.1}$$

The pore volume fraction, also known as porosity, is inversely proportional to the relative density. Therefore, the higher the relative density, the lower the porosity,

$$p = 1 - \frac{\rho}{\rho_s}. \tag{2.2}$$

Table 2.1: Cellular structure (topology) influencing parameters [24].

Cellular Architecture	**Pores**	**Metallic Skeleton**
Open-/closed-cell	Volume fraction	Cell wall thickness/length
Stochastic or periodic	Shape	Number of nodes
	Orientation	Cell wall ondulation/rugosity
	Aspect ratio	Microstructure
	Size	Defects

2.1.1 Mechanical Properties

There has been a greater focus on the usage of metal foams, particularly made of aluminium, for applications with greater mechanical requirements, due to their stiffness to weight ratios and very good energy absorption capabilities. Using foams as a filler of thin-walled structures or as a core of sandwich panels are some of the very promising applications, hence their characterization and analysis takes on greater importance [27, 28, 36]. Their behaviour is especially strong for compression scenarios but weaker for tensile and shear loading. For that reason, compression loading cases are the focus in this section. For more information regarding the official calculation of mechanical parameters of foam specimens, see norms ISO 13314:2011[1] and JIS-H-7902[2].

In a compression analysis, metal foams show a particular stress-strain curve (Fig. 2.3). This curve is divided into three main regions:

(i) the linear elastic region;

(ii) the plateau region;

(iii) the densification region.

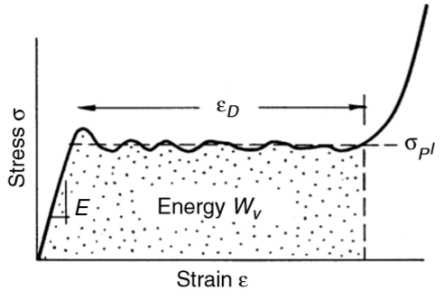

Figure 2.3: Stress strain curve of a metallic foam [26].

[1]ISO 13314:2011 Mechanical testing of metals — Ductility testing — Compression test for porous and cellular metals.

[2]JIS-H-7902 Compression Test for Porous And Cellular Metals, 2016.

2.1.1.1 Linear Elasticity

In the linear elastic region, the foam has a similar behaviour to a normal metal, i.e., it shows a linear response to applied loads and the deformation is reversible. The Young's modulus, E, and the Poisson's ratio, ν, can be inferred from this section from the slope and the relationship between the transverse strain and the compression axis' strain, respectively. Despite the representation, the initial curve is not straight and its slope is less than the true modulus. The Young's modulus (compression), E, the shear modulus, G, and Poisson's ratio, ν, scale with the density as [26]

$$\frac{E}{E_{\mathrm{s}}} \approx \alpha_2 \left(\frac{\rho}{\rho_{\mathrm{s}}}\right)^n \Leftrightarrow E \approx \alpha_2 E_{\mathrm{s}} \left(\frac{\rho}{\rho_{\mathrm{s}}}\right)^n, \tag{2.3}$$

$$\frac{G}{G_{\mathrm{s}}} \approx \alpha_2 \left(\frac{\rho}{\rho_{\mathrm{s}}}\right)^n \Leftrightarrow G \approx \alpha_2 G_{\mathrm{s}} \left(\frac{\rho}{\rho_{\mathrm{s}}}\right)^n, \tag{2.4}$$

$$\nu \approx 0.3, \tag{2.5}$$

where n has a value between 1.8 and 2.2 and α_2 between 0.1 and 4. Both depend on the structure of the foam. Moreover, the tensile modulus is typically 10% greater than for compression and anisotropy in the cell shapes can lead to significant differences, up to 30%, between moduli in different directions.

2.1.1.2 Plastic Collapse and Plateau Region

In compression, when a metal foam is loaded past its yield point, σ_{y}, it starts to collapse plastically. Initially, the cell edges and walls in weaker regions buckle and lead to early plastic deformation or fracture, followed by complete plasticization of the structure. Plastic collapse gives a long horizontal plateau to the stress-strain curve at the plateau stress, σ_{pl}, in which the deformation is no longer reversible. In addition, regarding the failure as mentioned in the book Cellular Solids by Gibson and Ashby [5]: "the failure is localized in a band transverse to the loading direction, which propagates throughout the foam with increasing strain". On one hand, the plateau region for open-cell foams is usually long, well defined and practically horizontal. On the other, in the case of closed-cell foams, the stress can rise with increasing strain due to the enclosure of gases, membrane stresses and a more complex structure. The plateau stress, σ_{pl}, scales with density as

$$\sigma_{\mathrm{pl}} \approx (0.25 \text{ to } 0.35)\sigma_{\mathrm{y,s}} \left(\frac{\rho}{\rho_{\mathrm{s}}}\right)^m. \tag{2.6}$$

For metal foams, m lies between 1.5 and 2.0 [5,26]. The existence of a long plateau region on the stress-strain curve plays an essential role in energy absorption applications. The absorbed energy per unit volume, W_{v}, is equal to the area beneath the curve up to the densification point, so it can be expressed as

$$W_{\mathrm{v}} = \int_{\varepsilon_1}^{\varepsilon_2} \sigma(\varepsilon)\, d\varepsilon, \tag{2.7}$$

where $[\varepsilon_1, \varepsilon_2]$ is the strain interval . Perhaps more relevant for lightweight applications, e.g., transports and packaging, is the absorbed energy per unit weight, W_{w}, which can be formulated as

$$W_{\mathrm{w}} = \frac{W_{\mathrm{v}}}{\rho}. \tag{2.8}$$

2.1.1.3 Densification and Failure Mechanisms

The densification phenomenon happens at the densification strain, ε_d, defined as

$$\varepsilon_{\mathrm{d}} \approx \left(1 - \alpha_1 \frac{\rho}{\rho_{\mathrm{s}}}\right), \tag{2.9}$$

or,

$$\varepsilon_{\mathrm{d}} \approx 1 - \left(\frac{\rho}{\rho_{\mathrm{s}}}\right) / \left(\frac{\rho_{\mathrm{crit}}}{\rho_{\mathrm{s}}}\right), \tag{2.10}$$

where α_1 lies between 1.4 and 2.0 and $\rho_{\mathrm{crit}}/\rho_{\mathrm{s}} \approx 0.6$ [5,38]. At this point, the foam has been practically completely crushed and the cell walls and edges start merging, leading to an increased stiffness comparable to that of the solid material. The stress rises steeply for small strains and the structure becomes more and more compacted.

The failure of an aluminium foam is a complex phenomenon which results from its very intricate structure. For this reason, let's take the example of a unit cell of a open-cell foam as represented in Figure 2.4. The representation consists of solid struts surrounding a void space which contains a gas or fluid. Three different collapse mechanisms compete during compression and the one that requires the lowest stress dominates [5, 38]. The most significant effect in the case of aluminium foams, which is a ductile material, is bending. When a compressive stress, σ, exerts a force on the cell edges it causes them to bend as shown in Figure 2.4 leading to a bending deflection, δ. In summary, it results in

$$\frac{\sigma_{\mathrm{pl}}}{\sigma_{\mathrm{y,s}}} \propto \left(\frac{\rho}{\rho_{\mathrm{s}}}\right)^{3/2} \quad \text{(Bending-dominated behaviour).} \tag{2.11}$$

The other two failure mechanisms, buckling and fracture, are not as relevant for this type of foam. They are the main failure mechanisms when analysing elastomeric and ceramic foams, respectively. The bending-dominated behaviour is not exclusive to open-cell foams. Closed-cell foams function in a similar fashion and allow similar scaling laws, however, the cell faces carry membrane stresses when the foams are loaded. Since these faces are very thin, they buckle and rupture at low stress giving a low contribution to the overall stiffness and strength.

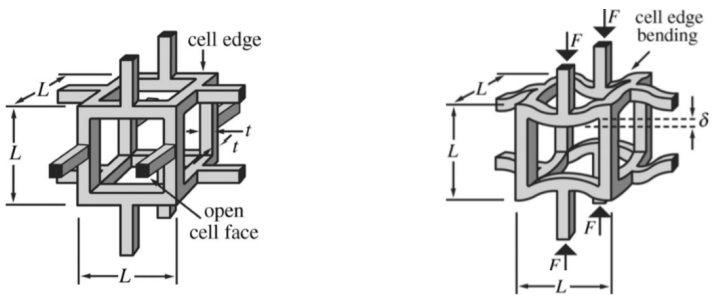

Figure 2.4: Representation of an ideal unit cell (left) and of a bent unit cell (right) [38].

Part II

Development of X-Ray Microtomography based Model

Chapter 3

X-Ray Microcomputed tomography and 2D Slice Analysis

The first stage and the base of this dissertation is the introduction of X-Ray Microcomputed Tomography (μCT) to acquire the geometries which are used to simulate and evaluate the behaviour of the foam specimens. It allows the observation and study of the microstructure of foams and their virtual 3D representation, which has been the focus of most of the available research up until now. However, its application combined with Finite Element Analyses (FEA) brings great potential and has been documented by some authors in varying degrees [7–13, 39, 40]. Through μCT scans, 2D reconstructed slices/images are obtained which represent the specimen in a layered format. Afterwards, they are processed and analysed so that they are ready to be used in 3D reconstruction algorithms in the next chapter. The process applied to the 2D slices is based on the principles of digital image analysis. It is, in general, simple to perform, however, difficulties arise when trying to establish the involved parameters so that a minimum of information is lost and the resulting 2D processed slices and the subsequent 3D geometry represent the real structure with accuracy. For this reason, a quality indicator based on the mass of each foam specimen is employed which tries to ensure the desired accuracy. The 2D slices have to be segmented (with a thresholding technique), i.e., transformed from grey scale to black and white images, which determines whether each pixel is part of the foam or just the background. Moreover, some morphological operations could be applied to the 2D slices which could improve their quality. All these techniques are analysed and described in this chapter. The software *CTAn*[1] version 1.17.7 by Bruker was mainly used for this purpose. It provides useful tools for the analysis of foams and their structure.

3.1 X-Ray Microcomputed tomography

X-ray Microcomputed Tomography (μCT) is a technique to non-destructively characterize the microstructure of a material or material specimen in three dimensions at a micron level spatial resolution using an X-ray beam [15]. It is characterized as a radiographic

[1] CTAn, Bruker, www.bruker.com/products/microtomography/micro-ct-software/3dsuite.html

imaging technique, requires no specimen preparation and many scans can be performed for the same specimen under different conditions. Even though it has been primarily used for the characterization of foam specimens in the field of metal foams [25, 41–44], i.e., analysing the properties of the micro- and macro-structure, its application for obtaining 3D models has been developing over the last few years [7–13]. The latter is the focus here. By analysing the literature, it can be seen that the involved parameters are very highly dependent on the characteristics of the foam, for example, base material, pore size, porosity type, the knowledge of the user and the conditions. Lack of knowledge of the user can result in poor scan quality and/or inability to extract adequate information for the required research purpose. Consequently, it is difficult to extrapolate a conclusion about how to properly proceed with the scans.

In μCT the X-ray emissions pass through a turntable sample and are projected on a digital detector (e.g., flat panel). The projection images are taken incrementally over a total rotation of either 180° or 360°. The acquired radiographs are mathematically reconstructed into slices allowing the reconstruction of a tridimensional (3D) map, in which each voxel (volume element or 3D pixel) represents the X-ray absorption at that point. The 3D map is usually presented as a series of 2D slices (Fig. 3.1) [15]. This technique is based on the partial absorption concept. The quality of the images depends mainly on the partial absorption and differential absorption that occurs during the scanning step. The partial absorption is associated with the absorption of some X-rays by the specimen and the transmission of others to the detector. The differential absorption refers to the absorption characteristics of the different materials to be scanned. For example, in the case of there being no differential absorption, the specimen's result comes out as an uniform grey level (no contrast). Usually, it is difficult to distinguish the different materials within the specimen. Both (partial and differential) absorptions are influenced by several aspects, such as the size of the specimen and the chemical composition of the material which the X-rays have to pass through. Each level of absorption/attenuation is saved on each image as a value of grey, from black to white. Therefore, a grey scale usually of 8 or 16 bit, i.e., 256 or 65 536 different levels of grey, is used to store and analyse the results from the scans (Fig. 3.2). This technique is useful not only for human visual perception but also for image processing.

3.1.1 Foam Specimens

There are many variables involved in such a technique and each could significantly change the end result. For this reason, it is difficult to obtain consistent results even for the same specimen when considering different users or different commercial μCT scanners. There are different μCT scanners on the market, each having different characteristics, namely the resolution, maximum energy level, different filter options, stage set up and internal chamber area. Some of the considered parameters are, for example, X-ray source voltage, image pixel size, rotation step, filter type (e.g., no filter, copper and aluminium), exposure time, among many others [45]. It should also be noted that the analysis starts from the 2D reconstructed slices and not from the 2D projection images. As a result, the influence of that transformation and what is involved in it aren't evaluated.

Due to the pandemic situation in the period of this work, the 2D slices of the different foam specimens used to perform this research work were analysed previously by other

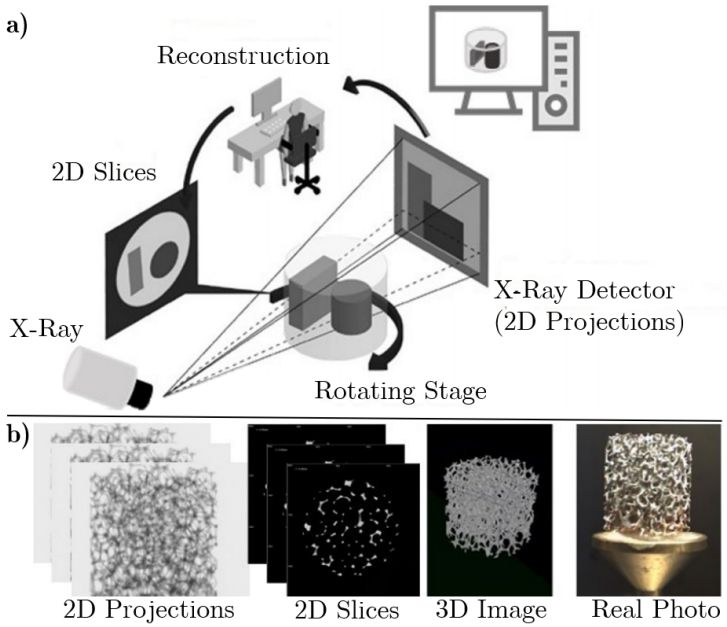

Figure 3.1: Schematic of the X-ray microcomputed tomography (µCT) equipment and an open-cell aluminium foam (height: 20.4 mm; diameter: 18.9 mm) (a) and showing and showing raw scans/projections, segmented images, reconstructed structure, and real photo [25].

researchers in the TEMA[2] lab using a SkyScan 1275 scanner (Bruker μCT, Belgium). The closed-cell specimen was analysed with penetrative X-rays of 80 kV and 125 μA, a 1 mm aluminium filter in high resolution mode with a pixel size of 15.001 µm and 48 ms of exposure time. It was prepared by a powder metallurgy method with AlSi7Mg as the base material, which has a density of 2.670 g/cm^3 and Young´s modulus of 74 GPa [24]. The different physical properties of the foam itself, such as, mass and volume, are also provided for later use in the quality indicator during the thresholding (binarization) (Table 3.1). However, the only available values were for the foam after having been produced but, unfortunately, it was cut to facilitate further analyses. Consequently, some approximations were performed. The original mass was 3.200 g and the volume of the Bounding Box (V_{BB}), i.e., the smallest box that can be wrapped around an object, was 8000 mm^3. The scanned foam has a size of 14.000×14.500×15.571 mm which corresponds to 3160.913 mm^3. Comparing to the original volume of 8000.000 mm^3, the specimen is just 39.5% volume-wise. Assuming the material is homogeneous, which is incorrect but close enough for an approximation, the same proportion is applied to the mass of the whole structure, 3.200 g. As a result, the value of mass to be used is $0.395 \times 3.2 = 1.264$ g. Considering the density of the material mentioned above, the volume of the object is calculated to be 473.545 mm^3, which is used later during analysis. The volume of the bounding box of the foam, V_{BB}, should not be confused with the volume of the object, or foam, inside the bounding box, V_{f}.

During the analysis, a large crack along the foam was identified which seemed ar-

[2]Department of Mechanical Engineering, Centre for Mechanical Technology and Automation (TEMA), Universidade de Aveiro.

tificial. As seen in Figure 3.2, there is a clear misalignment between the sides of the shown crack, which provides further evidence. Nevertheless, its origin is unknown but is suspected to be the process of cutting. The presence of such a defect could influence the results, however, it is not clear and the unavailability of another specimen restricts the options.

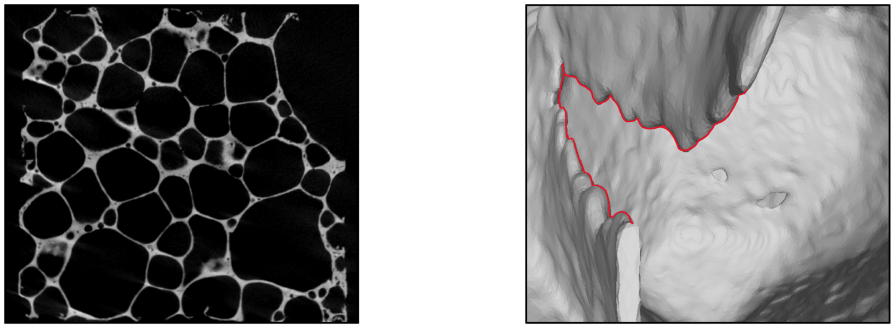

Figure 3.2: One 2D slice of the closed-cell foam (left) and distorted foam which is evidence of damage to the foam (right).

The second set of 2D slices belongs to a cubic open-cell foam made of AlSi7Mg with pore sizes of 10 ppi (pores per inch) supplied by Mayser GmbH & Co. KG (Germany)[3]. The cubic open-cell specimen (22×22×25 mm) was analyzed with penetrative X-rays of 40 kV and 250 μA, a 1 mm aluminium filter in high resolution mode with a pixel size of 15.001 μm and 132 ms of exposure time (Fig. 3.3). The mass and foam volume are 1.100 g and 411.990 mm^3, respectively (Table 3.1).

The third set of 2D slices belongs to a cylindrical open-cell foams made of AlSi7Mg with pore sizes of 10 ppi (pores per inch) also supplied by Mayser GmbH & Co. KG (Germany). The specimen (diameter: 19 mm; height: 20 mm) was analyzed with penetrative X-rays of 50 kV and 200 μA, a 1 mm aluminium filter in high resolution mode with a pixel size of 14.001 μm and 75 ms of exposure time (Fig. 3.3). The mass and volume of this foam specimen are 0.910 g and 340.820 mm^3, respectively (Table 3.1).

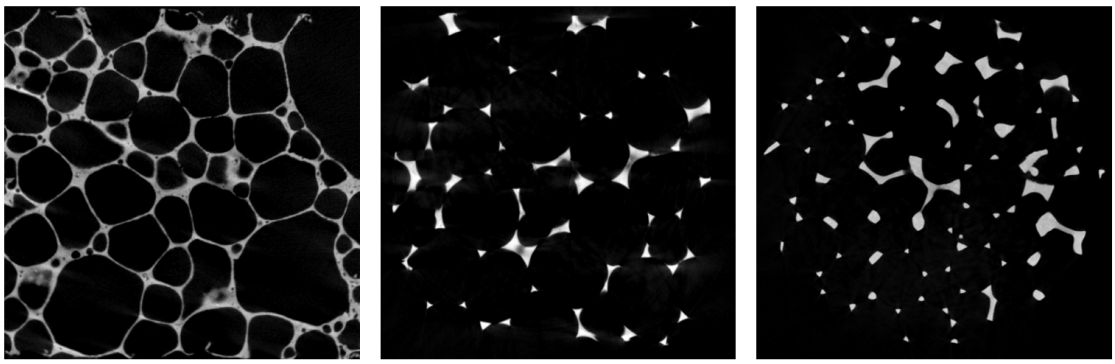

(a) (b) (c)

Figure 3.3: 2D slices of the closed-cell foam (a) cubic open-cell foam (b) and cylindrical open-cell foam (c) specimens.

[3]Mayser GmbH & Co. KG (Germany), www.mayser.com/en

Table 3.1: Properties of the closed-cell (CC), cubic open-cell (Cubic OC) and cylindrical open-cell (Cylindrical OC) foam specimens made of aluminium alloys.

	CC	Cubic OC	Cylindrical OC
Production Method	Powder Met.	Investment C.	Investment C.
Material	AlSi7Mg	AlSi7Mg	AlSi7Mg
Material Density, ρ_s (g/cm^3)	2.670	2.670	2.670
Young's Modulus, E_s (GPa)	74	74	74
Mass, m_f (g)	1.264	1.100	0.910
Foam Volume, V_f (mm^3)	473.545	411.990	340.820
Bound. Box Volume, V_{BB} (mm^3)	3 160.913	12 100.000	5 726.070
Image Pixel Size, s_p (μm)	15.001	15.001	14.001

3.2 Images as Discrete Functions

After having acquired the 2D slices with the μCT scanner, it is necessary to process them so that they can be used to reconstruct a 3D geometry. Therefore, for the clear understanding of this chapter, it is fundamental to first portray how digital images work and how they can be described as discrete functions.

An image $\mathbf{I}$ can be defined in the form of a 2D ordered matrix of integers (Fig. 3.4), i.e., it is a 2D function that maps from the domain of integer coordinates $\mathbb{N} \times \mathbb{N}$ that form a bitmap image to a range of possible pixel values $\mathbb{P}$ such that [46]

$$\mathbf{I}(u, v) \in \mathbb{P} \text{ and } u, v \in \mathbb{N}. \tag{3.1}$$

In the case of these μCT scans, the value of each pixel is indicated on an 8-bit grey scale, i.e., from 0-255 or 256 different values of grey ($2^8 = 256$). The size of the image is calculated directly from the number of columns and the number of rows of the image matrix $\mathbf{I}$. Additionally, the image pixel size or resolution specifies its spatial dimensions in the real world and is relevant when discussing about μCT scans given that it influences how much detail is captured (Sec. 3.1.1). Values around 15 μm were used as mentioned in Table 3.1.

A very important concept in digital image analysis is the histogram. The histogram is used to depict image statistics in an easily interpreted visual format. They represent, in general, frequency distributions, i.e., they describe how often a certain intensity or value of the grey scale occurs in an image, which is in this case a direct consequence of the attenuation of X-Rays during scanning with the μCT scanner [46]. The histogram for a grey scale image $\mathbf{I}$ with intensity values in the range $\mathbf{I}(u, v) \in [0, L-1]$ has exactly L entries, where L for an 8-bit image is 256. Furthermore, it is a very useful tool for defining a threshold value between the foreground and the background, i.e., the analysed object or foam and the unwanted additional information, since it provides a distribution of the values of grey observed in the analysed images.

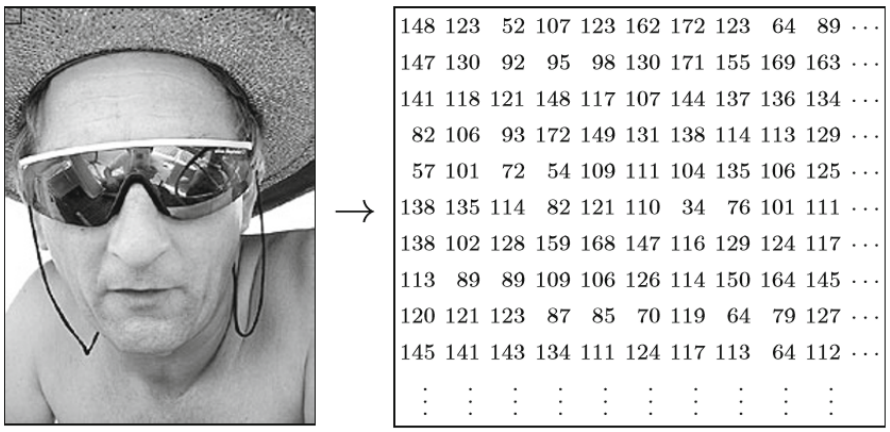

Figure 3.4: Discrete digital image $\mathbf{I}(u, v)$ on an 8-bit scale [46].

3.2.1 Region/Volume of Interest

The images provided by the scan included exterior areas that have no interest for the analysis and can have some speckles, hence, they must be eliminated. The software *CTAn* provides very useful tools for this purpose. The user selects a Region Of Interest (ROI) in the 2D slices so that it contains the useful information regarding the specimen and discards what is not important (Fig. 3.5). The ROI is then extended on a third axis, usually $\hat{z}$, providing a 3D region which envelopes the whole foam and is called the Volume Of Interest (VOI). On one hand, when the main objective is the morphological analysis in 2D or 3D (e.g., mean cell size and cell size distribution, fraction of solid, connectivity between cells, cell orientation, and porosity), it is important to select a ROI/VOI that tightly fits the foam so that it can be better observed and easily analysed by the software. On the other hand, when the goal is to obtain a 3D model, the regions can be more relaxed. After it is setup, the specimen is ready for the next steps.

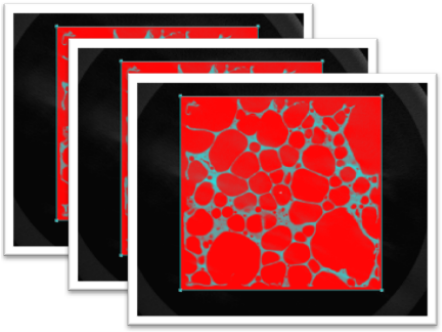

Figure 3.5: Example of region of interest of closed-cell foam. Corners contain some speckles that are negligible, therefore, not included.

3.2.2 Thresholding Techniques

Thresholding or image binarization/segmentation is an essential step in which the different phases/constituents are distinguished using thresholding algorithms which measure

the grey scale values in the 2D μCT reconstructed images [47]. In other terms, these processes transform images from levels of grey to binary (black and white). The resulting binary images, in this case 2D slices, are then comprised of two types of pixels: black, which represent the background; white, which represent the object. Therefore, the main goal is to find a certain value k (threshold) on the grey scale (0-255) which best separates the two main phases. The adjustment of the threshold allows the enhancement of the intensity and/or contrast in order to improve the visualization of the regions of interest of the specimen by decreasing the noise or unwanted background signal.

These techniques are based on point operations given that a modification to each pixel value is performed, in which there is no change to the size, geometry or local structure of the image. In addition, the new values depend exclusively on the previous values and are independent from any other pixel [46]. The general function, f, for such type of operations is given by

$$b = f(\mathbf{I}(u,v)) \quad \text{or} \quad b = f(a), \tag{3.2}$$

where a are the original values which are mapped to the new values b. For a thresholding technique with a defined threshold, the relationship can be expressed as follows (Fig. 3.6):

$$g(\mathbf{I}(u,v)) = \begin{cases} 255 & \longleftarrow \quad f(I(u,v)) > k \\ 0 & \longleftarrow \quad f(I(u,v)) \leqslant k \end{cases}, \tag{3.3}$$

where k is the threshold value, in this case somewhere on the 8-bit scale (0-255). Therefore, every pixel that has value superior to the threshold is assigned a 255, which is the same as white, and all others are assigned with a 0, or black. In the end, the final image will only include black and white pixels and the shape of the foam has been determined.

The key question is how to find a suitable or "optimal" value k that best applies in each case and preserves the best information. Should it be at 50% (128)? As it can be seen in Figure 3.6, it appears to work better than others, but it still isn't ideal since it eliminates some information in the corners. To overcome this problem, several thresholding techniques are discussed: the global thresholding technique of Otsu [48], which takes a statistical point of view; some adaptive techniques [16], which are local and perform calculations using smaller sections; and a manual global technique with a quality indicator [10]. Before the application of the thresholding techniques, different smoothing convolution filters and histogram operations could be applied to the 2D slices, however, these create unwanted distortions on the final geometry, therefore, they are not considered [46].

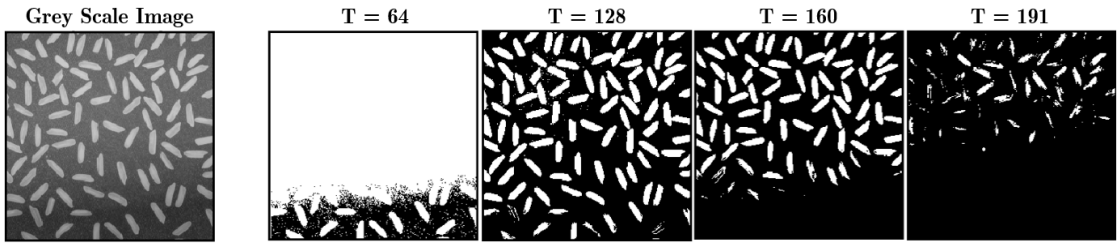

Figure 3.6: Example of different threshold values for the binarization of a grey scale image of rice obtained through MATLAB (www.mathworks.com).

3.2.2.1 Otsu Thresholding Technique

Generally, thresholding techniques can be categorised into two classes: global thresholding and local thresholding. For global thresholding, a single threshold value is used to separate the foreground and the background image. The Otsu thresholding has shown great reliability, simplicity and adaptability along the years and it is still the most used in image processing [47]. It determines an optimal threshold of an image by minimizing the within class variance, i.e. the background and foreground/object classes, using only the grey scale histogram of the image [48]. In addition, it is used, in its primary form, to separate images with bimodal characteristics, i.e., images with two main peaks in the histogram and it works unsupervised, since no human interaction is needed to define any parameter [16]. Other types of thresholding techniques also exist, for example, multi-level thresholding [49], but aren't considered for the purpose of this dissertation. Further information about the Otsu thresholding technique can be found in Section A.2.

The Otsu thresholding technique was then applied to the foam specimens considering not just the information of one 2D slice/image, but all the 2D slices of each specimen. Therefore, it was applied in 3D. This way, the calculations are done with the histogram of the sum of all the pixels of the series of reconstructed images (2D slices), yielding results independent of each individual slice. Results show that for reconstructed images with clear borders there is good separation between the background and foreground which provides a clear visualization and understanding of the regions of interest of the specimen (Fig. 3.7). However, for regions with more noise or less differentiation between classes, there are many slight imperfections and a many small defects, creating a demand for more intense post-processing. Another disadvantage of this process is that it simply relies on information regarding the 2D slices. No external information is introduced. For these reasons, this technique might not be ideal.

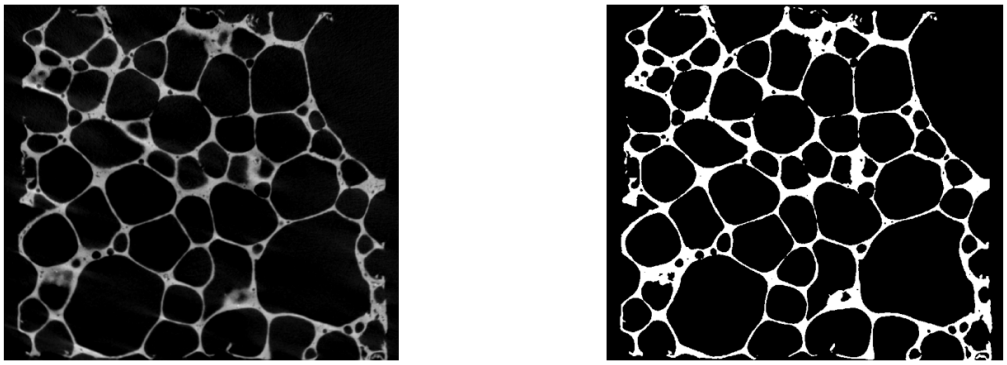

Figure 3.7: Application of the Otsu thresholding technique in 3D for the closed-cell foam specimen, which yields a threshold k of 70.

3.2.2.2 Adaptive Thresholding Techniques

Contrasting to the global thresholding mentioned above, local or adaptive thresholding techniques are discussed. Here, the threshold k is derived for each individual pixel by taking the values of the surrounding pixels in a specified region, i.e., the original image is divided into smaller areas. This definition could at first sight seem better for the

final result since it takes local differences in the reconstructed images into consideration. However, it usually requires human intervention to define certain parameters and takes longer to calculate the results. Adaptive thresholding (AT) techniques are commonly used to investigate a wide range of aspects related to the biology of bones and other calcified tissues and for scenarios with presence of lightning gradients [16, 47].

Mean-C, Median-C and Mean of Minimum and Maximum Values are some examples of AT techniques. All of them work with the same principle, despite presenting small differences. In essence, these techniques go through all pixels, and perform calculations with respect to the pixels inside a defined area, if considering a 2D image, or volume if considering a stack of images. This area/volume can be imagined as a matrix and can be selected to have a rather flexible shape, however, for more consistency, square/cuboid or circular/spherical/cylindrical shapes are usually used. In the case of the Mean-C, the mean of the values inside the defined area/volume around each pixel is calculated and a constant, C, a user specified value, is subtracted to it, obtaining the threshold. Then, the pixel in study is selected to be part of the background or part of the foreground through Equation 3.2. The Median-C and the mean of the min and max values techniques are similar to the one described, however, instead of calculating the mean of all values, they calculate the median and the mean of the minimum and maximum values within the defined area/volume, respectively. All the AT techniques require human intervention, unlike the Otsu thresholding technique, to select not only the size and shape of the selected area/volume, but also the value of the C constant. For these reasons, there are many fluctuations in the results.

The application of AT versus Otsu has been very well documented for open-cell foams, where the foam morphology is analysed with respect to the applied technique [16]. The technique which considers the mean of the minimum and maximum values was mainly investigated and it was verified that some artificial pores appear in the struts of the foams and that the technique and its parameters impact the strut diameters greatly. The same outcome was verified here for the open-cell foams as well as for the closed-cell foam for all techniques and not just the minimum and maximum technique (Fig. 3.8). The results demonstrate that the presence of such voids in the walls and struts eliminates mass and changes the structure of the foam, which is detrimental, specially, for structural analysis.

Moreover, defining the correct parameters is also very difficult because there are many possible combinations. Consequently, this type of technique is discarded as a viable option.

3.2.2.3 Global Manual Thresholding Technique

Another alternative is to apply a manually selected global threshold to the foam slices. This technique, unlike the others, allows the user to consider and introduce external properties in the calculation process of the ideal threshold value. Therefore, it isn't solely limited by the properties of the 2D slices which are being analysed.

The manual selection of the threshold provides a great opportunity to have more control over the process through the implementation of a quality indicator. However, it is difficult to gather and select information that could be used to verify the correctness of the results. In the case of foams, there is little information regarding the topology, architecture of the real structure, and the shape, except the information that is gathered from the scans. However, the images provided by the scans are also influenced by

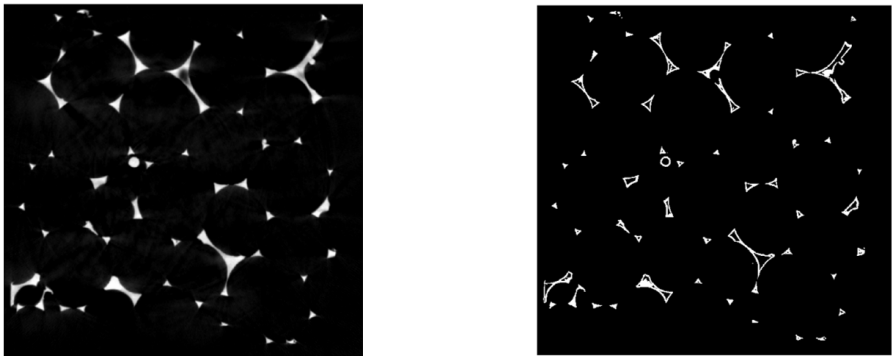

Figure 3.8: Application of the Mean-C technique on the 2D slices of an open-cell foam (Radius of 2 and constant of 15). Original on the left and binary after AT thresholding on the right.

the scans themselves. Therefore, choosing a physical property of the real foams as a reference might be ideal. It can be contrasted with the outcome of the 2D slices and used to evaluate the results. In this scenario, it is a good choice to take the image pixel size/resolution of the μCT scans and the number of white pixels, i.e., the object or foreground, for each specific value of threshold, calculate the volume of the structure and convert it to mass with the value of density of the base material. The calculated mass can then be compared to the real one. The threshold that yields the lowest difference between the real and virtual masses is, therefore, the ideal choice and the one that should minimize differences in the geometry. Consequently, there is at least some certainty that the virtual foam has the same amount of matter as the real one, therefore, having more chances of behaving like one during mechanical analysis. Thus, the mass of the foam is considered as the new quality indicator.

The volume of the specimen was calculated directly by *CTAn*[4] which provides a 3D quantitative analysis tool. The mass of the foam can then be calculated as

$$m_{\mathrm{f}} = \rho V_{\mathrm{f}} \tag{3.4}$$

where m_{f} is the mass of the foam, ρ is the density of the base material and V_{f} the foam volume. The volume is going to be interchangeably used with the mass since they represent the same thing, assuming a constant material density.

The next step is to find the value of the threshold that minimizes the difference between the real mass and the "mass" of the virtual foam (calculated with *CTAn* and Equation 3.4). This operation could be troublesome since there are 256 different levels (8 bit) that could result in the lowest difference and each would have to be tested, which is unreasonable. For this reason, a sensitivity analysis is recommended. The goal is to find if there is a relation between the two variables of interest, the threshold, k, and the volume (or mass) measured in the software, V_{f}. Using the volume doesn't require several conversions, therefore, it is preferred.

For this purpose, *CTAn* was used and the following functions were applied in the custom processing menu to obtain the required values:

- **Threshold**: Binarizes images with the selected technique;

[4]CTAn, Bruker, www.bruker.com/products/microtomography/micro-ct-software/3dsuite.html.

- **3D analysis**: Calculates an array of properties that describe the structure in question, e.g., volume, surface area, among others;
- **Save Bitmaps**: Saves the sets of images obtained up to that point;
- **Reload**: Reloads the base images in grey scale in order for the process to be repeated.

The thresholding process was repeated throughout the 8-bit scale in a spaced-out way in order to get a sense of how both properties interact.

3.2.2.4 Results

In the case of the cubic open-cell foam, values of the threshold, k, from 30 to 120 were applied resulting in volumes, V_f, from 610.104 to 363.718 mm^3, respectively. The values of the surface area are also provided, however, there isn't any information relating to this parameter for a comparison to take place. Results show that for increasing threshold values both the foam volume and the foam surface area decrease. Figure 3.9 further clarifies this fact and shows an almost linear relationship between both parameters. However, for low levels of k, small noise/speckles are picked up, therefore, creating a slightly curved line which is easily fitted with a higher polynomial or logarithmic tendency curve (in *MS Excel*). In this case, the latter was used and its equation, with a value of R^2 of 0.992, is

$$V_\mathrm{f} = -170.8 \ln(k) + 1180.3. \tag{3.5}$$

As seen in Table 3.1, the expected volume for this foam (V_f), which weighs 1.100 g, is 411.991 mm^3. Solving the equation above for k, a threshold of 90 was obtained which provides a volume of 413.202 mm^3. Given the obtained value is an approximation, the value above, $k = 91$, was tested, yielding a volume of 411.410 mm^3, which corresponds to a very small difference of 0.141% of the real volume. Therefore, results indicate that for this foam the process was very successful in maintaining at least the same amount of material as the real foam, which is important when considering the objective is a finite element analysis.

The same procedure was repeated for the cylindrical open-cell foam. This foam was produced in the same way as the one studied above, therefore, it provides a good comparison and brings greater robustness to the process. The mass of this specimen is 0.910 g and the object volume is 340.820 mm^3 (Table 3.1). The corresponding curve (Fig. 3.10) is defined as

$$V_\mathrm{f} = -73.15 \ln(k) + 597.83. \tag{3.6}$$

The final value obtained for the threshold, k, was ≈ 34 which was adjusted manually to 32, consequently leading to a volume of 341.291 mm^3, which corresponds to a difference of 0.138% of the real foam volume. Comparing both specimens, there is a clear distinction in the value of the thresholds. Even though their structure is similar, these values don't resemble each other, so, regardless of the number of specimens, it is safe to assume based on the results and visual breakdown of the slices of each foam that the value of the threshold depends greatly on the μCT scan parameters. Due to the great number of variables and lack of sets of slices, the dependence was not tested. The same set of scanning parameters could also be tested to test the differences in the final threshold.

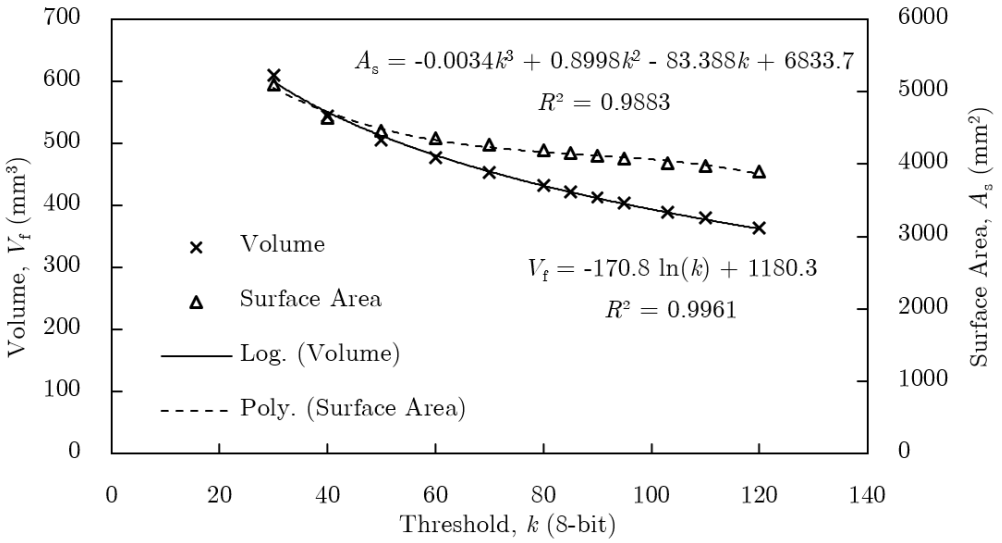

Figure 3.9: Threshold sensitivity analysis for the cubic open-cell foam specimen.

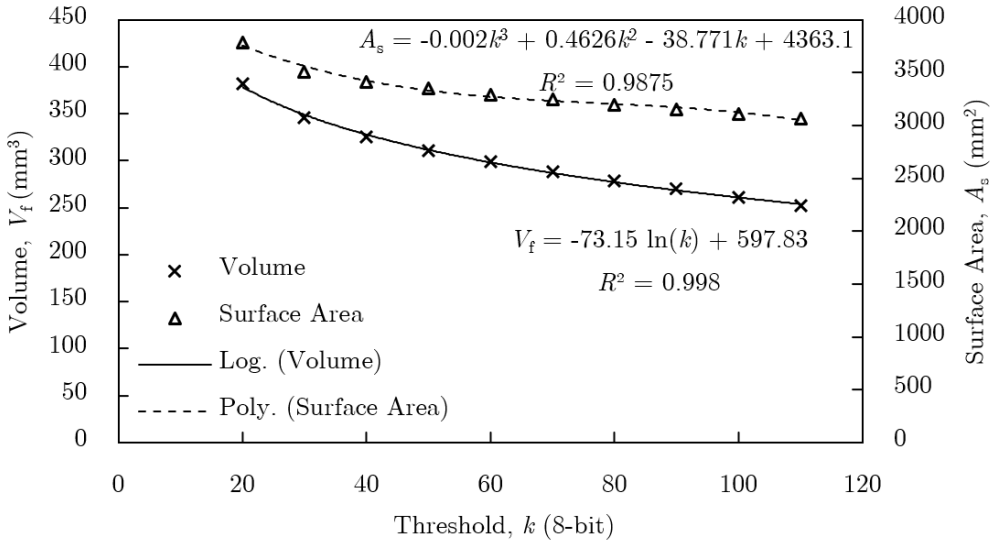

Figure 3.10: Threshold sensitivity analysis for the cylindrical open-cell foam specimen.

After that, the same analysis was performed to the closed-cell foam. Different thresholds are applied which correspond to different volumes and different surface areas. However, as mentioned in Section 3.1.1, the specimen that was examined with μCT had been previously cut, therefore, yielding a different mass for the smaller section than for the whole foam. For this reason, the mass was approximated by a proportion with the volume of the bounding box (V_{BB}), i.e., volume of the smallest box that can be wrapped around an object, with measurements known from the complete foam and manual measurements taken inside *CTAn*. The volume of the bounding box of the foam, V_{BB}, should not be confused with the volume of the foam inside the bounding box, V_{f} which is being recurrently used as a quality indicator together with the mass. The value of mass to be used is 1.264 g and a volume of 473.545 mm^3 (Table 3.1). In this case, the volume equation is given by

$$V_{\mathrm{f}} = -210.5 \ln(k) + 1282 \tag{3.7}$$

with a corresponding R^2 of 0.9911 (Fig. 3.11). An almost linear relation is again verified in the middle range of the scale, however, the effect of the speckles and noise is again present for lower levels. The surface area shows a less predictable behaviour, which can also be analysed in Figure 3.11. Finally, an ideal threshold is found to be 47, which yields a volume of 474.056 mm^3, i.e., a variation of 0.108%. In contrast, Otsu thresholding yields a variation in the final volume/mass of 15.048% (with a threshold of 70). Hence, the manual selection of the threshold based on the quality indicator is preferred.

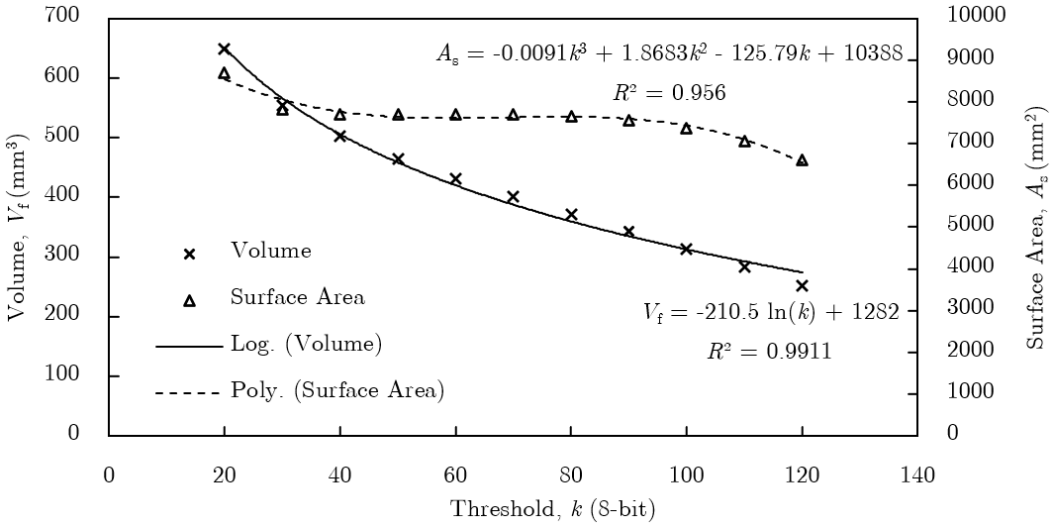

Figure 3.11: Threshold sensitivity analysis for the closed-cell foam specimen.

3.2.3 Morphological Operations

The presence of small defects and very small pores can sometimes be unwanted and problematic for the next stages of acquiring a geometry of a foam. Morphological operations, more specifically, the closing operation, are a very good tool to avoid these sorts of problems and make the surfaces more regular, maintaining, for the most part, the shape and architecture of the structures. It also brings some loss of information to the process

and the values of threshold for the same volume can be different because of the closure of pores, which increases the amount of mass in play. The objective of this section is to understand how such operations change the specimens and how they influence the output parameters with respect to the quality indicator evaluated above.

Here, the morphological operations are aimed at binary images, i.e., images with only two possible values, 0 and 1, or black and white, respectively. The basic idea is to apply a filter to the image, which in this case is denoted as structuring element, and alter the value of each pixel accordingly. The structuring element is then a matrix, itself in binary, that runs through all pixels and modifies them according to their neighbourhood. The neighbourhood, i.e., all the pixels inside the structuring element, can be defined by the user, where the locations with a value of 1 are considered and locations with a value of 0 are ignored and do not count. In simpler cases, e.g., rectangular pixel grids, the neighbourhood can be defined as (Fig. 3.12):

- **4-neighbourhood (N4)**: the four adjacent pixels in the vertical and horizontal directions;
- **8-neighbourhood (N8)**: The pixels contained in N4 plus the diagonal directions.

However, the structuring element can be used in various forms and can have many different sizes.

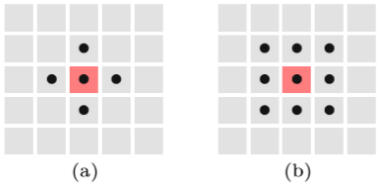

Figure 3.12: Structuring elements. Dots are 1's, empty spaces are 0's, red spot is the pixel in study. (a) N4; (b) N8 [46].

The two basic operations applied with this sort of element are: dilation and erosion. The dilation operation can be described as a growing of the foreground, i.e., of the object itself. During the sweep of the image with the filter, if a target white pixel (1) has a neighbouring pixel, i.e., which is inside the structuring element, defined as a 0, then this pixel is turned into a 1, progressively growing the structure. This effect can be seen in Figure 3.13 where a 3 by 3 N4 structuring element is applied. The opposite case is the erosion operation. Instead of growing the structure, it shrinks it. In Figure 3.13, when the 3 by 3 N4 filter is applied to each pixel, each one which has a pixel of value 0 in it's neighbourhood is converted to a 0 [46].

3.2.3.1 Closing Operation

Although both operations appear simple and limited in their applications, their combination can have extreme benefits in some cases. One example of these combinations, which is quite useful for the 2D slices of the foams, is the utilization of a dilation followed by an erosion, also known as a closing operation. It is useful because it can remove/close holes and fissures in the foreground structures that are smaller than the structuring element. The inverse operation, i.e., an erosion followed by a dilation which is also known

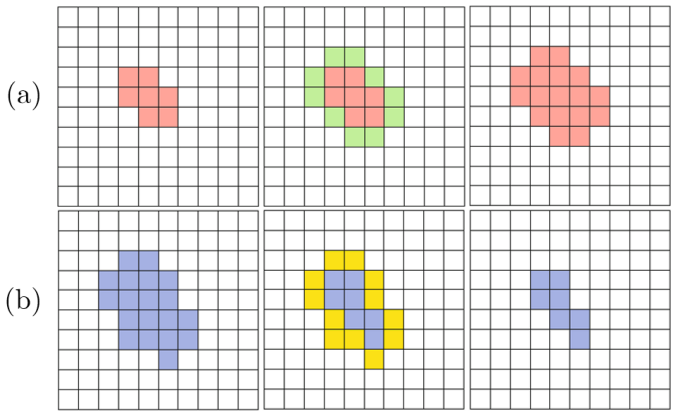

Figure 3.13: Example of dilation (a) and erosion (b) [46].

as opening operation, isn't considered since results show the effects aren't desirable, for example, the opening of smaller pores and defects.

When a closing operation is applied to the open-cell foams, the effects are not obvious and only a smoothing of the surface is observed. In contrast, when applied to the closed-cell foams, the impact is very meaningful and it changes the topology of the structure. The following effects can be seen:

(i) Pores smaller than the structuring elements are closed;

(ii) Surfaces are smoothed;

(iii) Some holes in the walls of the pores are closed.

The effects are, for the most part, desirable, however, the changes in topology, addition of material and changes to its distribution can be significant and finally alter the behaviour of the geometry when placed under loads during a finite element analysis. Nevertheless, it makes it easier to process the geometry in subsequent steps and reduces the number of kinks and areas of singularities. As a result of this ambiguity, it is crucial to understand how this phenomenon changes the structure and how the mass of the object changes.

For this reason, a sensitivity analysis was performed for different structuring elements. Caution is required when using such operations due to the fact that specimens with smaller image pixel sizes, i.e., with a higher number of pixels per a given area, are going to have different results when comparing with specimens with larger image pixel sizes. This issue originates from the definition of the structuring element which is, in simpler terms, a matrix/filter that runs through all the pixels. As a consequence, the values that characterize the structuring element are presented as real distances instead of matrix sizes:

$$R_{\mathrm{r}} = s_{\mathrm{p}} \cdot r_{\mathrm{SE}}, \tag{3.8}$$

where R_{r} is the radius of the structuring element in the real world, r_{SE} is the radius in terms of matrix sizes and s_{p} is the image pixel size, which is 15.001 μm for this foam (Table 3.1).

The structuring elements used in Figure 3.14 were all in 3D and approximately spherical. Filters in a shape of a cube (3D array filter) could have also been used,

however, they caused some pores to start assimilating a cuboid shape whereas the original pores have roughly the shape of a sphere. Radii values of 2, 4, 6 and 8, which correspond to real radii of 0.03, 0.06, 0.09 and 0.12 mm, respectively, were tested. These values mean that for each iteration small pores of radii inferior to the one used were eliminated and the walls were smoothed. Results indicate that as the radius of the morphological operation increases, the final volume also increases. This effect can be easily verified by the stacking of curves starting from the smaller radius, i.e., with no closing operation, to the higher radius in Figure 3.14. For each different curve a new ideal threshold and its corresponding values were calculated (Table 3.2), showing that the differences are very small and probably negligible when it comes to the structural analysis. Larger structuring elements could have been used, however, the computational time increases exponentially and the shape of the final foam would change even further.

The closing morphological operation should produce very satisfactory results like in Figure 3.15, where smoothing of the walls and closure of small pores can be observed.

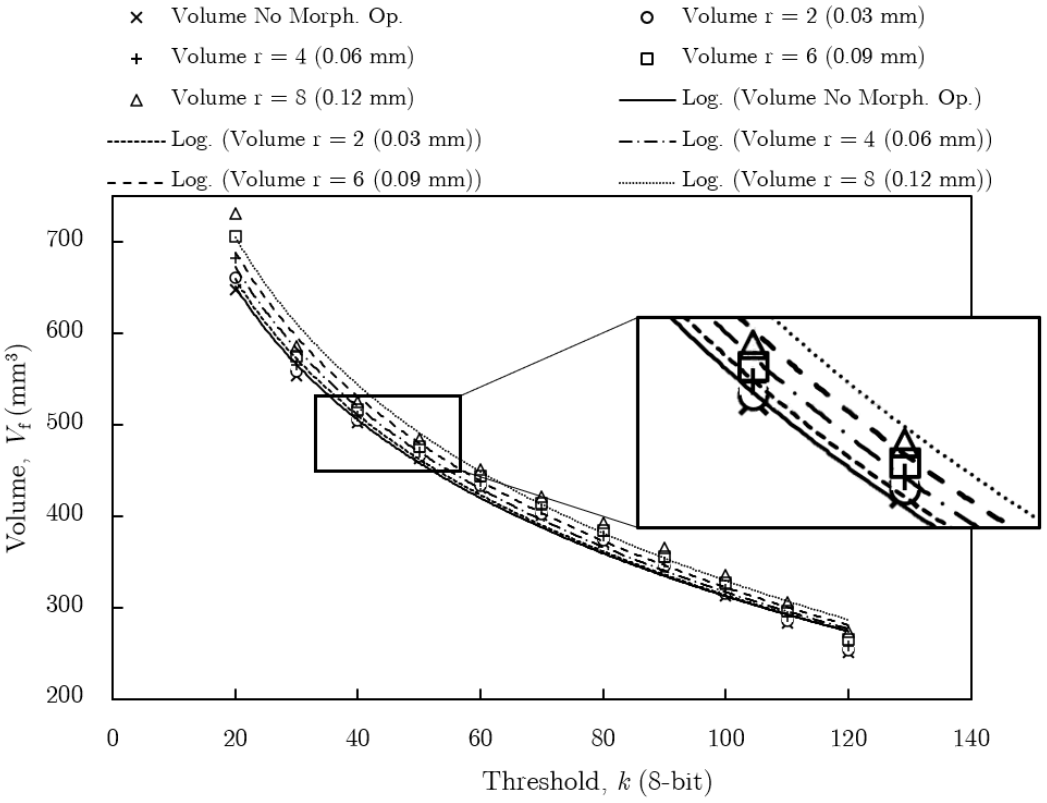

Figure 3.14: Sensitivity Analysis for different radii of the structuring element.

3.2.4 Despeckle

After completing the previously detailed process, the foam is ready for next steps, however, it can be taken even further by the despeckle function provided by *CTAn*. The first application of interest is to remove small objects/speckles up to a given size in 2D or 3D that could originate from the noise of the μCT scans. The second and maybe

most essential is that it can remove small pores, specially inside the closed-cell foams, which can be problematic because of their reduced size. However, connected pores are not eliminated. Several tests verified that the variation in mass caused by this operation were always lower than 0.1% for the tested specimens.

Therefore, the combination of the closing operation with the despeckle provides a very useful tool, where small pores that are connected or disconnected can be removed and the faces can be smoothed. In the end, the result should be very close to what is expected from a real physical foam with small corrections and adjustments which makes it more suitable for the next stages of the process.

Table 3.2: Ideal thresholds for the closed-cell foam specimen with different morphological operations. The error (%) in volume with regard to the real foam is also given.

	Threshold k	Volume (mm^3)	Surface Area (mm^2)
No Morph. Op.	47	474.056 (0.108%)	7693.935
R2 ($R = 0.030$ mm)	48	473.058 (0.103%)	7613.643
R4 ($R = 0.060$ mm)	49	474.143 (0.126%)	7552.480
R6 ($R = 0.090$ mm)	51	473.177 (0.078%)	7462.289
R8 ($R = 0.120$ mm)	53	474.342 (0.168%)	7381.550

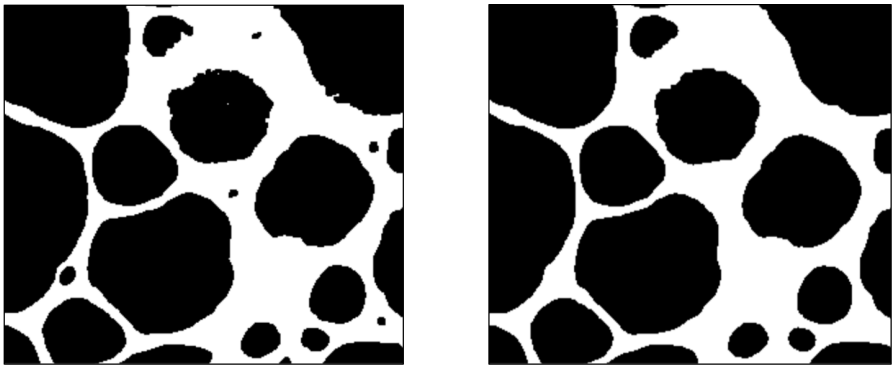

Figure 3.15: Ideal threshold with no morphological operation (left) and ideal threshold for a morphological operation of radius 6 (0.09 mm) (right) for the closed-cell foam specimen.

Intentionally blank page.

Chapter 4

3D Geometry Simplification and Analysis

After having obtained the binarized 2D slices, they can now be used to reconstruct a 3D model in STL that accurately represents the real foam. Nevertheless, the obtained 3D model, or surface mesh, or boundary mesh is flawed, i.e., it has too many nodes and several small errors, and must be corrected and simplified so that it can be utilized in Finite Element Method (FEM) analyses. That is the focus of this chapter: to develop a procedure from the 2D slices, i.e., the images which come from the μCT scans and are processed, to the raw 3D model until the final, clean and simplified 3D model. However, some difficulties emerge, namely that the procedure itself can have a major impact on the final results. For that reason, the procedures and involved algorithms were selected for their ability to cause meaningful yet minimal change to the structure of the foams. Similar research has been done in order to acquire the 3D models for FEM simulation, however, the effects of the process were not investigated and no control variables were presented, such as the evolution of the mass or changes in the shape [7–9, 11–14]. Hence, these topics are given a greater focus in this document.

In this chapter, the 3D models are reconstructed using reconstruction algorithms, such as the Marching Cubes 33 [17] and Double-Time Cubes [45], which provide a final 3D boundary mesh of triangles (tessellation). Due to the discrete nature of the 2D slices, several errors occur, for example, non-manifold vertices, self-intersecting faces and missing faces. Given that the purpose of obtaining such geometries with μCT scans is the geometrical correctness, allowing such defects to prevail would be counterproductive and the purpose would be somewhat lost. In addition, the 3D models are very oversampled due to the high resolution of the 2D slices which cause higher computational requirements and make their introduction in FEM more difficult. For these reasons, several algorithms are introduced which try to minimize the amount of lost data and preserve the geometric accuracy while reducing the size and computational requirements of the models.

So that the influence of the simplification procedure on the final results is evaluated, two different procedures are presented. The first seeks to maintain all the small details, defects and cracks that connect pores in an attempt to more accurately replicate the real foam specimens. The second aims to eliminate those features to make the model more stable and smooth by targeting and eliminating faces with high discrete curvatures.

Finally, the resulting 3D models are tested to ensure the simplification was done successfully and with minimal loss of information. They are tested in terms of mass/volume

preservation and shape preservation with the Hausdorff distance and the distance between meshes algorithm. The tests provide reassurance that the final 3D models are, in fact, correct and that the procedure of reconstruction and simplification was well done (Fig. 4.1).

The main software used was *Meshlab* [50], which provides a very wide array of algorithms/functions for handling and evaluating 3D models based on triangle meshes. The procedures were developed based on the work of Sharma et al., however, exploring the process and its effects more in-depth [7].

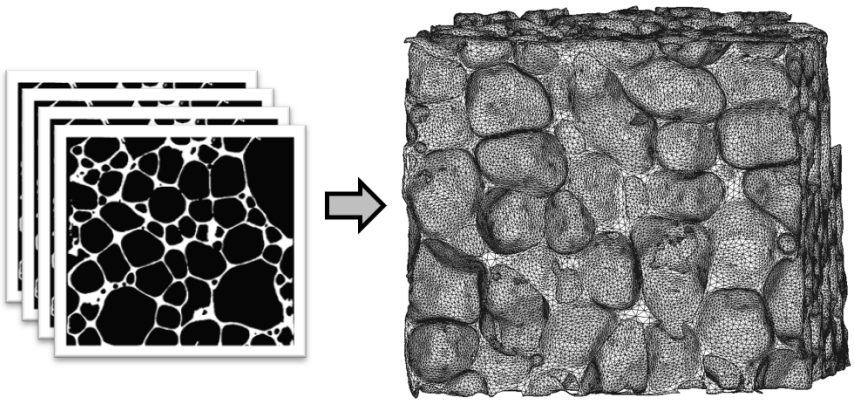

Figure 4.1: Conversion of binary slices to fully processed 3D model.

4.1 STL Format

The STL (Stereoligraphy) file format has been widely used in many fields related to 3D modelling, such as rapid prototyping, 3D printing, medical fields, etc [51, 52]. The files contain a triangular face representation of models and only require information regarding the boundary, or external surface, of a geometry instead of its full body. Other file types based on NURBS[1] and parasolids define curves and surfaces which are used to define the solid geometry [53, 54]. It is, therefore, an approximation of the real structures using triangular faces and is the most common format used in applications regarding 3D scans, e.g., medical CT scans and 3D printing, in which the geometries are built or reconstructed from a point cloud. However, there are several different emerging file types, e.g., the Wavefront format, also known as OBJ, and the Polygon format, or PLY, which are similar to the STL with the inclusion of other properties such as texture. Here, the focus is upon the STL format since there is no need for information relating to the texture. Furthermore, the data on each STL file can described in two data formats, ASCII and binary. The first one is easier for human interpretation, despite its larger file size comparing to the second one. Both types represent the information as floating-points, which can generate some problems with rounding.

The 3D models are represented by a triangular mesh[2] generated by tessellation of the

[1] Non-Uniform Rational B-Spline

[2] Triangular mesh, mesh, boundary mesh, surface or surface mesh are used interchangeably to refer to the geometries represented by triangular faces, here contained in STL files.

boundary of a 3D solid or by reconstruction through a point-cloud, which is described in the following sections. The content of a file of this format is a set of oriented triangles, each described by the following numerical data [52]:

$$\begin{matrix} n_x^{(i)} & n_y^{(i)} & n_z^{(i)} \\ p_{1x}^{(i)} & p_{1y}^{(i)} & p_{1z}^{(i)} \\ p_{2x}^{(i)} & p_{2y}^{(i)} & p_{2z}^{(i)} \\ p_{3x}^{(i)} & p_{3y}^{(i)} & p_{3z}^{(i)} \end{matrix}, \quad i = 1, ..., N \tag{4.1}$$

where $\{n_x^{(i)}, n_y^{(i)}, n_z^{(i)}\}$ are the coordinates of the outward normal, $\{p_1x^{(i)}, p_1y^{(i)}, p_1z^{(i)}\}$, $\{p_{2x}^{(i)}, p_{2y}^{(i)}, p_{2z}^{(i)}\}$, $\{p_{3x}^{(i)}, p_{3y}^{(i)}, p_{3z}^{(i)}\}$ are the coordinates of the first, second and third vertices of the ith face and N the total number of faces. Moreover, the files do not contain any topological information like pointers to other elements and each vertex is written by its coordinates in the file as many times as it occurs in any face of the mesh, which may cause problems with vertex identification. Each face is part of the boundary between the interior and the exterior of the object and its orientation must be specified redundantly in two ways. First, the direction of the normal must be outwards. Second, the vertices are listed in counter clockwise order when looking at each face from the outside (Fig. 4.2). Additionally, each triangle must share two vertices with each of its neighbours, i.e., a vertex can't lie on top an edge, which is usually refer to as the vertex-to-vertex rule (Fig. 4.2) [52].

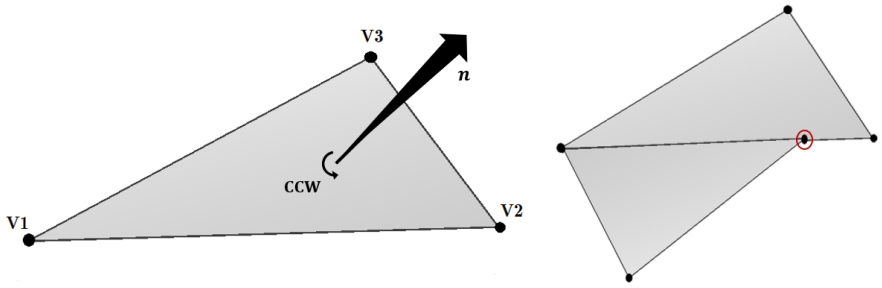

Figure 4.2: Orientation of a face (left) and vertex-to-vertex rule (right).

The STL file format and the surface reconstruction algorithms are not ideal and have inherent problems, therefore, solutions must be found to repair them. Most of the problems that plague STL files are due to the very nature of the format, as it doesn't contain any topological data, and can be classified as follows [55, 56]:

(i) Gaps (Cracks, holes), i.e., missing faces;

(ii) Degenerate faces, i.e., where all its edges are collinear;

(iii) Overlapping faces or self-intersecting faces;

(iv) Non-manifold topology conditions, i.e., non-manifold edge, point and face.

It is crucial to solve these problems as they don't allow for the usage of the geometries in subsequent applications.

4.1.1 Missing Faces or Gaps

Tessellation of surfaces with large curvatures can lead to errors at the intersections between such surfaces, leaving gaps or holes along the model. Depending on their location and positioning, they can be the most difficult problem to solve, however, they can be dealt with and closed with a hole closing algorithm (Sec. 4.3.3).

4.1.2 Degenerate Faces

The formation of degenerate faces occurs when all the faces' edges are collinear despite all the vertices being distinct. This might be caused by stitching algorithms that try to avoid small holes. Given this type of issue doesn't occur often, it is overlooked.

4.1.3 Overlapping Faces or Self-intersecting Faces

Overlapping faces or self-intersecting faces can appear due to numerical round-off errors occurring during tessellation. The vertices are represented in 3D as floating point numbers instead of integers. Consequently, it can cause some faces to overlap. They are quite common and can lead to errors especially during mesh simplifications. Their presence confuses the simplification functions and provides unwanted results. For this reason, they must be dealt with before simplification.

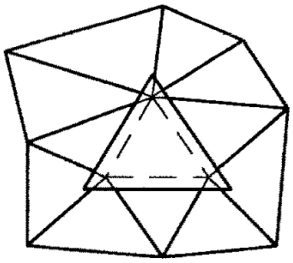

Figure 4.3: Overlapping faces or self-intersecting faces [55].

4.1.4 Non-manifold Conditions

For a surface mesh to be considered valid and to be used in other applications, e.g., 3D printing, FEA, it must be manifold. So, a connected mesh is manifold if every edge is either a boundary edge or a manifold edge, i.e., an edge which is part of exactly two faces. In this case, the final goal is a closed manifold mesh which means that every edge must be manifold and that no boundary edges or intersecting faces may exist. However, some problems may arise during the tessellation of fine features because they are susceptible to round-off errors. There are 3 main types of non-manifold conditions: non-manifold edge; non-manifold point; non-manifold face. A non-manifold edge is shown in Figure 4.4 (a). Here, the edges connect with four different faces instead of two. Figure 4.4 (b) and (c) represent a non-manifold face and a non-manifold point or vertex, i.e., where a vertex is only connected to two faces.

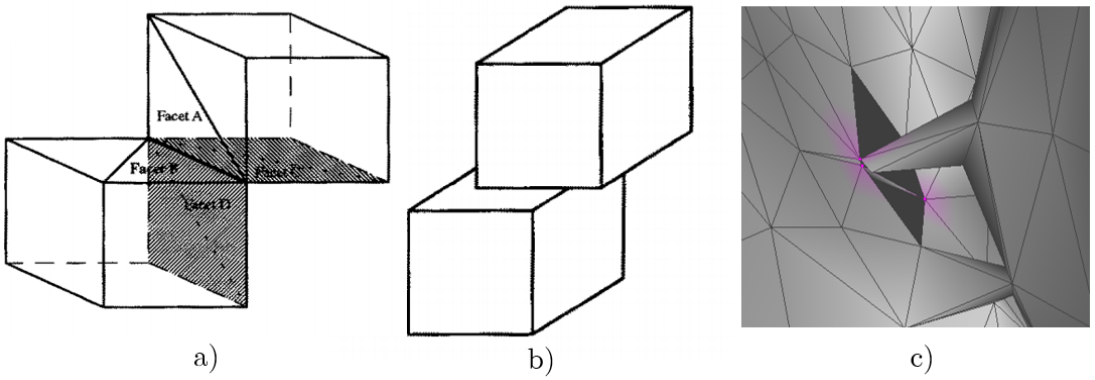

Figure 4.4: Non-manifold conditions. (a) Edge; (b) Face; (c) Point (vertex) [55].

4.2 Reconstruction Algorithms

The representation of the foams with images is discrete, i.e., the images (or 2D slices) are stacked and represented as a matrix of point values that show, in the case of binary images, if a given point is part of the foreground/object or part of the background. Therefore, the foams can be imagined as point clouds, where each point connects to others, forming 3D surfaces. There are many methods that can perform this task, however, only two methods, the ones provided by *CTAn*, are explored more thoroughly: Marching Cubes 33; and Double-Time Cubes.

4.2.1 Marching Cubes 33

The Marching Cubes 33 algorithm (MC33) is used for the reconstruction of isosurfaces from volumetric datasets, i.e., from 3D arrays of data [17,57]. It uses the images obtained with the μCT to create a surface representation. Initially, these methods were applied for rendering in medical applications, however, they can be applied in many other areas, e.g., to obtain models to be used in structural analysis and 3D printing.

This technique uses a divide-and-conquer approach to locate the surface in a logical cube from eight pixels, four from one 2D slice and four from another adjacent slice/image. The algorithm determines how the surface intersects this cube and then moves, marches, to the next cube. As the name implies, there are thirty three different intersection patterns that a surface could present. Further information about the MC33 algorithm can be found in Section A.6.

4.2.2 Double-Time Cubes

Another alternative is to apply the Double-Time Cubes algorithm (DTC) which, according to Bruker, produces very similar results to the MC33 [45]. However, results show that the final mesh shows a reduction of 50% in the number of faces and a smoother surface, or boundary mesh, which is better for visualization. Nevertheless, the smoothed surface is produced without human interaction which might lead to uncontrolled loss of information.

4.2.3 Method Selection

Finally, both methods are compared in order to evaluate which one is more suited for this application. As mentioned before, the primary goal is to minimize losses of information along the process, so the final volume, or mass, of both structures for both methods was compared to the real value of the real specimen. Taking the cubic open-cell foam as an example, the values of interest can be analysed in Table 4.1. An error of 8.027% of the volume for the DTC is verified which is easily defeated by the MC33 with an error of only 1.560e−5%. The MC33 maintains the volume/mass constant and preserves more information. This can also be observed by the variation of the surface area[3] that shows a small change of 0.301% in contrast to 6.633% for the other method. Moreover, the number of faces and the file size are the double for the MC33 algorithm, as mentioned in Section 4.2.2. On one hand, more faces mean more details. On the other hand, the file is bigger and its processing time is going to be larger. Nevertheless, the high amount of details is preferred and the file can later be simplified on command and not just randomly by the surface reconstruction algorithm. Despite the given example being just for the open-cell foam specimen, the same results are observed for the closed-cell foam and cylindrical open-cell foam specimens.

Given the results are more satisfactory for the Marching Cubes 33, it is going to be used for all 2D slice sets/foams. Table 4.1 also provides the volumes of the other specimens for the MC33 algorithm with an error estimation considering the real foams' volumes/masses (Sec. 3.2.2.3). Given there is no information regarding the real surface areas, the variation included refers to the one obtained with the software. The values of that parameter for the cylindrical open-cell and closed-cell foam show a large, unjustified variation, however, when the geometries suffer a reduction in the amount of faces, the values become similar to what is expected. A reason for this phenomenon wasn't found, but the main hypothesis is that the large number of faces, 49 and 89 million for the cylindrical open-cell specimen and for the closed-cell specimen, respectively, might cause trouble in *Meshlab*. In any case, this effect was neglected since the main focus is the volume/mass.

Table 4.1: Comparison between the Double-time Cubes and the Marching Cubes 33 algorithms. The error in volume with respect to the real values is provided between brackets. The error in surface area is calculated with the values obtained with *CTAn*.

	Volume (mm^3)	Surface Area (mm^2)	Faces (M)	File (MB)
Cub.OC DTC	378.914 (8.027%)	3836.051 (6.633%)	12.769	623
Cub.OC MC33	411.412 (1.560e−5%)	4096.003 (0.301%)	23.230	1134
Cyl.OC MC33	341.393 (0.031%)	2057.574 (41.016%)	48.757	2380
CC MC33	473.842 (0.001%)	2051.678 (72.356%)	89.054	4347

[3]Surface area is obtained with CTAn, there is no way of measuring it in the real specimen.

4.3 Main Simplification Algorithms

Along with the problems regarding STL files, the algorithms or filters used for simplifying the meshes must also be understood before analysing the whole process, so, they are explained in the following sections. There are many strategies and software that could have been used, however, using *Meshlab*, the employed algorithms were the ones that presented the most consistent results [50]. The four main ones used were:

(i) Quadric edge collapse decimation;

(ii) Taubin smooth;

(iii) Close holes;

(iv) Discrete curvature calculation.

Each one was selected among many others mainly for its ability to cause meaningful change to the mesh while preserving the shape and not causing almost any shrinkage, i.e., volume reduction. There are several other operations that are applied to the model, however, they are quite simple and don't need much introduction.

4.3.1 Quadric Edge Collapse Decimation

The quadric edge collapse decimation algorithm is the most important for the simplification of the mesh, i.e., a reduction of the amount of faces. This technique is very important in the context of models built based on μCT-imaging since they are usually oversampled and very taxing for computers. It is able to perform the desired simplification while maintaining the volume of the model and keeping sharper features, to a certain degree. Such characteristics make it an ideal solution for the problem at hand. This algorithm simplifies the mesh based on Quadric Error Metrics (QEM), as opposed to others that use the geometric distance, which allows for the preservation of features with high curvature. Quadric Error Metrics are a measurement of error that determines how far a vertex is from an ideal spot and are found using the plane equation derived from a triangle (face) [58].

In order to perform the simplification, a mechanism named edge collapse is applied. Edge collapse, which can be denoted as $(\mathbf{v_1}, \mathbf{v_2}) \longrightarrow \overline{\mathbf{v}}$, moves the vertices $\mathbf{v_1}$ and $\mathbf{v_2}$ to the ideal position $\overline{\mathbf{v}}$, connects all their incident edges to $\mathbf{v_1}$ and deletes vertex $\mathbf{v_2}$ (Fig. 4.5). As a consequence, any edges or faces which have become degenerate (Sec. 4.1.2), i.e., which have collapsed, are eliminated [59]. There are also other methods for the simplification of a mesh, such as vertex clustering [60], vertex decimation [61], etc. The position of the remaining vertices can now be controlled to retain the geometry of the original model. For this reason, the quality of the simplified mesh is greatly dependent on final assigned position for each vertex. To calculate the optimal position, the point which minimizes the quadric error must be found [62].

The algorithm has many options and parameters which could be used. Therefore, in *Meshlab*, the parameters were selected based on the recommendations of the software, with boundary preservation, topology preservation, planar simplification, optimal positioning of simplified vertices, a quality threshold of 0.4 (0-1, 0.5 penalizes good faces) and the intended final number/percentage of faces. An analysis of the effect of different

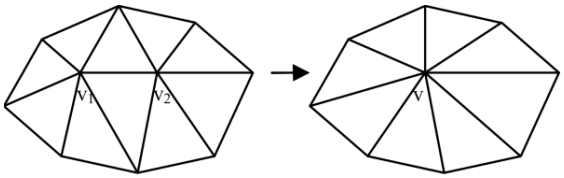

Figure 4.5: Edge Collapse [62].

values was not performed, however, it is important and should be the target of greater focus in the future.

To generalize the analysis of the foams in terms of the number of faces and to make it clearer for future work, the density of faces is used instead of the pure amount from this point onwards. For this purpose, the face density, ρ_{f}, is defined as the number of faces, N_{f}, divided by the volume of the bounding box, V_{BB} of each foam as:

$$\rho_{\mathrm{f}} = \frac{N_{\mathrm{f}}}{V_{\mathrm{BB}}}. \tag{4.2}$$

Results show that reducing the number of faces up to 98% of the initial number yields a minimal error in volume and surface area of around 2% and 10%, respectively, for the available specimens. The face quality, i.e., aspect ratio, was reduced due to the collapse of edges, which was handled with a smoothing operation described in the next section, where the analysis of the face quality is also performed.

4.3.2 Taubin Smooth

An inherent problem of approximating real geometries with a reduced number of faces is that the final result can be irregular and appear faceted. To reduce these problems, smoothing algorithms are introduced. The Taubin smoothing operation provides a method to regularize faceted geometries of arbitrary topology while keeping the changes in volume and in shape to a minimum, i.e., it doesn't produce shrinkage. Additionally, the face quality is also improved, making each face more regular and closer to an equilateral triangle [63, 64]. Here, it is given great importance due to the fact that it facilitates the application of other algorithms and prevents the genesis of subsequent errors, e.g., bad mesh simplification using the quadric edge collapse decimation (Sec. 4.3.1) and difficulty in FEM mesh generation.

This algorithm generalizes the classical discrete Fourier Analysis to two-dimensional discrete surface signals. Therefore, the problem of surface smoothing or fairing is reduced to low-pass filtering. The space of signals based on the surface mesh is decomposed into orthogonal sub-spaces associated with different frequencies, with the low frequency content of a signal regarded as subjacent data, and the high frequency content as noise. It removes high curvature variations by moving the vertices of the surface without changing the connectivity of the faces and maintaining the volume (and mass) almost unchanged [63].

The algorithm was applied in *Meshlab* using empirically selected parameters based on the recommendations of the software. They were selected so that no extreme changes to the model were verified. λ[4] was selected to be 0.5, despite higher values, e.g., 0.6, yielding

[4] λ is the scale factor for the shrinking step, where $0 < \lambda < 1$ (for $\lambda < 0$ and $\lambda \geq 1$ the algorithm

smoother surfaces, 0.55 for μ[5], due to $\mu < -\lambda$, and 10 smoothing steps/iterations. The theory of this smoothing process translates very well into reality. It manages to produce very minimal shrinkage, the shape is preserved and the number of faces remains the same. For example, applying this algorithm to the cubic open-cell and closed-cell foams produces a very small variation of volume of just 0.04% and 0.09%, respectively. Such range of values is negligible. Regarding the quality, the effects can be seen in Figure 4.6, a cut version of the closed-cell foam, where the application of the algorithm causes very visible changes to the quality of the surface making it more regular. Here, the quality is calculated as [65]

$$\eta = K \frac{inscribed\ radius}{circumscribed\ radius}, \tag{4.3}$$

where inscribed radius is equal to the radius of the largest circumference that fits inside a triangle, circumscribed radius means the radius of the circumference that contains the triangle vertices and K has been chosen so that the equilateral triangle has $\eta = 1$, which is the preferred configuration of each face and that maximizes the relationship between radii. In the histograms of Figure 4.6, there is a clear shift of the values towards levels of higher quality, i.e., faces with quality equal to 1, (the size of the bars of the histogram are scaled to allow for better visualization). The mean value changes from 0.75 for the initial mesh to 0.84 for the post smooth surface.

Yet, the effects of the Taubin smooth operation are not all positive. After smoothing, some faces become self-intersecting, however, this problem can be resolved by deleting them and applying the hole closing algorithm.

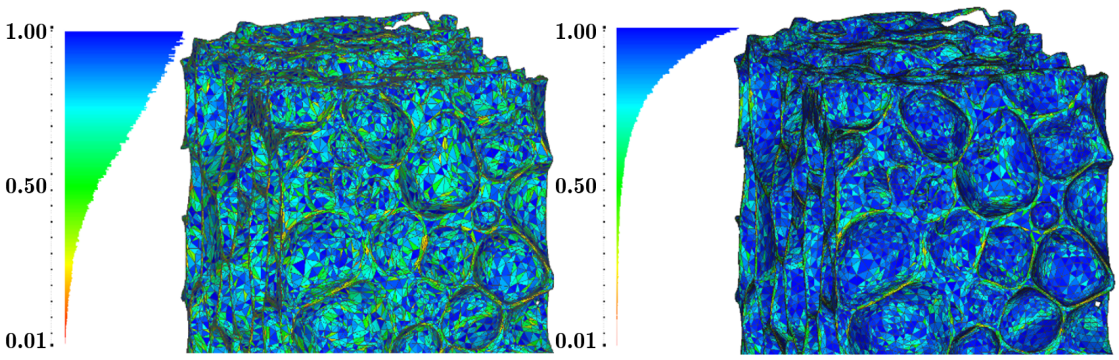

Figure 4.6: Comparison of surface quality before (left) and after smoothing (right) for the closed-cell foam specimen. Histograms bars are adjusted to a max size.

4.3.3 Close Holes

One of the most essential steps in simplifying and repairing the 3D models is to close the holes, which are a consequence of missing faces and one of the main discussed problems (Sec. 4.1.1), turning it into a closed manifold mesh. The elimination of such gaps is not a simple and follows the following strategy [55, 56]:

(i) Check for approved edges with adjacent faces;

enhances high frequencies instead of attenuating them).

[5] μ is the negative scale factor for the un-shrinking step.

(ii) Detection of gaps in the tessellated model;

(iii) Sorting bad edges into closed loop;

(iv) Generation of faces for the repair of gaps.

For the first step, a routine is used to check for approved edges, i.e., with no gaps next to them. Taking a face A, each of its edges are checked to verify if there is a coincident edge in the opposite direction. If so, it is stored under a temporary file as an approved edge. All the edges of all faces are checked with the same principle. If an edge in opposite direction is not detected, a gap has been found and that edge is stored in another temporary file. For the third step, all edges without adjacent faces are sorted into closed loops, one for each gap, and stored again in another temporary file.

Finally, after the closed loops are established, faces are generated to cover the holes. To generate the first face, the first two vertices in the first two edges in the temporary file, which holds the sorted closed loops, is connected to the first vertex in the last edge (Fig. 4.7). Its orientation is checked and approved if correct. To generate the next faces, the same procedure is followed, but only with the remaining edges and vertices. There are some cases of gap closing that need special attention, e.g., two or more gaps formed from a coincidental vertex or two faces sharing a common edge, but they are not clarified here [56].

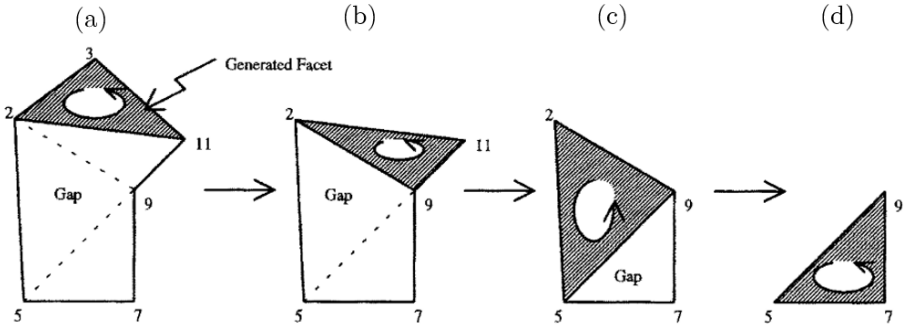

Figure 4.7: (a) First face generated. (b) Second face generated. (c) Third face generated. (d) Fourth face generated [55].

4.3.4 Discrete Curvature Calculation

Because of the definition of the 3D models based on triangle surface meshes, there is no intrinsic curvature. They are inherently discrete and each face is planar. However, the discrete curvature calculation algorithm is able to extract an approximation based on "averaging Voronoi cells and the mixed Finite-Element/Finite-Volume method" [66]. The obtained curvatures by this calculation allow the detection of very small features, which could cause problems during meshing for finite element analyses, and also find small defects and cracks in the cell walls, that could significantly change the strength of a foam. Therefore, its usage provides more control and flexibility in the process, favouring a more in-depth analysis of the effect of such defects by comparing the same structure with defects and no defects (Sec. 4.4).

This algorithm was applied in *Meshlab*. There are four options for calculating the curvature: mean curvature; gaussian curvature; RMS (Root Mean Square) curvature; and absolute curvature. In this case, RMS was preferred because it showed good results. In this software, the curvature is calculated for each vertex and saved in the "vertex quality" field. From the stored values, vertices can be selected based on their curvature values. For example, in order to eliminate very small features, all vertices with "quality" equal or higher than 300[6] were selected and eliminated (working in millimetre). Another option is to select and eliminate all vertices with curvature higher than 30-40 (empirical values) in order to eliminate the areas of small cracks and defects on the cell walls for subsequent remeshing. Many other vertices could also be unintentionally included in the selection with the curvature, however, it can also be easily solved with the hole closing algorithm. Moreover, the software not only selects the vertices but also the faces which contain the vertices. The condition "Inclusive Selection" was also turned on for every selection of the vertices because that way only the faces which had all three vertices pass the imposed condition would be selected. Therefore, ensuring that every selected face is, in fact, a area of high discrete curvature and not just small local variations.

4.4 Simplification Procedure

The principle idea of this section is to demonstrate a procedure that is not only simple and easy to replicate, but also meaningful for the type of application. As a consequence, it must be able to eliminate all the problems regarding STL meshes mentioned above and reduce the number of faces while preserving their shapes [67]. In order to complete this task, several functions/algorithms are applied, some of which have already been described in previous sections, and the results are evaluated in terms of volume and surface area preservation, the quality of the final mesh and the point to point difference between initial and final meshes. The procedure is detailed in the next sections giving an overview of the application and order of application of the different algorithms and their impact on the boundary meshes. The final result of this process are simplified and clean surfaces, or boundary meshes, which are ready to be introduced in finite element meshing software.

To begin with, it is necessary to define the end goal. What is a valid geometry/mesh and how is it defined? In this case, as well as in 3D printing and for medical applications, the final surface mesh needs to fulfil certain requirements:

- Closed manifold mesh (Sec. 4.1.4), consequently, watertight;
- Free from self intersecting faces (Sec. 4.1.3);
- Reduced number of faces or reduced face density;
- Geometrically and topologically identical to the real foams;
- Good quality, i.e., faces with a good aspect ratio and a low distortion/curvature.

Now that the goal is clear, a procedure can be more clearly defined. So as to have a complete analysis of the foams and of the influence of the process on the results, two

[6]Empirical value. Other values could also be used.

different procedures are described. These procedures are more focused on simplifying the closed-cell foam since it is more complicated and nothing more than an extension of the preparation of the open-cell foam. Similar or better results could probably be obtained in another manner or in another order, however, the described procedures showed moderate implementation difficulty as well as consistent results.

4.4.1 Procedure 1: Plain Simplification

As described in Figure 4.8, the first step is to apply the Taubin smoothing algorithm. As previously mentioned (Sec. 4.3.2), it smooths the surface and improves the quality of the faces while minimizing the shrinkage and preserving the shape. Despite its application as a starting point for the process not being necessary, the resulting surface mesh is more regular and minimizes the posterior occurrence of errors.

Secondly, all self-intersecting faces, non-manifold edges and high discrete curvature vertices (values above 300 for very small features) must be deleted. These cause problems with volume calculation, finite element mesh generation, development of kinks after simplification and don't allow for the surface to be closed.

Afterwards, some small problems regarding the gaps and the irregularities around them are easily noticeable. These irregularities are detrimental to the surface and cause many problems when closing the holes or when the mesh is simplified. For this reason, the borders of the mesh, i.e., the borders of all holes/gaps, are deleted four to six times. This step might appear contradicting to the general purpose of the whole process, which is to minimize changes to the initial structure, but, since the faces are very small, the removed data is minimal and the benefits appear to be greater than the downsides. It is, nevertheless, an optional step and can be skipped.

The next stage is to eliminate all non-manifold vertices (Sec. 4.1.4), which don't have much meaning and don't allow the closure of the gaps associated to them. At this point, the surface should be free of errors, open, with a very high number of faces and ready for the application of the hole closing algorithm. Due to the high amount of detail, small distortions and limitations to the algorithm, the process can't be completed in just one step. Its further application results in nothing and the mesh remains open. To solve this issue, the borders are again deleted, this time one to four times (other values can be used as well), other errors like non-manifold vertices are deleted yet another time and the function that closes holes is employed again. Closing all the holes is, in general, an iterative process. With each iteration more and more holes should be closed until the surface becomes a closed manifold mesh (watertight). Manual intervention might be required in more delicate areas where the user must select and delete highly distorted borders (around the holes). In case some holes are very hard to close, *Meshmixer*[7] can be used. It has more complex hole closing algorithms which might be helpful in some cases.

When the mesh is watertight, the quadric edge collapse decimation simplification algorithm is applied following the instructions given in Section 4.3.1, reducing the number of faces to the desired amount and limiting changes to the topology and shape of the structure. This simplification technique could also be applied before the surface is treated and made watertight, but the process of cleaning errors after simplification could lead to bigger changes to the geometry. Subsequently, the Taubin algorithm is applied again, the

[7]Meshmixer, Autodesk, www.meshmixer.com

self-intersecting faces, non-manifold edges and high discrete curvature vertices resulting from the simplification and smoothing must be deleted and the holes closed as described above.

Finally, the surface mesh should be clean and simplified, however, small components left out by the procedure could persist. These can be eliminated, but attention must be paid in order not to eliminate small elements that constitute the smaller closed pores. In this case, all pores and small components with a diameter inferior to 0.4 mm were deleted. At this point the final surface is simplified to the desired extent. It should faithfully represent the original surface even including the very small defects and imperfections in the cell walls which connect different pores, in the case of closed-cell foams. It is known that the physical properties of a foam are a direct consequence of the micro-/macro-structure [41]. So, their presence is normal, as verified in some articles, and desired in terms of fidelity to reality [68]. However, small holes are sure to originate kinks during finite element analyses. For this reason, procedure number 2 is introduced.

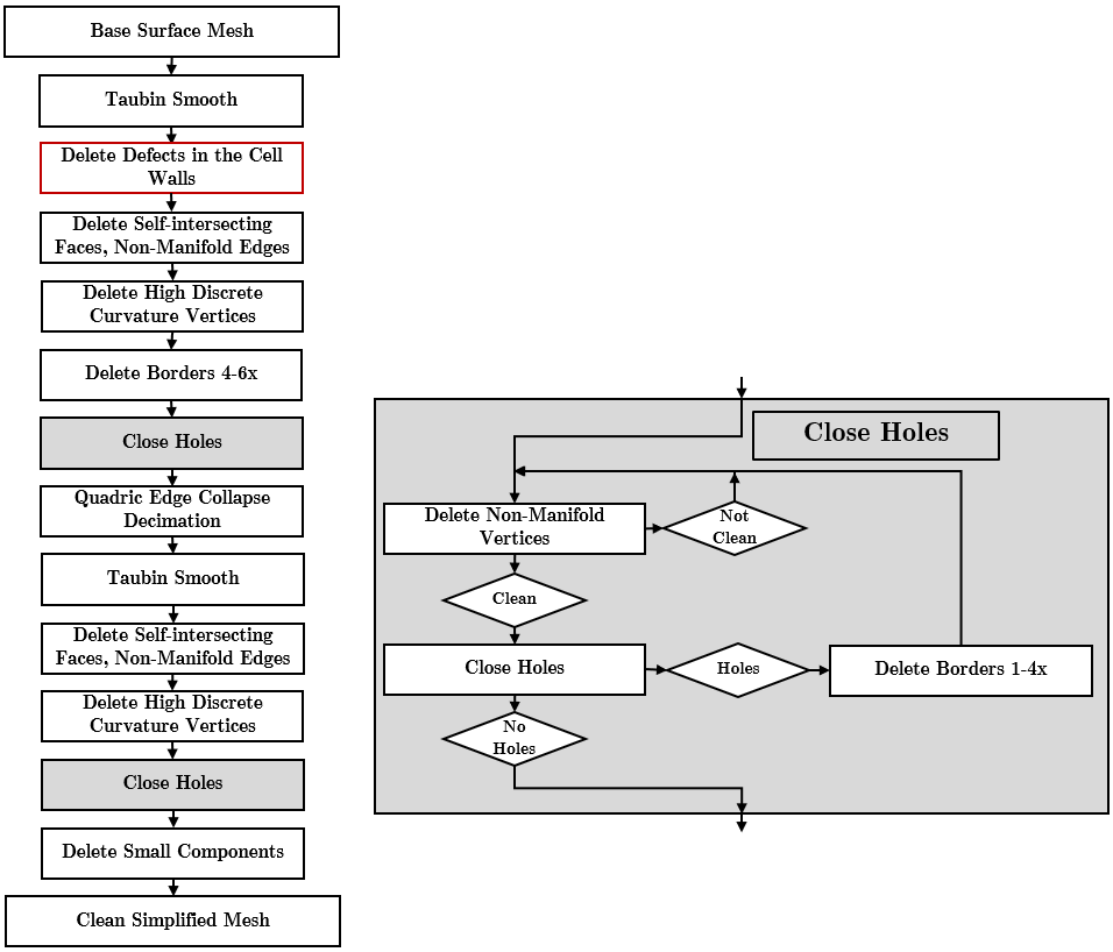

Figure 4.8: Procedure pipeline. The step represented in red is only added for Procedure 2 (clean small defects and cracks).

4.4.2 Procedure 2: Elimination of Cell Wall Holes

It seems reasonable to extend the previous procedure to eliminate the aforementioned defects, or structural imperfections, in the cell walls and obtain an even smoother and cleaner surface which will be more stable during analysis. Having both types of surface allows the observation of the magnitude of change caused by their elimination, how the results might be dependent on the process of obtaining and processing the surfaces and if there should be a stronger process standardization across this scientific field.

Eliminating the small imperfections in *Meshlab* is a time-consuming process and depends on the experience of the user with the software. Nevertheless, the procedure is described thoroughly for the closed-cell foams, given it is useless in the case of the open-cell foams because they show, in comparison, a low number of defects. To accomplish this objective, a method which detects their presence is required, given their position is completely arbitrary. Observing the defects and their shape, it can be verified that the areas involving them have high curvatures. Therefore, by taking advantage of this property, the faces can be deleted, leaving one gap on each side of the corresponding cell wall, which are later remeshed/fixed. For this purpose, the discrete curvature algorithm is introduced again in the whole process as shown in Figure 4.8, maintaining the rest of the process pipeline unchanged. This time, all vertices with curvature values above a given threshold, usually around 30 to 40[8] when working with millimetre as the main unit, are selected in order to capture all the intended areas (Sec. 4.3.4). For this reason, the user might be required to test different threshold values and check which works the best. During the selection using the vertex quality selection menu, the option "Inclusive Selection" must be activated which only allows for faces which have all three vertices with high curvature to be selected. In simple terms: the curvature is calculated for each vertex; the values are stored in the field of vertex quality; the vertices must be selected using a given threshold; *Meshlab* also selects the faces associated with the vertices; and the "Inclusive Selection" option only allows the faces which have all their three vertices within the selection range values to be selected. The user must be especially attentive to the keywords face and vertex in the explanation above. At this point most areas regarding defects have been selected along with many other smaller areas can be deleted, which should be easily dealt with using the hole closing algorithm. Additionally, when working with specimens which have been cut and, therefore, have flat sides, all vertices and faces (the enunciation of both is intentional) on those sides must be deselected before eliminating because it is very difficult to deal with the generated holes in future steps of the procedure. From this point onward, it continues as defined above with the exception of the necessity for more manual intervention in areas which arent't completely captured by the discrete curvature algorithm. The difference between Procedure 1 and Procedure 2 is indicated in Figure 4.9.

4.5 Results

Up to this point, each phase was evaluated separately giving an idea about its effects on the images or on the 3D model. So, the next step is to evaluate how all of them develop together and if the final result is satisfactory. For this purpose, the assessment is based on the foam's mass/volume (quality indicator discussed in Section 3.2.2.3), the variation

[8]Empirical values. Others could be used.

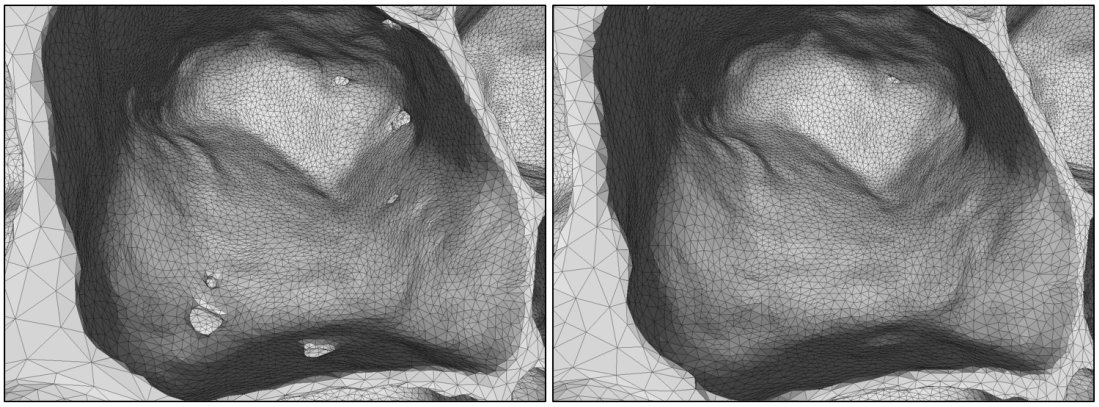

Figure 4.9: Procedure 1 with defects (Left) and Procedure 2 without defects (Right).

in surface area comparing to the initial values calculated in the analysis of the slices and, finally, the average distance between the final simplified mesh and the initial mesh, obtained with the slices, calculated with the Hausdorff distance algorithm and the distance from a reference mesh algorithm, which are both provided by *Meshlab*. An analysis of the file size was also performed in order to indirectly evaluate the computational effort of processing the foams.

4.5.1 Mass/Volume and Surface Area

The analysis of the variation of the foam volume and surface area was performed for the closed-cell foam with respect to the number of faces. Due to the large number of faces of the closed-cell foam, i.e., 89 million, which corresponds to a face density of 24450 faces per mm^3, and, consequently, the high computational effort associated with them, the foam was reduced to a section of 8 by 14 mm which extends in the z direction by the original amount of 15.571 mm. The new values of volume and surface area of the foam considering the same set of parameters for the image analysis as the whole foam, i.e., threshold value of 47 with no closing operation and no despeckle operation, are 219.381 mm^3 and 3759.213 mm^2. Reducing the size of the specimen should not be problematic since it is just used as a mean to evaluate the variation caused by the process of obtaining the simplified 3D model in the values and not because of the absolute values themselves. In addition, the focus of this section is a foam which has been minimally processed, i.e., Procedure 1, where the smaller defects weren't removed as shown in the last few paragraphs of the last section. This decision is mainly due to the fact that the results are similar and that the variation in volume/mass for Procedure 2 is minimal, about 0.1%. The effects of the elimination of the defects are further discussed in Section 5.5.2.2.

In this case, the error in volume increases almost exponentially for decreasing face densities hitting a maximum of around 2% for 286 faces per mm^3 or 500 thousand faces, which corresponds to a reduction of about 99% of the initial amount, 26136 faces per mm^3 or 45.7 million faces (Fig. 4.10). Regarding the surface area, a peak error of 43% is verified for the initial density of faces, however, the value converges to the value calculated by *CTAn* for smaller densities. A reason for this outcome was not found.

In the case of the cubic open-cell foam, the whole foam was used. The volume

that describes it is 411.985 mm^3 , which was calculated through the real mass (Table 3.1). A threshold of 91 and no closing or despeckle operations were selected as the preferred parameters which yielded a volume of 411.412 mm^3, i.e., only a slight variation of 0.139% to the real value, and a surface area of 4108.292 mm^2 before simplification. Afterwards, Procedure 1 was applied. Procedure 2 doesn't bring any major advantage when simplifying open-cell foams due to the lack low number of defects. Results show a similar behaviour to the closed-cell foam for the volume error with a maximum value of around 1.8% for a density of 50 faces per mm^3 or 500 thousand faces, which corresponds to a reduction of about 98% of the initial amount, 2341 faces per mm^3 or 23.2 million faces (Fig. 4.10). The error of the surface area shows a more unstable development, where it initially increases to a maximum of about 8% and, subsequently, slightly decreases [9].

Finally, it can be concluded that the volume and, therefore, the mass evolves in a predictable way, showing low errors even for very high reductions of the number of faces for both open and closed-cell foams. The effect of the procedure on this parameter was minimal, so, it can be considered successful. On the contrary, the surface area is more unstable and there are some problems when calculating it. Even though it is not an essential parameter, more time should be dedicated to its analysis in the future. Regardless, the simplification of the meshes to very low levels still only exhibits a maximum error of 10%, which is acceptable.

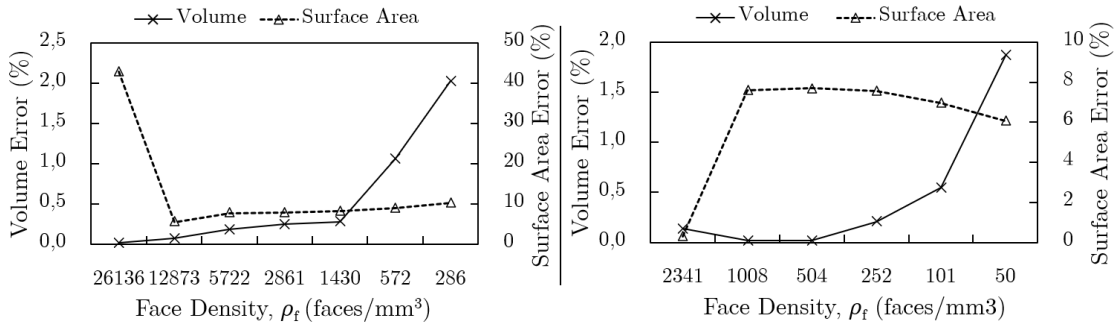

Figure 4.10: Error of the volume and surface area with respect to the density of faces for the closed-cell foam (left) and the cubic open-cell foam (right).

4.5.2 Distance Between Meshes

The analysis of the volume and the surface area is useful, however, it is not enough to confirm that the 3D models maintained their shape. For this reason, the Hausdorff distance algorithm and the distance from a reference mesh algorithm are applied, which provide statistics about the error distribution regarding the distance between a mesh to be measured and a reference mesh [18, 50].

The introduction of the Hausdorff distance algorithm that provides the actual geometric difference between the original and the simplified meshes is strategic for the design of better simplified meshes. Such tool allows the user to have actual control over

[9]The cylindrical open-cell foam is not included in the following analysis since it shows similar results to the cubic one and was mainly used to verify the effect of the different scanning parameters in the threshold in Section 3.2.2.3.

the process and be able to gather more precise conclusions. Therefore, in such a context, the Hausdorff distance is very relevant. The approximation error between two meshes may be defined as the distance between corresponding sections of the meshes. Given a sampling point p on a surface S, the distance $e(p, S)$ is obtained as [18]

$$e(p, S) = \min\, d(p, p'), \quad p' \in S, \tag{4.4}$$

where d is the Euclidean distance between two points. The one-sided distance between two surfaces S_1, S_2 is defined as

$$E(S_1, S_2) = \max\, e(p, S_2), \quad p \in S_1. \tag{4.5}$$

The definition of the distance is not symmetric and, in general, $E(S_1, S_2) \neq E(S_2, S_1)$. The two sided Hausdorff distance is then obtained by taking the maximum of $E(S_1, S_2)$ and $E(S_2, S_1)$. For a uniformly sampled set of distances, the mean distance E_{m} between surfaces can be calculated as

$$E_{\mathrm{m}}(S_1, S_2) = \frac{1}{A_{S_1}} \int_{S_1} e(p, S_2)\; ds, \tag{4.6}$$

where, A_{S_1} is the area of surface S_1.

The Hausdorff distance was calculated using the aforementioned principles for the closed-cell foam for several levels of face densities using *Meshlab* by sampling the vertices, faces, edges. The number of samples was selected to be equal to the number of vertices, ≈ 23 million, of the reference mesh, i.e., the initial mesh without any filter or smoothing operation. Given this method provides the one-sided distance, the distance calculations were done for both sides and averaged, in order to facilitate the evaluation. In Figure 4.11 the evolution of the mean is represented with respect to the density of faces. For higher levels, the mean shows a almost linear behaviour, however, it drastically increases for lower levels. Even for a simplification of 286 faces per mm^3 or 500 thousand faces, i.e., a reduction of 99%, the maximum distance/error is only around 0.032% of the diagonal of the bounding box, which corresponds to about 0.07 mm in real measurements.

One of the most extreme examples can be visually analysed in Figure 4.12, where a simplified surface of 500 thousand faces, i.e., 286 faces per mm^3 and approximately a 99% reduction, was measured in comparison to the reference mesh. Here, all the distances are positive since the Hausdorff method always gives the absolute distance. The histogram with the colour map and the coloured mesh provide a very useful tool to analyse where the biggest differences appear. Here, the areas where the foam was cut show the largest variations in shape, while the rest maintain the initial format very well.

The same procedure was applied to the open-cell foam with a number of sampling points equal to the number of vertices of the foam, 12 million. The reference mesh was again the initial surface without any sort of processing. Figure 4.11 shows that the error, i.e., the mean distance between the meshes as a percentage of the bounding box's diagonal, has a similar behaviour to that of the closed-cell foam. It is close to linear for higher levels of density, however, in the case of higher levels, the error grows more intensively. Still, even for a density of 50 faces per mm^3 or 500 thousand faces, the error is only about 0.016%, which corresponds to 0.006 mm. For this case, the distribution of the Hausdorff distance and its visual representation is given in Figure 4.13.

The second applied algorithm, Distance from Reference Mesh, to test the similarity of the processed meshes to the initial one is very similar to the Hausdorff distance. The

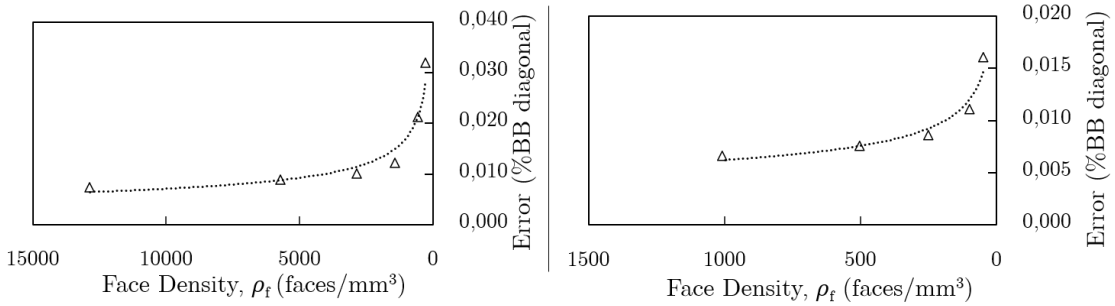

Figure 4.11: Mean of the two-sided Hausdorff distance of the cut closed-cell foam (left) and of the cubic open-cell foam (right) plotted with respect to the face density.

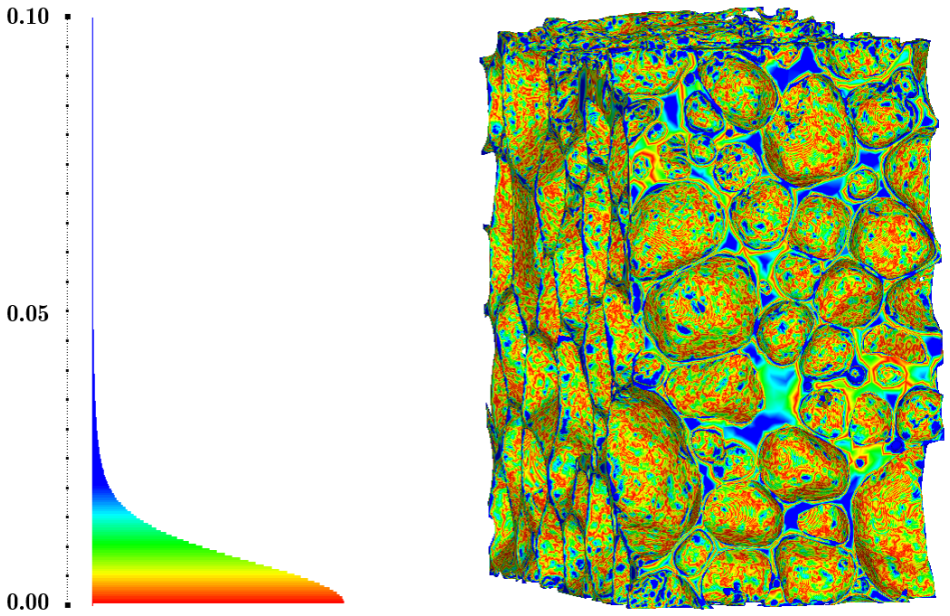

Figure 4.12: Visual representation of the Hausdorff distance of the cut closed-cell foam with 500 thousand faces, i.e., 286 faces per mm^3 and a 99% reduction.

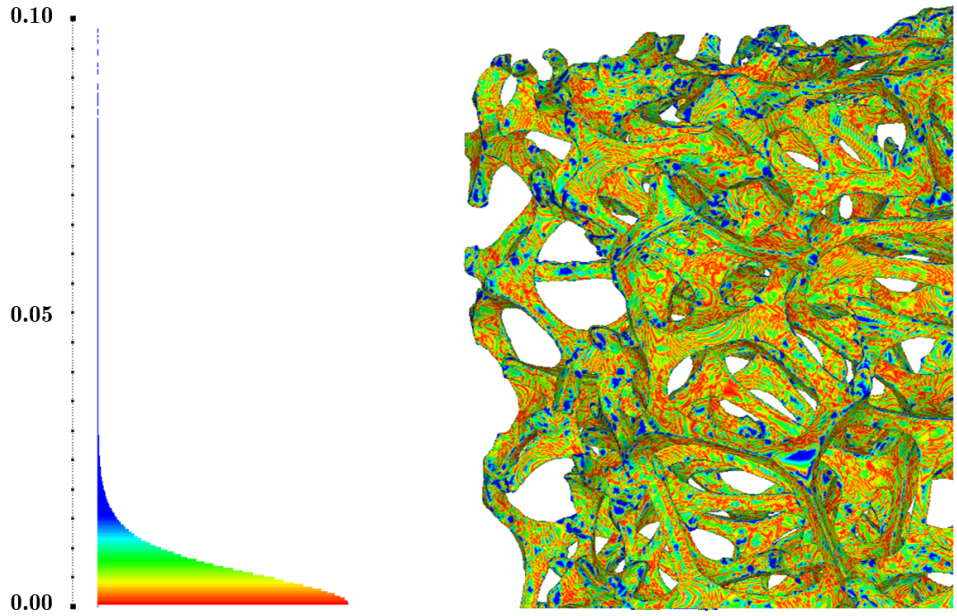

Figure 4.13: Visual representation of the Hausdorff distance of the cubic open-cell foam with 500 thousand faces, i.e., 50 faces per mm^3 and a 98% reduction.

main difference is that it calculates the signed distance, i.e., positive or negative, instead of the absolute value. This feature allows to better understand where and how the mesh deviates from the original shape. This technique works with the same principles as the previous one, however, the sampling is done vertex to vertex instead of uniformly distributed sampling points and the distance is signed.

Similarly to the calculation of the Hausdorff distance for the closed-cell foam, the initial unprocessed mesh was taken as the reference. The results for every calculation show a normal distribution and the mean is always very close to zero, therefore, the mean value is complemented with the standard deviation. As it can be seen in Figure 4.14, the mean and the standard deviation shift lightly for high face densities, however, for very low densities the mean starts to move away from zero and the deviation increases much quicker. For example for a density of 286 faces per mm^3 or 500 thousand faces (99% reduction), the mean error has a value of about -0.002% with a standard deviation of 0.045%, which means that 68.2% of the distances calculated for the sampling points are between -0.047% and 0.043%. The obtained values are, therefore, very small even for a very simplified structure.

Figure 4.15 visually represents the example given above. Since the distance is signed, there is a greater awareness about where the shape is changed and in what direction. In this case, the representation is of the distance calculated with the final mesh as the reference and the initial as the one to be measured. The only foreseeable consequence is that distances are inverted to what is expected, therefore, areas in the red spectrum represent points where the final mesh stays above the initial and in the blue spectrum the inverse. It should be remembered that the output of this algorithm depends on which of the two meshes in study is selected to be the reference. The red areas are mostly seen in planar surfaces, which are artificial and a consequence of cutting the foam, where the

smoothing of the edges of the pores appears to cause these surfaces to lift. Blue areas are especially seen in thin walls and edges where their smoothing causes some contraction and rounding.

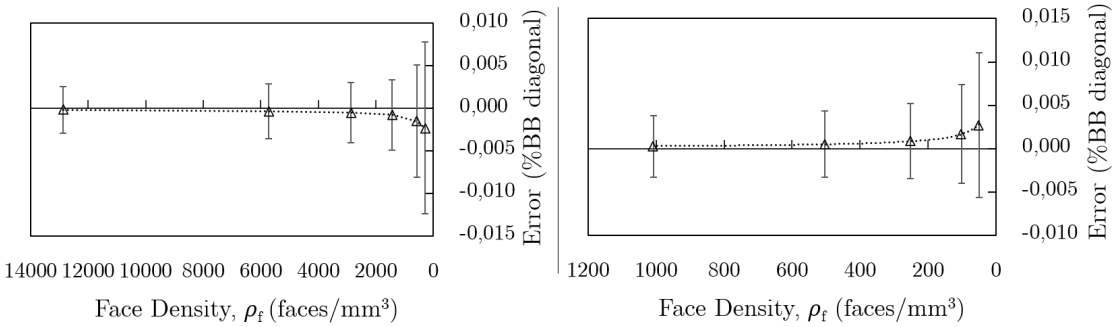

Figure 4.14: Distance from reference mesh of the cut closed-cell foam (left) and of the cubic open-cell foam (right) plotted with respect to the face density.

The calculations were repeated for the open-cell foam, which shows very similar results to the closed-cell. The evolution of the error is close to linear for high face densities, however, it starts to move away from zero towards positive numbers for low densities, along with a great increase of the standard deviation (Fig. 4.14). Ultimately, the error is quite low, representing just around 0.003% with a standard deviation of 0.02% for a foam with 50 faces per mm^3 or 500 thousand faces (98% reduction). The distance distribution for this case is shown in Figure 4.16.

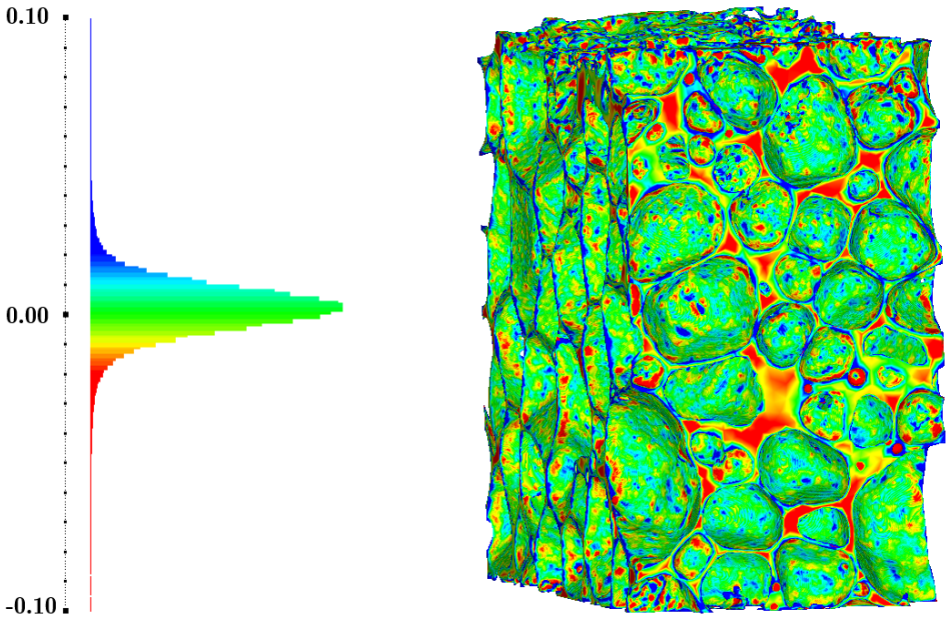

Figure 4.15: Visual representation of the distance from a reference mesh of the cut closed-cell foam with 500 thousand faces, i.e., 286 faces per mm^3 and a 99% reduction.

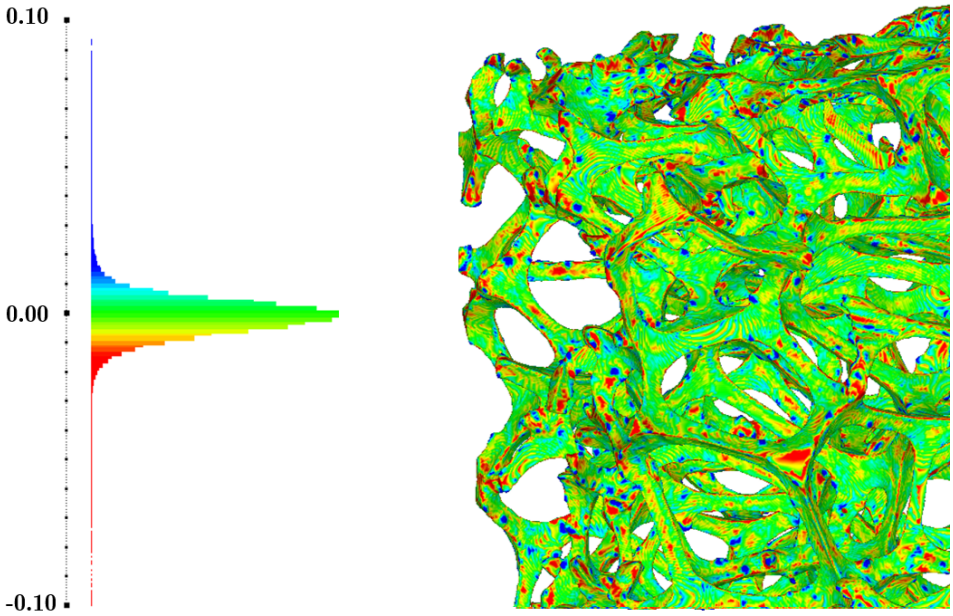

Figure 4.16: Visual representation of the distance from a reference mesh of the cubic open-cell foam with 500 thousand faces, i.e., 286 faces per mm^3 and a 99% reduction.

4.5.3 File Size

In an attempt to indirectly investigate the computational effort, the file size was going to be studied with respect to the amount of faces. However, the STL format stores the information regarding each vertex, increasing the file size linearly (Sec. 4.1). For this reason, instead of analysing with regard to the number of faces, the density is preferred. The file size shows a linear correlation with the foam density for both types, closed and open-cell. However, the tendency line for the open-cell foam is steeper, showing larger sizes than the closed-cell for the same density values. The value or R^2 is 1 which is expected due to the definition of STL files.

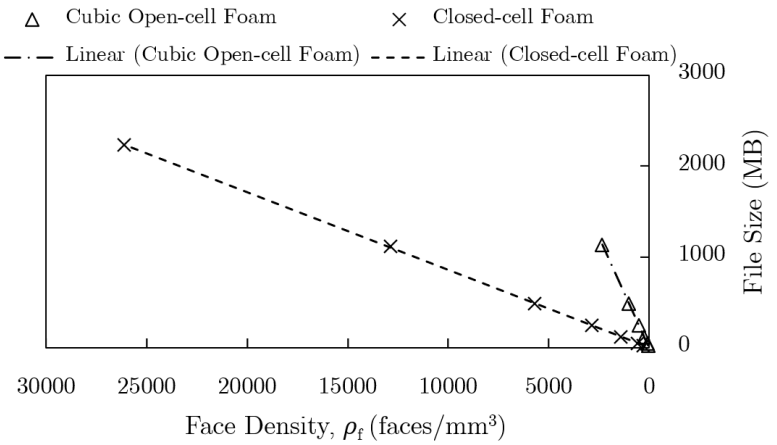

Figure 4.17: File size and face density of the open-cell foam and the closed-cell foam.

Intentionally blank page.

Part III

Numerical Modelling, Analysis and Results

Chapter 5

Numerical Modelling and Analysis

In the past few years, there has been a greater interest in obtaining 3D models for Finite Element Analysis (FEA) from μCT scans. Hence, there are several methods described by many other authors [7–14]. Different approaches could yield different results, therefore, it is difficult to define a correct procedure. For that reason, two different alternatives to obtain the 3D models have been presented.

In the following sections, the obtained 3D models derived from the μCT scans are analysed. The main purpose is to evaluate the effective relative Young's modulus with respect to the relative density of the different types of foams when submitted to a compression loading scenario and, for the closed-cell foam, the influence of the procedure from the 2D slices to the simplified 3D model in the results. Since the presence of small structural imperfections could change the mechanical results, it is relevant to analyse how different approaches deal with them and how large an impact they have. The values obtained from the structural analyses are then compared to theoretical, numerical models, as well as some based on Representative Unit-Cells (RUC) and experimental results in order to evaluate their accuracy and to have a better understanding of what advantages or disadvantages the models bring to the table. Firstly, the meshing of 3D models for FEA based on boundary tessellated meshes in the STL format is discussed. Afterwards, the boundary conditions and loads are introduced, explaining how the important parameters are obtained and calculated. The study of the mesh refinement is also presented. The cubic open-cell foam specimen is assessed simply, whereas the closed-cell foam specimen is analysed for the two different procedures, i.e., with defects and no defects. The influence of the morphological operations is also analysed for the latter. Due to some limitations, the closed-cell foam is also divided into octants in order to study some unwanted effects. To conclude, the Poisson's ratios and the anisotropy of the specimens are evaluated, providing a better sense of the specimens' behaviours.

5.1 Analytical Models

In the literature, there are several models which attempt to describe foams and their effective properties, more specifically the Young's Modulus, by associating them to the relative density (Tables 5.1 and 5.2). These models are relevant in the context of this

dissertation, given they provide a basis for comparison for the results obtained with the procedures which have been previously described.

Throughout the years there have been many attempts to characterize foams, metallic or polymeric. For this reason, there are models based on several deformation mechanisms, for example, edge stretching and cell-wall bending, axial and shear deformation, etc. Many authors provided their conclusions, allowing for a large, differentiated and not always correct database [69–77]. Table 5.1 summarizes all the theoretical models considered in this work for both types of foams, open-cell and closed-cell. Other models based on numerical approaches can be found in Table 5.2. In addition, the rule of mixtures with parallel association, as in composite materials, is also used, which provides the upper limit for the values of Young's modulus. The series association isn't discussed since air has a null value of stiffness, which would then yield a null stiffness for the "composite" [20, 78–80].

Table 5.1: Theoretical Models for open-cell and closed-cell foams.

Foam Type	Author(s)	Young's Modulus	Poisson's Ratio
Open-cell	Dement./Tarak. [81]	$\frac{E}{E_s} = \frac{4\sqrt{2}}{9}(\frac{\rho}{\rho_s})^2$	-
	Warren/Kraynik [82]	$\frac{E}{E_s} = 0.979(\frac{\rho}{\rho_s})^2$	-
	Zhu et al. [83]	$\frac{E}{E_s} = \frac{1.009\overline{\rho}^2}{1+1.514\overline{\rho}}$	$\nu = 0.5\frac{1-1.514\overline{\rho}}{1+1.514\overline{\rho}}$
Closed-cell	Renz/Ehrenstein [84]	$\frac{E}{E_s} = 0.33\frac{\rho}{\rho_s}$	-
	Gibson/Ashby [5]	$\frac{E}{E_s} = \phi(\frac{\rho}{\rho_s})^2 + (1-\phi)\frac{\rho}{\rho_s}$	-
	Christensen [74, 85]	$\frac{E}{E_s} = \frac{2(7-5\nu)}{3(1-\nu_s)(9+5\nu_s)}\frac{\rho}{\rho_s}$	$\nu = \frac{1+5\nu_s}{9+5\nu_s}$
	Mills/Zhu [86]	$\frac{E}{E_s} = 0.06(\frac{\rho}{\rho_s})^{1.06}$	-

Table 5.2: Numerical Models for open-cell and closed-cell foams.

Foam Type	Author(s)	Young's Modulus	Poisson's Ratio
Open-cell	Chen [87]	$\frac{E}{E_s} = 1.49(\frac{\rho}{\rho_s})^3$	-
	Rob./Garb. [88]	$\frac{E}{E_s} = 0.93(\frac{\rho}{\rho_s})^{2.04}$	-
	Gan et al. [89]	$\frac{E}{E_s} = \frac{\overline{\rho}^2}{1+6\overline{\rho}}$	-
Closed-cell	Simon/Gibson [90]	$\frac{E}{E_s} = 0.3163(\frac{\rho}{\rho_s})^2 + 0.3188\frac{\rho}{\rho_s}$	-
	Rob./Garb. [88]	$\frac{E}{E_s} = 0.563(\frac{\rho}{\rho_s})^{1.19}$	-

5.2 FEA Meshing

Usually, in finite element analyses the parts which are going to be studied are modelled in a NURBS based format [53], i.e., every feature is defined parametrically as in CAD,

and they can be directly inserted into most simulation software. However, the foam parts in this work are saved in a different format, STL, which lacks some information, in comparison to the above mentioned, and is not recurrently accepted as an input format. Therefore, there are at least two ways of solving this situation (Fig. 5.1):

1. Transform an STL model into a parametric model, in some CAD format, and use the final result as the input;

2. Skip the transformation and use the STL directly in an appropriate programme.

The first option seems feasible at first, but for such complex geometries there are some problems or limitations which might arise, given there is a high difficulty in reconstructing the models as continuous and parametric surfaces. For example, *Solidworks* from *Dassault Systemes*[1] was tested for this purpose using the *ScanTo3D* tool or by importing and converting the geometry to a NURBS based solid, which has a face limit of around 500 000. In spite of working, the final geometries might have several flaws, unconnected faces and the files are usually extremely heavy due to the large number of faces and the format definition itself. An initial file with 500 000 faces might take several hours to save in a modest computer. In the case of *Fusion360* by *Autodesk*[2], the situation is similar. It provides some mesh manipulation tools, but it is limited to 500 000 faces. Other methods were tested, however, the results weren't satisfactory.

The second option might, therefore, be ideal if there are sufficient resources in order to process and use the STL files. Fortunately, software like *Gmsh*[3] accept STL files and can create finite element meshes. Gmsh is a versatile software. It can be readily used by

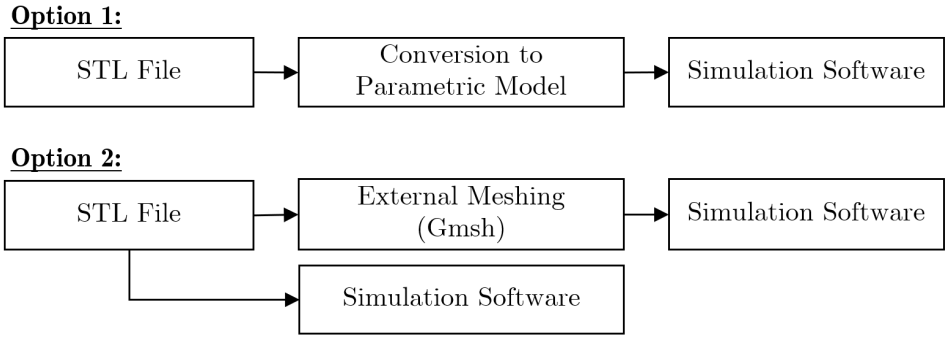

Figure 5.1: Input and Analysis paths.

anyone and it can output finite element meshes for different solvers [65,91]. The user can not only use the graphic interface, but also the available scripting options for repetitive and extenuating work. Here, the graphic interface was preferred. In order to obtain a FEM mesh the following four steps were followed:

(i) *File* → *Merge* → *Select STL File*

(ii) *Modules* → *Geometry* → *Elementary Entities* → *Add* → *Volume*

(iii) *Modules* → *Mesh* → *3D* → *Optimize 3D*

[1]Solidworks, Dassault Systemes, www.solidworks.com
[2]Fusion360, Autodesk, www.autodesk.com/products/fusion-360/overview
[3]Gmsh, gmsh.info

(iv) *Files → Export → Select Output Format*

The described steps take a surface mesh, or boundary mesh, in STL format and create a volumetric finite element mesh which uses the faces of the initial boundary mesh as the external faces of the created tetrahedrons (3D elements), i.e., the creation of the 3D elements is tied to the boundary mesh, which could be considered a limitation.

In some cases, the software might not be able to generate a mesh and the process fails, however, the problem is usually easily fixable. The most common errors are the presence of self intersecting faces and very small angles between faces due to very small features, therefore, both originate from bad processing, which was described in previous chapters. Nevertheless, the file must be edited again in *Meshlab*. The self intersecting faces and areas with very high curvature, usually above 500 (empirical value) using the Discrete Curvature algorithm in millimetre (Sec. 4.3.4), must be deleted and the new holes closed. Finally, the last step is to export in the desired format. Given the fact that in this project the preferred simulation software was *ABAQUS*[4], by *Dassault Systemes*, the output format selected was INP.

This process has two main problems. Firstly, both the volumetric mesh as well as the boundary mesh are exported, which is problematic for simulation, but it can be easily solved by selectively deleting elements in ABAQUS. Secondly, the final mesh is conditioned by the initial boundary mesh, i.e., the exterior surface is maintained and the interior mesh, or 3D elements(tetrahedrons), is generated with respect to it. Because of the last aforementioned problem, optimizing and creating a high quality STL takes on greater importance (Sec. 4.3.2). A regular initial boundary mesh results, therefore, in a regular FEM mesh. In addition, the mesh refinement is conditioned requiring manual intervention during the simplification of the 3D model as described in Chapter 4.

Lastly, C3D4 elements were used for the finite element analysis, i.e., four-node linear tetrahedral elements, which is the standard used in *Gmsh*. Further types of elements should be investigated in future research [14].

5.3 Boundary Conditions and Properties

In order to analyse the specimens, a loading scenario with Symmetry boundary conditions with an Imposed Displacement (SID) was chosen. It involves enforcing a displacement on one of the sides of the specimens, assuming a shape similar to a rectangular cuboid, and symmetry conditions on three other sides, leaving two sides in distinct directions which can expand or contract freely. Such a configuration allows the calculation of the Poisson's ratios by measuring the displacements (Fig. 5.2). Contrary to Symmetry boundary conditions with a Prescribed Force (SPF), where a force is imposed on one of the sides, SID provides better load homogeneity, especially since the geometries based on μCT scans are irregular [19, 20]. Imposing a displacement is also simpler than imposing a force and doesn't require additional boundary conditions, for instance, contact with a rigid surface.

This approach attempts to extract the effective properties of a heterogeneous material at a smaller scale which could be extrapolated to describe the material on a larger scale. For that reason, it is considered an homogenization approach, like asymptotic expansion homogenization, which is a multi-scale approach, among others [20, 92]. The effective

[4]ABAQUS, Dassault Systemes, www.3ds.com/products-services/simulia/products/abaqus

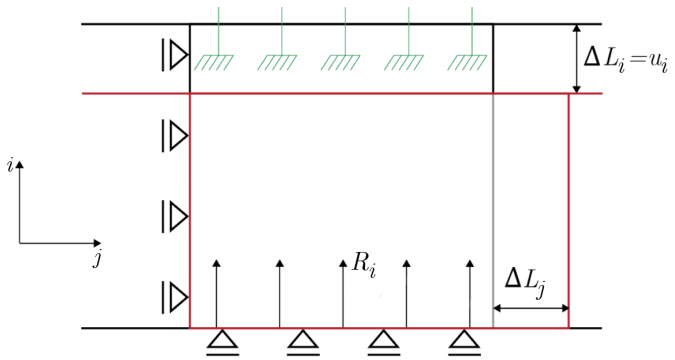

Figure 5.2: 2D representation of the SID boundary conditions [20].

properties of the foam specimens can then be determined by applying Hooke's Law [93]. The effective Young's Modulus, E, is given by

$$E = \frac{\sigma}{\epsilon} \ , \ \sigma = \frac{F_i}{A} \ , \ \epsilon = \frac{\Delta L_i}{L_i}, \tag{5.1}$$

where σ is the stress and ϵ is the strain. The stress is the ratio between the force, F_i, and the area of the section of the specimen, A. The strain is given by the ratio of the displacement, ΔL_i, by the total length of the specimen, L_i, in the load direction. Rewriting and joining these equations, the Young's Modulus can be calculated with

$$E = \frac{F L_i}{\Delta L_i A}. \tag{5.2}$$

Contrary to the most common procedure or the SPF, in which a force is applied and the displacement is determined, here a displacement, u_i, is imposed and a reaction force, R_i, must be determined. Considering these changes, the Young's Modulus takes on the following form analogous to Equation 5.2:

$$E = \frac{-R_i L_i}{u_i A}. \tag{5.3}$$

The Poisson's Ratio is defined as

$$\nu_{ij} = -\frac{\Delta L_j}{\Delta L_i}, \tag{5.4}$$

where L_j is the displacement in a generic perpendicular direction to the loading direction. The intention is to analyse each specimen in all three dimensions, but with the considered boundary conditions the cylindrical open-cell foam specimen is unusable. Adjustments would be necessary in order to extract the necessary values, therefore, it is left out.

The base material selected for the numerical analysis was AlSi7Mg, which is the material that constitutes both the cubic open-cell and closed-cell foam. Its Young's modulus is 74 GPa, the Poisson's Ratio is 0.33 and the density is 2670 kg/m^3. During the analyses only the linear elastic behaviour was considered.

5.4 Mesh Refinement

To study the mesh density is an essential step in the process of analysing the available foam specimens. It allows to understand how the geometries behave with varying numbers of degrees of freedom and for what level of refinement the results become stable. By defining a fine mesh, which corresponds to small element sizes, the results become more accurate, but the processing power requirements are higher. On the contrary, a coarse mesh, i.e., larger element sizes, produces less accurate results but with lower computational requirements. Therefore, due to the limited processing power and time, a level of refinement which is satisfactory must be selected. However, this selection might eliminate some finer details which unavoidably alter the final solution. Another option would be to apply local refinement in more detailed areas, but the mesh is strictly connected to the initial boundary mesh in STL not allowing such operations. Therefore, in order to find an equilibrium between the loss of information in the geometry and the amount of needed processing power and time, several convergence analyses of the Young's Modulus are presented for both the closed-cell and cubic open-cell foam specimens. The error of convergence is calculated with respect to the values of the previous refinement level.

5.4.1 Cubic Open-cell Mesh Convergence Analysis

In the case of the cubic open-cell foam ($22\times22\times25$ mm^3), the complete specimen was used and the conditions were defined as described in Section 5.3 with an imposed displacement of 1 mm. Then, a value for the reaction force was extracted for each refinement level, meshes in the range of $10000 - 1700000$ nodes, and the Young's moduli were calculated using Equation 5.3.

Figure 5.3 shows the evolution of the error of the Young's modulus with respect to the increase in the number of nodes. It is possible to verify that for 750000 nodes, or 2250000 degrees of freedom (DOFs), which corresponds to around 2.10E+10 Pascal, the development of the Young's modulus is minor and that there isn't much benefit in using higher refinement levels. The small fluctuations observed in Figure 5.3 can be a result of the process of meshing which, in this case, is completely connected to the STL file that was used, i.e., the process is manual and can induce small changes in the geometries (Sec. 5.2). Consequently, a satisfactory level of refinement of around 750 000 nodes has been found and is further used to analyse the specimen in Section 5.5.

5.4.2 Closed-cell Mesh Convergence Analysis

As discussed in Section 3.1.1, the closed-cell foam specimen ($14.000\times14.500\times15.571$ mm) is not ideal, i.e., it was cut before the μCT scan, which caused some larger internal and artificial cracks, and its volume/mass was approximated. For this reason and the large size of the foam file, the specimen was divided parallel to the three main plains, i.e., divided in octants[5], creating eight smaller parts of $8\times8\times8$ mm with $3 - 6$ pores in each main direction with small overlapping areas, given the original specimen is a cube with sides of 13 mm. Even though small amounts of pores can lead to unwanted effects or irregular behaviour and show different results when compared to larger amounts of

[5]Octant numbering takes the axes in consideration.

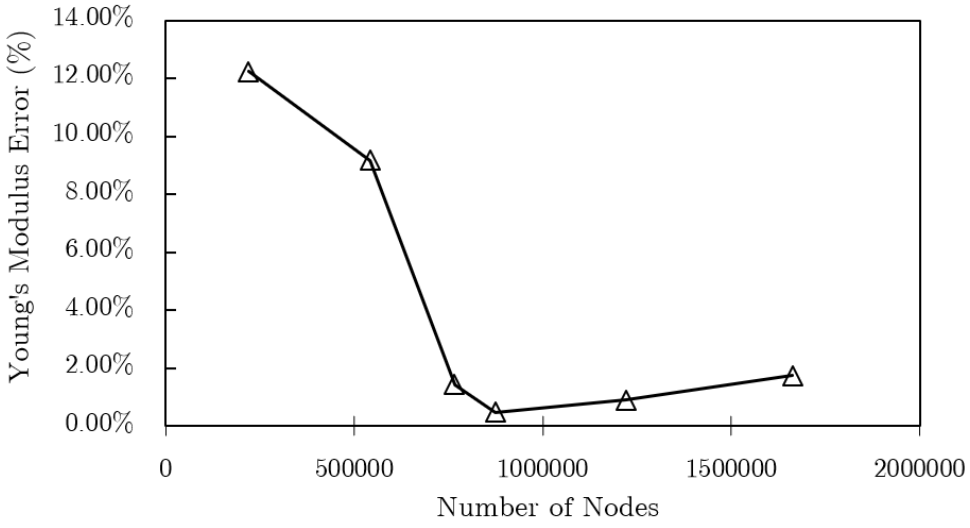

Figure 5.3: Convergence analysis of the error of the Young's modulus for the cubic open-cell foam.

pores, this separation allows for the observation of the consequences of the presence of the larger cracks [68].

As discussed in Section 4.4, there are two options for the process of simplification of the specimen: Procedure 1, i.e., plain simplification, which repairs gaps and errors and simplifies the geometry; and Procedure 2, i.e., elimination of cell wall defects and small structural imperfections, which extends the previous.

5.4.2.1 Procedure 1

Similarly to the open-cell foam, a 1 mm displacement was imposed, a reaction force was obtained and the Young's modulus calculated for each refinement level for the geometries obtained with the first procedure (Sec. 4.4.1). Each level, ranging from approximately 130000 to 1700000 nodes, was created by simplifying the original file percentage-wise (Sec. 4.4) so that all eight parts are processed equally. Therefore, each octant was simplified to 0.7%, 2%, 5%, 7%, 10% and 15% of its original number of surface faces, because the simplification is performed in *Meshlab* [50].

Figure 5.4 represents the evolution of the error of the Young's modulus. Large discrepancies between the Young's modulus of different octants are observed. Fluctuations are especially high, for example, for the fourth octant. Nevertheless, the error between each level decreases for increasing numbers of nodes, in spite of being irregular, and from the third level of refinement (from left to right), i.e., 5% of the original number of surface faces, there are no large changes. For that reason, that is the level of refinement which is used to study the close-cell foam specimen with Procedure 1.

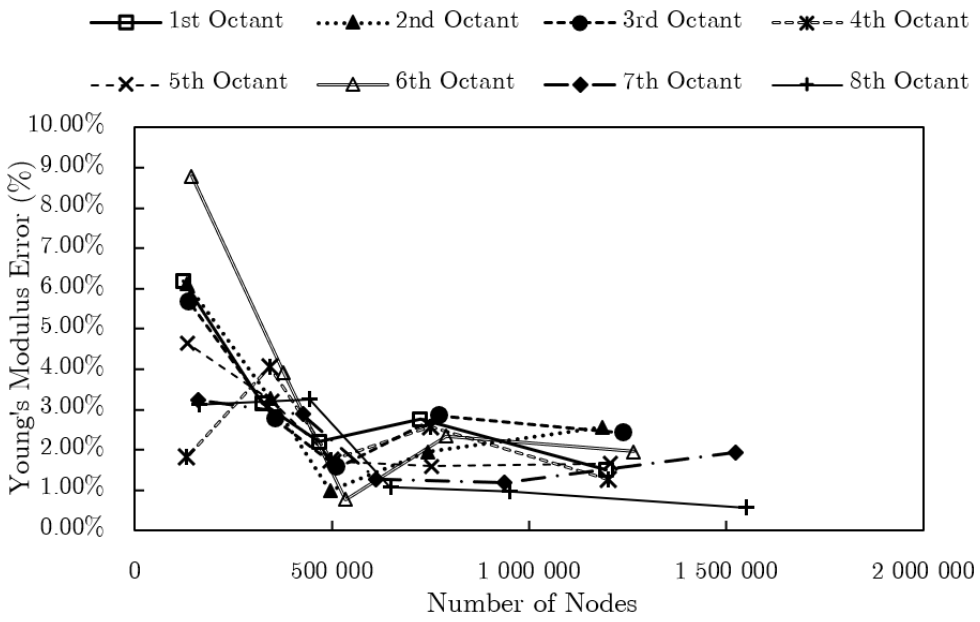

Figure 5.4: Convergence analysis of the error of the Young's modulus for the closed-cell foam prepared with Procedure 1.

5.4.2.2 Procedure 2

For the second procedure, the same conditions were used. Each octant, which has had almost all cracks in the cell walls removed, was simplified percentage-wise and compared to its less processed counterpart (Fig. 5.5). However, only three octants were analysed due to the limited time frame and because they provide enough information. The same irregular behaviour is observed for each part with no defects/kinks but with a clear decrease in error. Furthermore, from the third refinement level, 5%, there seems to be no great benefit in increasing the number of nodes. When comparing the analysis of the same octant with both procedures, the Young's modulus shows a different convergence behaviour and, therefore, appears to be dependent on the process of simplification. However, the third octant did not show a different behaviour for the two methods, as their points in the graph are coincident, and their Young's moduli are roughly the same. This phenomenon is unpredictable and can only be explained by the process of elimination of the defects in the cell walls not being successful or this section not having many or not so relevant structural imperfections. In conclusion, the 5% refinement level seems to be, again, a good trade-off between time/computational resources and quality of the analysis.

5.5 Mechanical Behaviour and Effective Properties

In this section, the effective properties for both types of foams are presented in contrast to several analytical models and experimental results. Additionally, the mechanical behaviour is analysed. All tests were performed by applying the Symmetry boundary conditions with an Imposed Displacement (SID) principles, and the calculated refinement

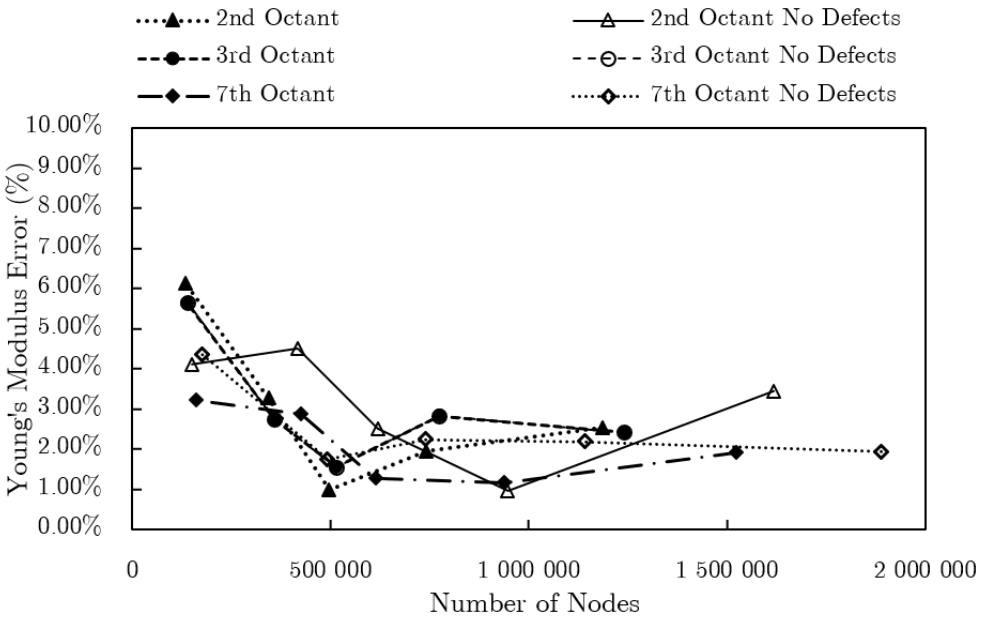

Figure 5.5: Convergence analysis of the error of the Young's modulus for the closed-cell foam prepared with Procedure 2 (No defects) compared with Procedure 1.

levels. The results are based on the determination of the Young's modulus and Poisson's ratio for each foam, but mainly using the effective relative Young's modulus, i.e., the foam's Young's modulus divided by the material's Young's modulus. As expected from such a complex process, from the 2D slices to the FEM mesh, there are always some downfalls with respect to the accuracy of the results, despite the intention being the minimization of any errors which could have been induced by the process itself. The provided analyses already give a good insight on the properties and behaviour of metal foams, but, due to the limited number of specimens, more tests are required in future work.

5.5.1 Open-cell Foam

Contrary to the closed-cell category, in which several mechanisms were used to enhance the geometry and limit the amount of errors, kinks and defects, the cubic open-cell foam is easily processed and there isn't much variation. Figure 5.6 shows the effective relative Young's Modulus of the open-cell foam, obtained with the Procedure 1, plain simplification, described in this dissertation, with respect to the relative density and compared to the analytical models described in Section 5.1. It is possible to observe that the developed μCT based model lands very closely to the expected values determined by the analytical models but slightly above them. This could be possibly explained by the lack of small cracks and structural imperfections, which are eliminated by the process of simplification, and are known to reduce the strength of the material [68]. It is difficult to compare which model best predicts the real behaviour of the foams since there is only one specimen and it is has a quite low relative density, where all models converge. The rule of mixtures is not represented since it doesn't provide useful information, the

corresponding line has a very high slope.

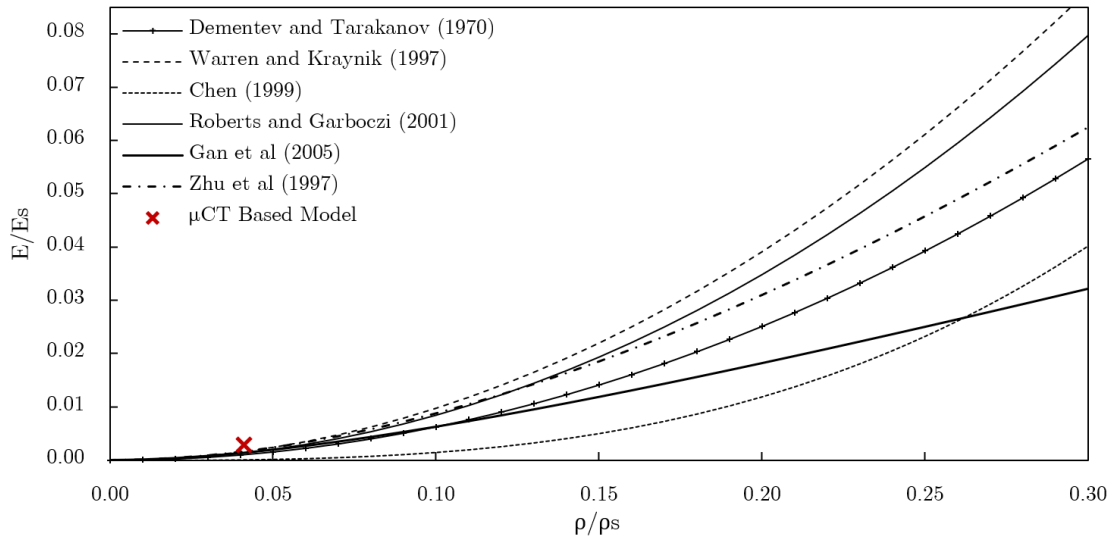

Figure 5.6: Relative Young's modulus for the cubic open-cell foam for an imposed displacement with symmetry boundary conditions.

In addition, the equivalent Von Mises stress distribution along the foam can be analysed in Figure 5.7. It can be noted that there are several zones where the base material's yield stress (Aluminium alloy $\approx 10^6$ Pa) is surpassed. This happens because a random "round" displacement (1 mm) was imposed. Since the analysis is elastic, there is no interference in the calculation of the Young's modulus and the stress distribution can still be analysed. The blue colour represents parts of the foam specimen where very low stresses can be found. This phenomenon originates from the definition of the boundary conditions, in which those parts are free to move, since the symmetry boundary conditions are placed on the opposite side of the model[6]. In addition, stresses along the foam are consistent, with greater values on the struts. Some areas have a more homogeneous behaviour while others give an idea of flexion.

5.5.2 Closed-cell Foam

The process of obtaining the simplified closed-cell foam is quite complex, has many parameters which could be altered and, consequently, change the final solution. However, due to limited time and resources, only the most important parameters are discussed, such as the influence of the morphological operations and the difference between maintaining (Procedure 1) or eliminating (Procedure 2) the defects and structural imperfections in the cell walls.

5.5.2.1 Octants

In Section 3.1.1, the presence of some artificial large cracks was identified, leading, understandably, to the question whether the specimen was viable or not and how large

[6]This phenomenon shows the importance of periodic boundary conditions.

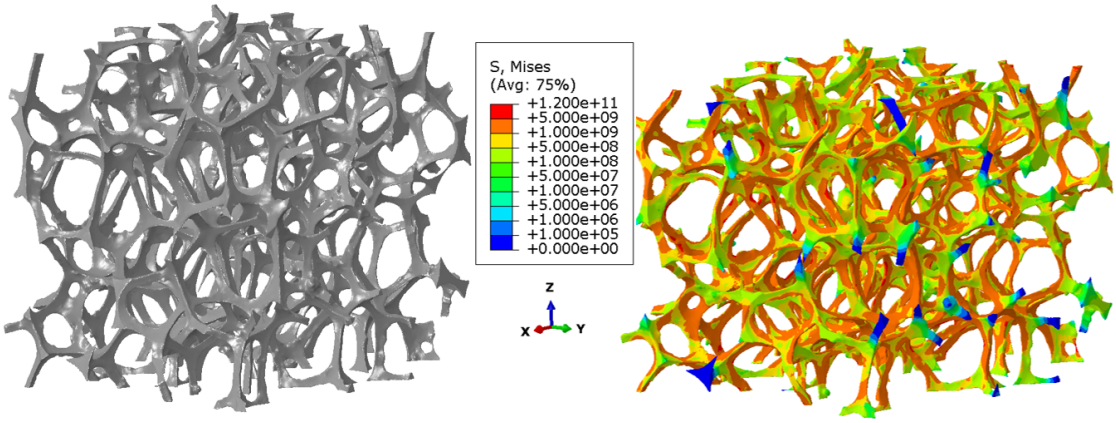

Figure 5.7: Stress distribution (Equivalent Von Mises) for the cubic open-cell foam for a compression analysis.

an influence this problem would have on the final global solution. For this reason, the foam was divided in octants and the levels of refinement were evaluated percentage-wise. Now, the effective relative Young's modulus is evaluated for each of the defined octants using the foam simplified with Procedure 1, which keeps the defects and is, therefore, closer to reality.

Figure 5.8 shows results obtained for each individual octant compared to several analytical models and the whole foam. It is possible to observe that the sixth octant is not only the section whose behaviour most diverges from what is to be expected as well as the section which encapsulates the great majority of the large supposed artificial cracks. The rest of the parts vary a fair amount with octants one, two, three, four and five landing on the same area lower on the graph and seven and eight showing a stiffer behaviour and higher relative densities. The whole foam presents results very close to the analytical ones leaning towards the area of the less stiff octants, as is to be expected. Additionally, due to the high number of small features and cracks on the cell walls, the number of points with stress concentrations is significantly higher than if the small defects would have been removed, as in Procedure 2. This causes the simulation to be a little more unstable, despite the finer details. In general, this is a positive result as it shows that this method has the potential and could possibly be useful for future research, despite still needing more confirmation.

In addition, Figure 5.10 shows the stress distribution in the whole foam (equivalent Von Mises stress). The yield stress is again passed because of the imposed displacement (1 mm). The load appears to be mainly transmitted by the face walls and somewhat also by the struts. As mentioned before, the areas with small structural imperfections show a higher concentration of stresses.

5.5.2.2 Influence of the Elimination of Defects

The presence of small defects, cracks and kinks in foams is well documented in the literature [41, 68]. Their existence is known to significantly reduce the strength of foams and to be critical to their failure. However, the comparison of a model of the same foam with and without such defects is something innovative given that without the μCT

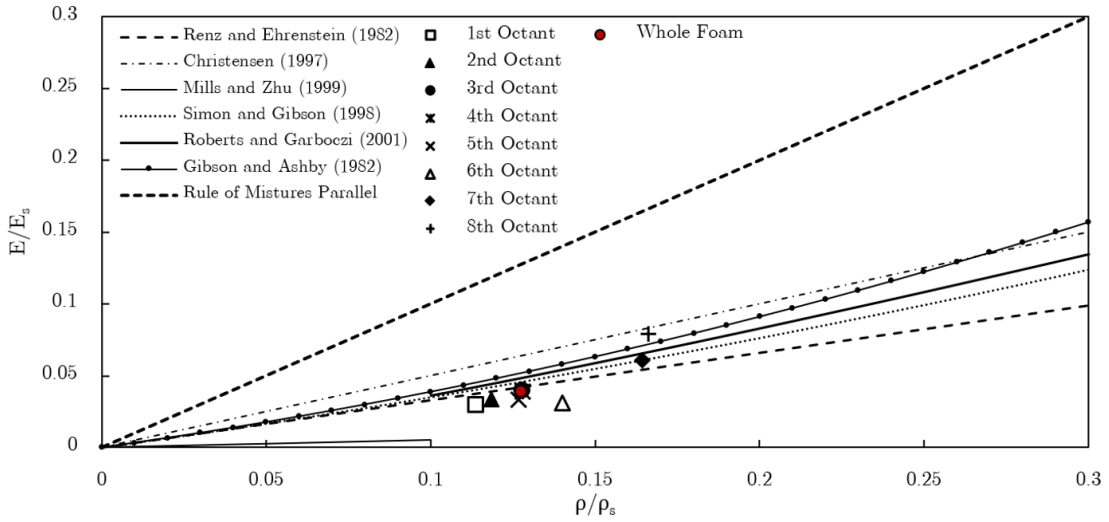

Figure 5.8: Relative Young's modulus for the closed-cell foam and the different octants.

images it is impossible to recreate the exact same foam with such slight differences. Therefore, this analysis allows to understand how critical these small changes are.

The foam specimen was prepared with Procedure 1, i.e., normal foam with defects, and Procedure 2, i.e., the defects were removed, and the results are displayed in Figure 5.9. It can be noted that Procedure 2 yielded a value of Young's modulus significantly larger than Procedure 1, getting close to the limit imposed by the rule of mixtures (parallel). An increase was expected, given there would be more material and less kinks, but the magnitude of the difference is quite surprising. Furthermore, the difference in mass between both procedures is minimal, i.e., the two points are vertically aligned in the graph, with a difference of just 0.1% the original weight. From this information, it can be assumed that the small defects have a severe impact on the strength of the material the same way a hole has a great impact on a sheet of metal. In addition, Procedure 2 makes the mesh smoother (with less irregularities) which could lead to a better response to the applied load. The same effect can be observed for the smaller octants. In this case, two of the three tested octants show a great increase in the Young's modulus, while one remains somewhat the same. This phenomenon might indicate that this part of the foam doesn't have as many cracks or that their position is not as critical as in the others.

The foam versions with no defects had few or no points with stress concentrations while their "defected" counterparts presented some kinks in those regions. Therefore, the first are more stable even though they usually overshoot the estimations of Young's modulus. Moreover, the same foam simplified with the two procedures presents a distinct stress distribution, which provides some insight on the effect of the structural imperfections (Fig. 5.10). The distribution appears to change significantly, demonstrating their great impact.

5.5.2.3 Influence of the Closing Morphological Operation

In Section 3.2.3.1, the morphological operation named closing was introduced. Its purpose was to clean up any remaining speckles from the μCT scan, smooth the surfaces

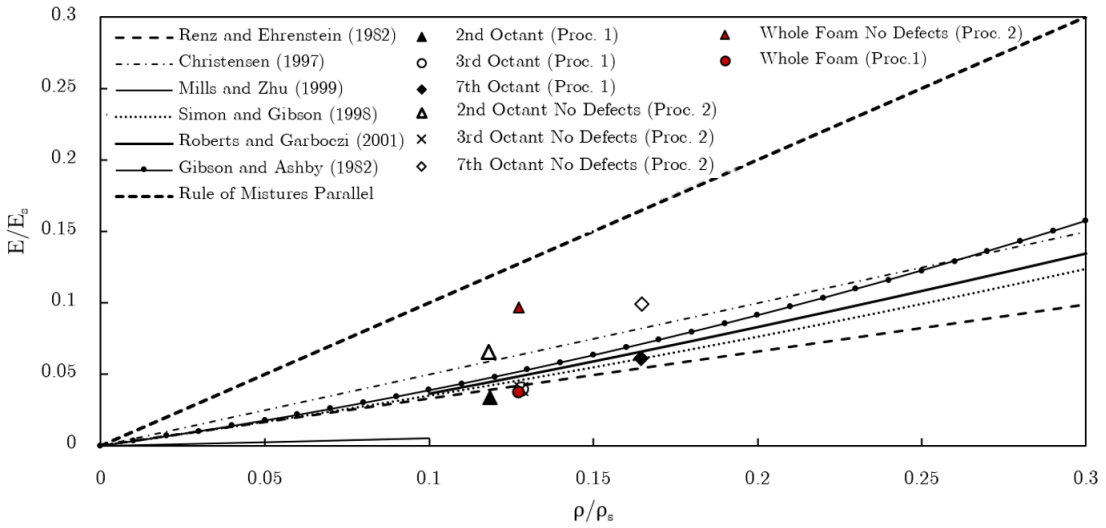

Figure 5.9: Relative Young's modulus for closed-cell foam prepared with Procedure 1 (defects) and Procedure 2 (no defects).

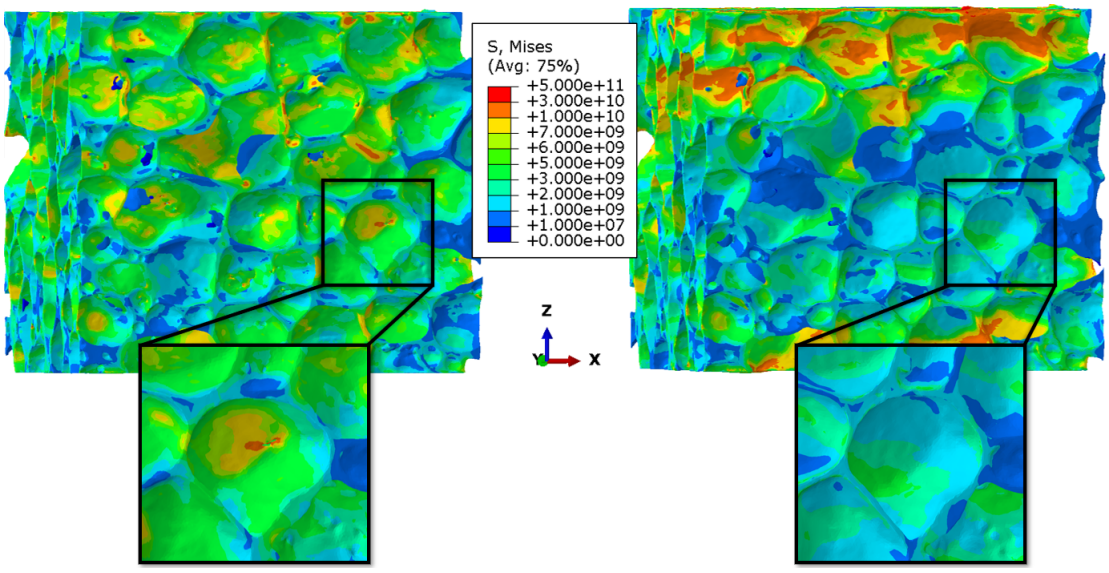

Figure 5.10: Stress distribution (Equivalent Von Mises) for the closed-cell foam for a compression analysis. Procedure 1 (plain simplification) on the left and Procedure 2 (no defects) on the right.

and close very small pores and kinks, delivering, in the end, a better, more stable STL file which would then be easier to simplify. However, this process caused a gain of mass which was balanced with a readjustment of the threshold in *CTAn*.

Now, after discussing the process and maintaining all other variables constant, the impact of the radius of the closing operation on the Young's modulus is evaluated (Fig. 5.11). Due to the amount of time necessary to process the whole foam, only three radii were tested, 0 mm or no closing operation, 0.06 mm and 0.12 mm. It can be observed that, for smaller radii, the impact on the Young's modulus is small and can, therefore, be beneficial. On the contrary, for higher radii the modulus is seriously altered. This is possibly caused by some defects in the cell walls being fixed, reinforcing the structure as it was discussed in Section 3.2.3.1. It is difficult to judge whether this might be a good application for this operation as it increases the values which are being examined, but, at the same time, facilitates the process and makes it more stable during simulation, i.e., less kinks and small features. It should be noted that the values discussed here are purely used as an example and for this specific type of foam. Due to principles of morphological operations, foams with different pore sizes and porosities will certainly require different radii in order to observe the same results.

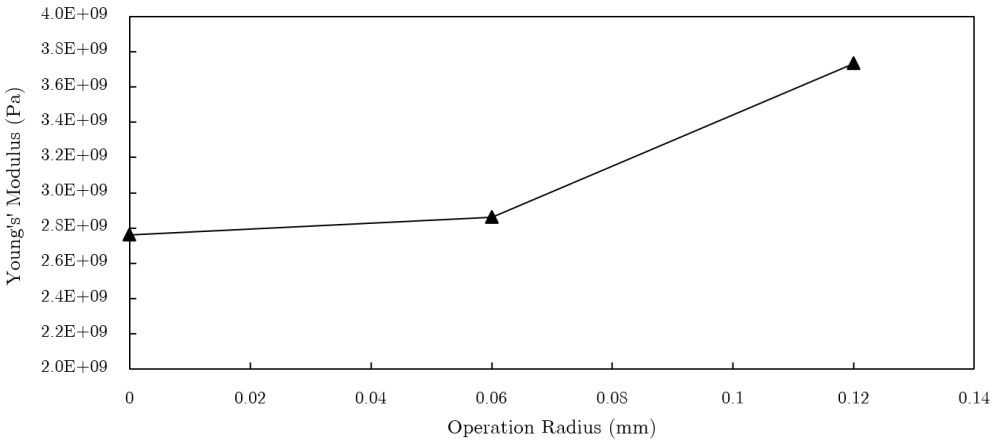

Figure 5.11: Analysis of the Young's Modulus with respect to the radius of the closing operation.

5.5.3 Experimental Results

In order to evaluate this method, a full analysis from start to finish would be ideal, i.e., obtaining the specimen, scanning it, obtaining its mass, performing the procedures described throughout this document and performing a compression strength test on the same specimen. However, the results for the foams weren't available and they had already been destroyed. For this reason, the second best option is to compare with other available foams.

The results obtained with the described procedures are now compared to the experimental results obtained by other authors and the numerical and theoretical models in Tables 5.1 and 5.2. Duarte et al. [68] provides values of foams obtained by powder metallurgy, with two types of specimens: one large foam block (FB) and four integral-skin cubes (IC). Jang et al. [94] and Triawan et al. [95] provide results for specimens obtained

with batch casting, which yield foams called ALPORAS. In (Fig. 5.12), the models of the whole foams obtained with the procedures based on μCT scans are shown in comparison to the analytical models and experimental results. Among each other, the ALPORAS show a stiffer behaviour when compared to the foams analysed by Duarte et al., which highlights the impact of the different processes on the final results [68]. In general, both the analytical models as well as the approach described here appear to overestimate Young's modulus, which can derive from the lack of defects. Nevertheless, Procedure 1 comes close to what was demonstrated by the real foams emphasizing the importance of considering the small defects in the cell's walls. Procedure 2, despite being more stable, overshoots the expected values provided by the experimental results and the models.

For the cubic open-cell foam, values were taken from the work of Ashby et al. [26]. In this case, the theoretical and numerical models are able to accurately predict the relative Young's modulus of the real foam specimens, however, the developed model overestimates both. The specimen shows a stiffer behaviour, which could result from the simplification and elimination of small structural imperfections. Unfortunately, there isn't any specimen for the same relative density, therefore, it is difficult to reach a conclusion. More specimens and tests are required.

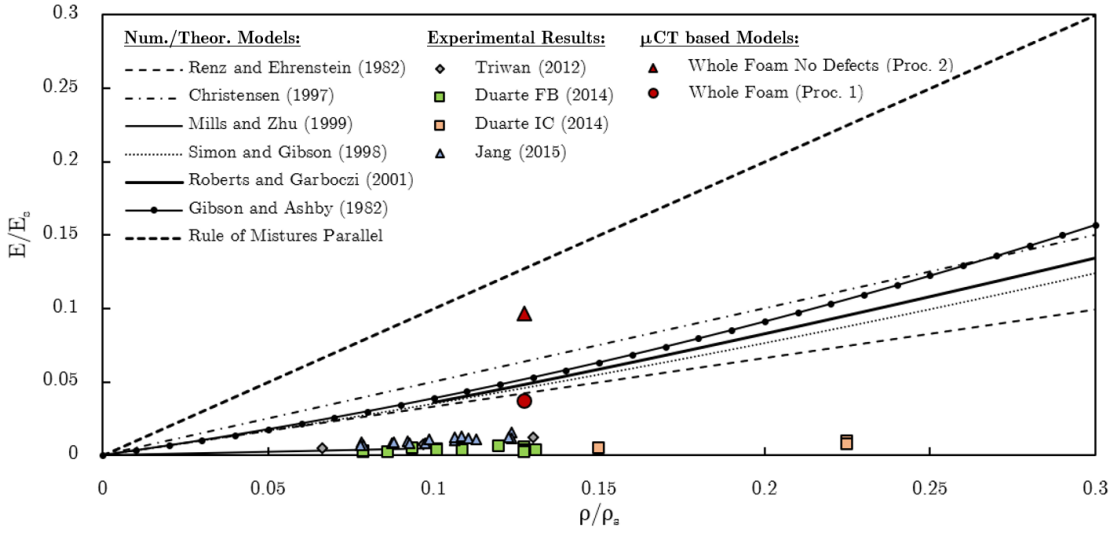

Figure 5.12: Relative Young's modulus of closed-cell foam models and experimental results [68, 94, 95].

5.5.4 Representative Unit-cell Models

An alternative to the proposed procedures based on μCT scans is using Representative Unit-Cell (RUC) models which try to recreate the different foams with a simplified structure which can be periodically repeated to construct foams of different sizes. For this reason, they are far less detailed, but simpler and require less processing power, a feature that is highly desirable in case the results are accurate. Due to being simpler also means there are no kinks and defects which can alter the results as seen with Procedure 1 and 2.

These alternatives have already been tested by Aquino, a colleague from the same

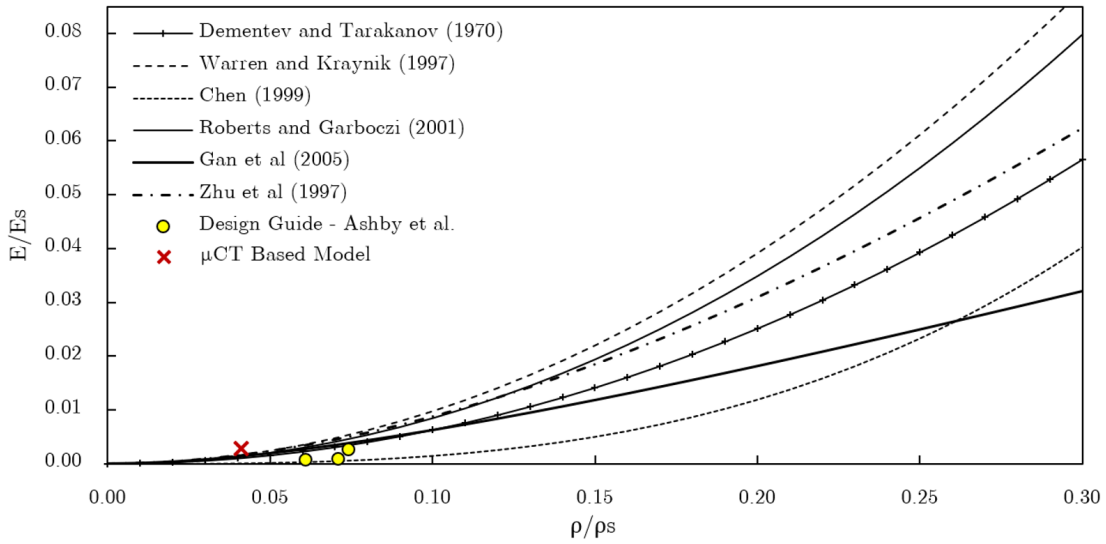

Figure 5.13: Relative Young's modulus of open-cell foam models and experimental results [26].

institute [19, 20]. Eight different types of RUCs were considered[7]: Four for the closed cell-foams, Solid Closed Kelvin Cells (CL), Surface Kelvin cells, Solid Closed Weaire-Phelan (CL) cells and Surface Weaire-Phelan cells, and four for the open-cell foams, Solid Open Kelvin cells (OP), Wire Kelvin cells, Solid Open Weaire-Phelan (OP) cells and Wire Weaire-Phelan cells [96].

Analysing Figure 5.14, one can observe that for the closed-cell foams, the predictions of the RUCs are very similar to the predictions given by the theoretical and numerical models. Consequently, they overestimate the relative stiffness of the evaluated specimen processed with Procedure 1 (with defects) and are below the results for Procedure 2 (no defects). As it can be seen in Figure 5.12, the real foams present values of Young's modulus which are lower than what is indicated by the several models and, for this reason, also lower than the ones provided by the RUCs. Then, it is possible to conclude that the first procedure elaborated and described here shows better results. Yet, the processing power required is much greater and the difficulty is higher, which can make the representative unit-cells one of the preferred options when it comes to mimicking and simulating closed-cell foams. Nevertheless, using μCT imaging can most likely yield more accurate results for individual foams if the user is very attentive to the changes caused by the process of obtaining the 3D models from the 2D slices in the cell structure.

The same tendency is observed for the open-cell foams (Fig. 5.15), but with greater accuracy. The representative unit-cell models perform very well when compared to the theoretical and numerical models as well as the experimental results discussed in Figure 5.13. Again, the μCT model created here shows a value of relative Young's modulus just slightly above the predicted ones, consequently, demonstrating that it might be unnecessary to use such complex techniques. Even though this type of foam is simpler when compared to the closed-cell foam μCT based model, it still is more complex and time consuming than simply using the RUCs. For this reason, the best solution might be

[7]More information about the cell types in Section A.5.

using a RUC based model when such applications are necessary. In the end, it seems that using the μCT for such purposes isn't useful unless a more in-depth analysis is required. In addition, the presence of defects in the cell walls appears to be the determining factor when it comes to the accuracy of such models. The open-cell foams have very few defects and kinks and their behaviour is well predicted by most models. In contrast, the closed-cell foams have many kinks and cracks, the processing procedure heavily influences the final results, and the models have a hard time correctly predicting their properties.

In conclusion, these models are able to approximately predict the effective properties of the open-cell and closed-cell foams. Even though they are faster and easier to apply, the amount of detail is reduced and the local behaviour can't be analysed. Additional tests should be performed in order to complement the performed tests, also taking into consideration the nonlinear behaviour of the materials.

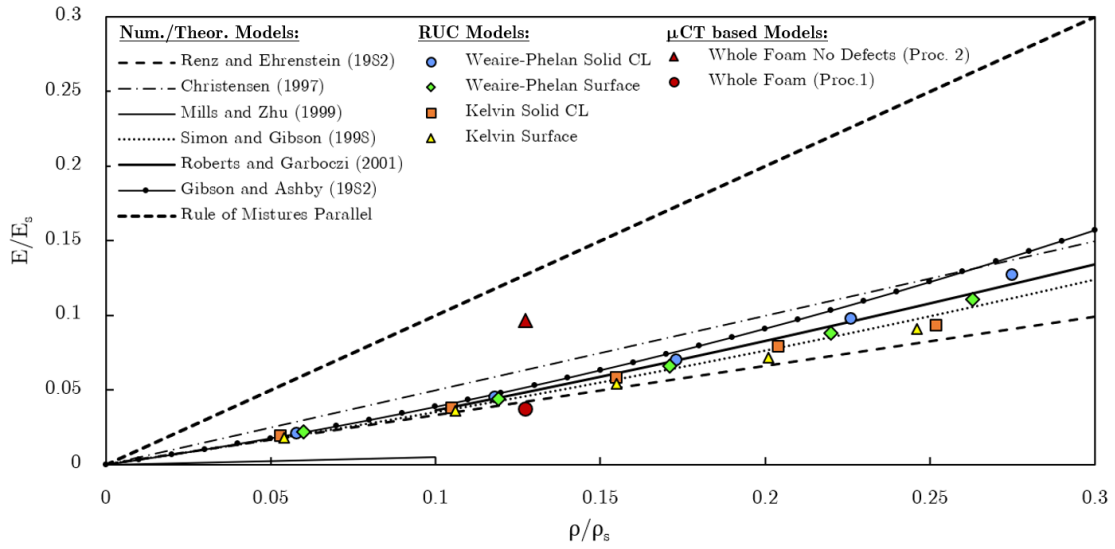

Figure 5.14: Relative Young's modulus of closed-cell foam μCT based models and RUC models [19, 96].

5.5.5 Anisotropy Analysis

The two types of cells were also studied in the other two main directions allowing for an anisotropy analysis. The results are presented in Table 5.3 as

$$\begin{bmatrix} E_{\mathrm{x}} & \nu_{\mathrm{xy}} & \nu_{\mathrm{xz}} \\ \nu_{\mathrm{yx}} & E_{\mathrm{y}} & \nu_{\mathrm{yz}} \\ \nu_{\mathrm{zx}} & \nu_{\mathrm{zy}} & E_{\mathrm{z}} \end{bmatrix}, \tag{5.5}$$

where ν_{ij} is calculated using Equation 5.4. Results show that there is a high orientation dependence for all specimens. The closed-cell foam specimen simplified with Procedure 1 demonstrates a stiffer behaviour in the y direction and a high variability in Poisson's ratios, which range from 0.25 to 0.29. Interestingly, the elimination of the small structural imperfections with Procedure 2 significantly increases the Young's modulus in all directions and makes the specimen stiffer in the x direction, displaying, again, the strong

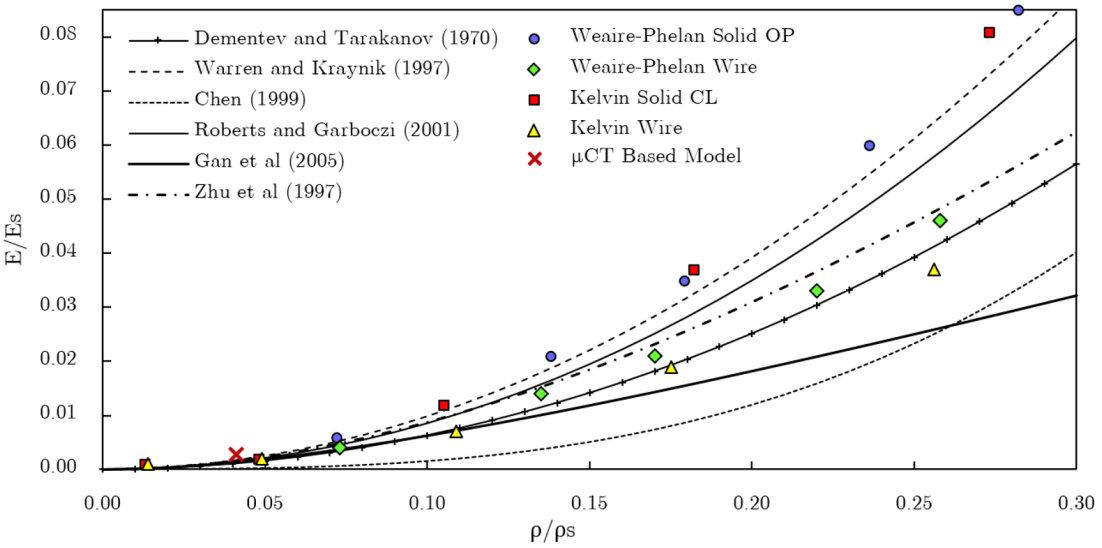

Figure 5.15: Relative Young's modulus of open-cell foam μCT based models and RUC models [19, 96].

influence of the small defects. There is also a noticeable change in the Poisson's ratios, which range from 0.20 to 0.25. The cubic open-cell foam exhibits the largest difference, in proportion, between its Young's moduli. In the case of the Poisson's ratios, ν_{zx} and ν_{zy} are 0.56 and 0.58, which are unexpected values for open-cell foams, given a perfect open-cell foam has approximately a value of 0.33. A Poisson's ratio above 0.5 indicates that the material is highly anisotropic. In order to confirm the validity of the process of numerical modelling, a solid cube was tested which yielded the exact same properties as the base material. Since the modelling appears to work correctly, the high values can be attributed to two factors: 1) the foam specimen is indeed highly anisotropic; 2) or/and there is the induction of local deformations by deformation mechanisms. The strain (deformation) was calculated with the average displacement of the nodes on the free sides of the specimens, which could have had their values emphasised by a rotation of the struts.

Table 5.3: Values of Young's modulus (Pa) and Poisson's ratio in all three directions for the closed-cell foam specimen with both procedures and for the cubic open-cell foam specimen.

Closed-Cell Procedure 1	**Closed-Cell Procedure 2**	**Cubic Open-cell**
$\begin{bmatrix} 2.92 \cdot 10^9 & 0.27 & 0.25 \\ 0.28 & 3.12 \cdot 10^9 & 0.29 \\ 0.25 & 0.26 & 2.76 \cdot 10^9 \end{bmatrix}$	$\begin{bmatrix} 7.61 \cdot 10^9 & 0.22 & 0.21 \\ 0.22 & 6.82 \cdot 10^9 & 0.25 \\ 0.20 & 0.23 & 7.15 \cdot 10^9 \end{bmatrix}$	$\begin{bmatrix} 1.38 \cdot 10^8 & 0.31 & 0.29 \\ 0.32 & 1.35 \cdot 10^8 & 0.31 \\ 0.56 & 0.58 & 2.09 \cdot 10^8 \end{bmatrix}$

Both specimens can be approximated as orthotropic materials, there is a high orientation dependence, with a compliance matrix, i.e., the inverse of a stiffness matrix,

given by [97]

$$\begin{bmatrix} \frac{1}{E_x} & -\frac{\nu_{yx}}{E_y} & -\frac{\nu_{zx}}{E_z} & 0 & 0 & 0 \\ -\frac{\nu_{xy}}{E_x} & \frac{1}{E_y} & -\frac{\nu_{zy}}{E_z} & 0 & 0 & 0 \\ -\frac{\nu_{xz}}{E_x} & -\frac{\nu_{yz}}{E_y} & \frac{1}{E_z} & 0 & 0 & 0 \\ 0 & 0 & 0 & \frac{1}{G_{yz}} & 0 & 0 \\ 0 & 0 & 0 & 0 & \frac{1}{G_{zx}} & 0 \\ 0 & 0 & 0 & 0 & 0 & \frac{1}{G_{xy}} \end{bmatrix}, \tag{5.6}$$

where

$$G_{ij} = \frac{E_i}{\nu_{ij}}. \tag{5.7}$$

Orthotropy is a subset of anisotropy, in which a material's properties differ along three mutually-orthogonal axes, i.e., the material possesses symmetry about three orthogonal planes, and can be defined by six different parameters instead of thirty six, as seen in Equation 5.6. The open-cell foam specimen could be further simplified. Its behaviour resembles a transversely isotropic material, in which the properties are the same for all directions in a plane, such as the x-y plane, but different for the third (z) direction. Nevertheless, it is approximated as an orthotropic material. The condition of anisotropy is confirmed, because of the symmetry of the stiffness matrix, by the relation [97]

$$\frac{\nu_{ij}}{E_i} = \frac{\nu_{ji}}{E_j}, \tag{5.8}$$

where $i \neq j$. With the information provided in Table 5.3 and Equation 5.6, the anisotropy maps can be constructed. Figure represents the 3D anisotropy maps for the closed-cell foam specimen with Procedure 1, the closed-cell foam specimen with Procedure 2 and the cubic open-cell foam specimen. The oblong shapes of the maps demonstrate the orientation dependence of the materials, therefore, the anisotropy.

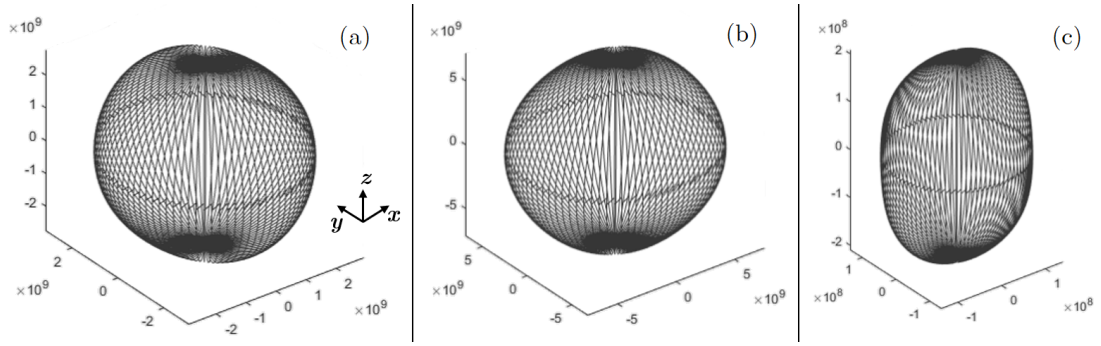

Figure 5.16: 3D Anisotropy maps for (a) the closed-cell foam specimen with Procedure 1, (b) the closed-cell foam specimen with Procedure 2 and (c) the cubic open-cell foam specimen.

Intentionally blank page.

Chapter 6

Final Remarks

Metal foams have a particular set of properties, for example, high strength-to-weight ratio, good impact absorption, great vibration damping and high thermal and electrical conductivies, which make them very desirable for certain applications. However, their final properties depend greatly on several factors (Sec. 2.1), such as the properties of the base material (aluminium), the cellular structure (e.g., pore size distribution) and the relative density, all of which are considerably affected by the production method and conditions. Due to the stochastic nature, i.e., the random development of cellular pores, of the open-cell and closed-cell foams, they exhibit several complex morphological imperfections, for instance, structural defects and imperfections. Such structural defects and imperfections limit the ability to produce foams with consistent properties, which could be later used in high performance structures and products. Therefore, the objective of this work was to develop a procedure which allows to predict the properties using the real cellular structures of these stochastic aluminium foams obtained from μCT scans and use them for the development of FEM models. The models could then be used to characterize the foam specimens not only in different scenarios of mechanical loading but also thermal and electrical conditions. They are a tool to supplement the experimental mechanical characterization of cellular metals and can be used before experimental testing to reduce the number of required specimens and after to validate other computer models. In this case, the properties of the aluminium alloy foams are evaluated with regards to the relation between the Young's modulus and the relative density.

The development of the procedure to obtain the FEM models was divided in three stages: (1) 2D slice acquisition and analysis; (2) 3D geometry simplification and analysis; (3) numerical modelling and analysis. In the first stage, the 2D reconstructed slices were processed in order to provide geometrically correct, binary 2D slices with a minimum number of speckles/artifacts (Sec. 3). Thus, several thresholding techniques were applied in an effort to segment the images (2D slices). Otsu thresholding was employed to the 2D slices of the different specimens, providing results based on the statistical analysis of the information in the slices without human intervention. Results are very positive and show a good separation between the foreground and background for both open-/closed-cell foams [47, 48], but are very dependent on the quality of the images/scans, which could influence the final outcome. Then, three different Adaptive Thresholding (AT) techniques were applied to the foam specimens: Mean-C, Median-C and Mean of Minimum and Maximum Values [16]. AT techniques make decisions based on local information, taking local variations of the intensity of grey in consideration. However, results indi-

cated that many artificial voids in the cell walls and struts appeared, which impacted the final shape and changed the mass/volume of the specimen substantially. These changes are detrimental to structural analysis and go against the procedure's philosophy, i.e, the minimization of change to the structure. Furthermore, the definition of the involved parameters is very intricate, as demonstrated by other authors [16]. Afterwards, the global threshold was manually selected in an attempt to include physical properties of the foam specimens in the segmentation process. As a result, the mass/volume of the foam was taken as a quality indicator, merging the properties of the 2D slices with the physical properties of the foam. This process achieved very good separation between the foreground and the background and the masses/volumes of the foams were matched with differences of 0.141%, 0.138% and 0.108% of the original values for the cubic open-cell, cylindrical open-cell and closed-cell foam specimens, respectively. In contrast, the Otsu thresholding technique yielded a threshold of 70 for the closed-cell specimen (comparing to 47 for manual selection), which results in a volume/mass variation of 15.408%. Hence, the manual selection of the threshold based on the quality indicator was preferred to the Otsu technique. The threshold of the two open-cells were very different, despite being produced in the same way, which shows that the μCT scan parameters have an influence on the final threshold. The densities of the two specimens were different, so no final conclusions could be reached. It was also observed that the application of the closing morphological operation brings benefits in terms of surface quality and elimination of small defects and pores, which makes the adjustment of threshold necessary because of the addition of mass. The elimination of small speckles and artifacts in the 2D slices is very useful causing changes inferior to 0.1% of the real mass/volume.

In the second stage, 3D surface meshes, or boundary meshes, were created based on the binary 2D slices. The two different tested reconstruction algorithms yielded very different results. The Double-Time Cubes (DTC) algorithm showed better smoothing than the Marching Cubes 33 (MC33), however, only the MC33 maintained the mass of the specimen unchanged (variations lower than 0.031%). Moreover, the smoothing caused by DTC was automatic, not allowing any control over the final result. Then, the resulting 3D surface meshes were simplified using the two described procedures, which were used to evaluate the effect of the presence of defects and of the the procedure in numerical analysis. Procedure 1 maintained all small defects and cracks in the cell walls and Procedure 2 eliminated them using the discrete curvature of those features. In the end, the procedures managed to maintain the mass with small variations of a maximum of 2% of the initial volumes/masses for both types of foams (open-/close-cell), showing also a very small difference of 0.1% between the two procedures applied to the closed-cell foam. In addition, the variation in the shape was tested with the Hausdorff algorithm and difference between meshes. Results show that the shape of the foam specimens suffered small changes even for reductions of 99% of the number of faces, i.e., values inferior to 0.04%. The quality of the mesh, described by the closeness of the triangular faces to an equilateral triangle, was improved by the Taubin smooth algorithm, while preserving the shape and mass.

Finally, in the third stage, FEM models were created based on the 3D boundary/surface models. They were meshed for FEM using free software (Gmsh), which can directly mesh STL files. Other options, like converting the STL to a parametric model, were tested but limitations rendered them impractical. Subsequently, the mesh convergence was analysed for both foam specimens. Unfortunately, the closed-cell foam

was divided in octants, in order to evaluate some possible artificial damage to the specimen. In the case of the open-cell specimen, the developed model based on μCT showed results very close to not only the different analytical and numerical modes but also the experimental results and the results based on Representative Unit-Cells (RUC). The relative Young's modulus with respect to the relative density was well predicted even though there was no real experimental results with the same relative density. Additionally, it showed anisotropic behaviour. The closed-cell foam was tested for the two procedures (defects and no defects). The results were very positive for Procedure 1 (with defects), showing a relative Young's modulus very close to the prediction of the analytical, numerical and RUC models and experimental results, but with some kinks and concentration of stresses in smaller features. Procedure 2 (no defects) exhibited less kinks, however, the value of relative Young's modulus was almost double the one obtained with Procedure 1, deviating more from the several models. This is an important finding, since it provides insight about the presence of small cracks and defects on the cell walls. They appear to substantially weaken the foam. Moreover, the effect of the procedure to obtain the foam models on the models themselves comes into questioning. Higher standardization might be required in order to compare this sort of numerical results with experimental results and with results by other authors. Lastly, the closing operation was verified to impact the Young's modulus severely for larger radii. However, for smaller radii it provides smoother models with less kinks and lower increases to the Young's modulus.

In conclusion, this work demonstrates that μCT is an effective technique to reconstruct the complex geometrical and topological features of open-cell and closed-cell foams, which are otherwise difficult to capture, and use them, successfully, in simulation software. The obtained models allow for the observation of the local structure, behaviour and anisotropy, requiring high computational power. Therefore, high detail corresponds to slower analyses, making other simpler types of models better for other applications. It was also shown that the process from the 2D slices to the FEM model has a great impact on the results, which should be taken into consideration when developing models based on μCT scans.

6.1 Future work

Further research is required in order to complement what has been discussed. Suggestions are:

1. Evaluate the effects of the μCT scans' parameters on the resulting 2D slices;

2. Apply the 3D Watershed technique to bridge gaps in the cell walls during 2D slice processing, instead of using discrete curvature, to delete small cracks and defects [10, 14];

3. Use different types of elements for FEM [14];

4. Evaluate shell finite element modelling for closed-cell foam specimens [10];

5. Nonlinear FEM analysis;

6. Investigate other software for image (2D slice) analysis or geometry simplification, such as *Mimics*[1], *ScanIP*[2];

7. Direct comparison of experimental data and numerical results for the same specimen.

[1]Materialise NV, Leuven, Belgium
[2]Simpleware Ltd. Exeter, UK

Appendix A

Complementary Information

A.1 Foam Production Methods

When compared to other foams made of polymers or ceramics, metal foams have greater potential. Polymer foams show a more flexible behaviour, but can't support high temperatures [37]. Ceramic foams are stiff and can endure high thermal shocks, but are brittle. In contrast, metallic ones are tough, can plastically deform and absorb high amounts of energy. In spite of the advantages, they are yet to be used in large scale mainly because of the lack of fine control and difficulty of obtaining consistent results, at least for the stochastic ones. For these reasons, the production methods are an important topic of discussion and are currently being developed [1, 34, 35]. The different methods can be divided into categories according to the state of matter in the initial step of production [2]:

(i) from metal vapours;

(ii) from liquid metals (melt metallurgy);

(iii) from powdered metals (powder metallurgy);

(iv) from metal ions.

Despite the large number of different production methods based on the aforementioned concepts, only a few are commercially relevant, therefore, only the ones based on liquid and powdered metals are discussed for stochastic foams of the two different cell types (closed and open-cell). Periodic foams are produced with other methods and are not discussed here [29–31].

A.1.1 Closed-cell Foam Production

In the case of closed-cell foams, the production methods can be divided in two groups: melt metallurgy, also known as direct foaming, and powder metallurgy, indirect foaming (Fig. A.1) [98]. Melt metallurgical production methods are some of the most efficient methods used to produce closed-cell foam specimens. They can also be referred to as direct foaming methods, given the pores are created by directly introducing inert gas bubbles, for example, argon, in the molten liquid metal. However, as the laws of physics demand, the bubbles formed tend to rise to the surface and be released

due to strong buoyancy forces. This effect can be minimized by increasing the fluid viscosity by the introduction of fine ceramic powders, like silicon carbide or aluminium oxides (5-20 vol%), which provide stabilization. In a second step, the melt is foamed by injecting gases (air, nitrogen, argon) into it using rotating impellers or vibrating nozzles, which introduce very small bubbles and distribute them uniformly. The resulting viscous mixture of pores and metal melt floats to the surface of the liquid where it turns into a moderately dry liquid foam. It can then be pulled out to stabilize and solidify. The produced foam can, in theory, be as large as the vessel where it is produced. This method makes the production of large specimens possible. Other variations are also possible, such as using chemically generated bubbles by the decomposition of a blowing agent or the precipitation of gas dissolved in the melt by controlling temperature and pressure [1, 2, 26, 99].

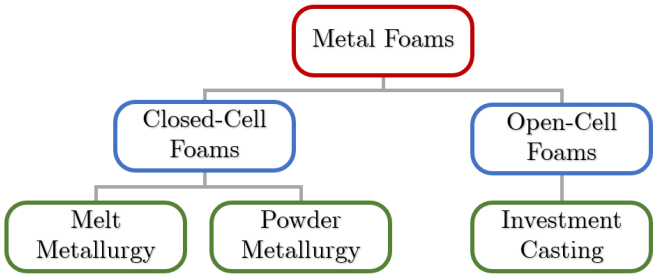

Figure A.1: Schematic of commercially relevant production methods of metal foams including trade names and companies [1].

Contrary to the previous group, powder metallurgy based production methods, or indirect foaming methods, utilize matrix metal and blowing agent powders (Fig. A.2). The process begins with the mixing of the aluminium alloy powder with the blowing agent, typically 0.5 to 1.0 wt.% of TiH_2 [1, 100]. The mixture is then consolidated and sintered by extrusion, uniaxial compaction or rolling in order to obtain a foamable precursor [1, 100, 101]. The next step consists of heating the precursor up to a temperature near the melting point of the matrix material. Then, the blowing agent starts to decompose, releasing gas that force the sample to expand, subsequently, creating its highly porous structure. Traditionally, the foams can be produced by placing the precursor inside the cavity of a mould which is filled up during the expansion process, however, this process usually requires manual intervention and is limited because of it. For those reasons, other options have been developed, such as continuous foaming furnaces, which try to automate the production and remove the human element. These use long furnaces, which are divided in three heating zones for the different stages of foaming, and conveyor belts to carry the moulds [35].

Powder metallurgy methods have several advantages when compared to other methods based on melts. They enable the production of components of complex geometry, good quality, good surface finish and there is no necessity to use expensive joining techniques like welding and brazing to join the metal foams with other materials, which damage the foams [35]. Moreover, they can be produced in-situ as a core or filler for sandwich panels and thin-walled structures, respectively. On the other hand, melt metallurgy is able to produce very large parts. However, they are more brittle, due to the introduction of a high quantity of ceramic particles, and their application, for exam-

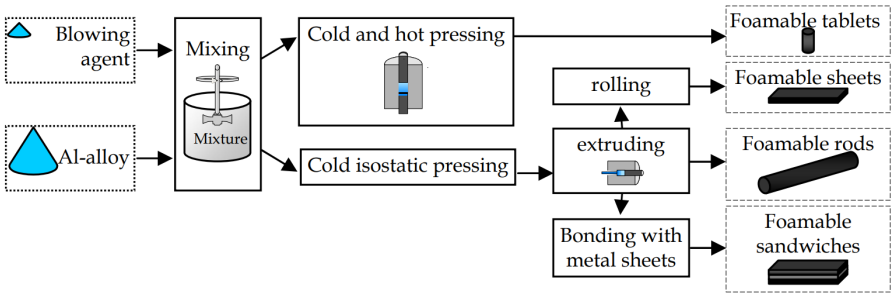

Figure A.2: Indirect foaming or powder metallurgy methods [102].

ple, in the car industry, is limited. Closed-cell foams can be used in sandwich panels and thin-walled structures for structural and energy absorbing components in vehicles, trains and airplanes, where low weight results in better efficiency, or in machines and protection elements.Other commercial, industrial and military applications are also possible [1, 22, 23].

A.1.2 Open-cell Foam Production

The production of open-cell foams is more limited, since they are unable to retain gases. They cannot be foamed, but can still be formed into foam-like structures through the utilization of a carrier, such as a polymer foam (sponge), a process called investment casting [1]. Therefore, the production of metal foams is usually performed without directly foaming the metal. Polymer foams are used as a starting point and the final obtained metal structure is identical to the used polymeric base. This method takes advantage of the quality of the polymer foams in terms of pore homogeneity and distribution, since the technology in that field is more advanced compared to metallic foams [1, 2].

Initially, the polymer foam is filled with a slurry of heat-resistant material, e.g., a mixture of mullite, phenolic resin and calcium carbonate. Afterwards, when it is dry, the polymer is decomposed and the result is a mould for the molten metal. Finally, the melt is introduced in the mould and the final foam is complete after cooling down. Open-cell foams exhibit increased thermal and electrical conductivities due to the network of pores and large surface area. For those reasons, they are used as heat exchangers, catalysts, filters and in biomedical applications as bone implants and prosthesis (usually in titanium and its alloys) [1, 34].

A.1.3 Influence of the Production Method on Pore Distribution

Different production methods have different levels of control and yield different foam structures and characteristics. Because of this, a classification system, proposed by Lehmus *et al.* [30], is introduced which differentiates these processes by the various levels of geometrical control. Closed-cell and open-cell or foams and sponges are not distinguished in this list. All types are included under the term “metal foam”:

1. **Stochastic Foams**
   (a) Melt foaming using blowing agents, gas introduction (uncontrolled);
   (b) Powder metallurgy using blowing agents.

2. **Partially Ordered Foams: Enhanced Structural Control**
   (a) Melt foaming using controlled gas introduction;
   (b) Melt foaming using solidification control;
   (c) Placeholder methods;
   (d) Precursor/replication methods;
   (e) APM foams;
   (f) Syntactic foams;
   (g) Placeholder methods with ordered assembly of placeholders;
   (h) Syntactic foams through ordered assembly of hollow particles;
   (i) Metal fibre structures.
3. **Ordered Foams: Ordered Assembly of Identical Structural Elements**
   (a) Kagome-type foams;
   (b) Corrugated sheet metal structures;
   (c) UniPore structure.
4. **Designed-to-Purpose Cellular Structures**
   (a) Additive manufacturing approaches.

Figure A.3 represents the previously mentioned classes based on the level of geometrical control. The distinction between classes is not always clear as there are processes that could be placed as an intermediate between two adjacent classes.

A.2 Otsu Thresholding Technique

The Otsu thresholding technique is used, in its primary form, to separate images with bimodal characteristics, i.e., images with two main peaks in the histogram and it works unsupervised, since no human interaction is needed to define any parameter [16]. Other types of thresholding techniques also exist, for example, multi-level thresholding [49], but aren't considered for the purpose of this dissertation.

The main version of the Otsu thresholding, which was implemented in *CTAn*, has the following formulation [48,103]. Letting the pixels of a given image (**I**) be represented in L grey levels, the number of pixels at level i denoted by n_i and the total number of pixels by $N = n_1 + n_2 + ...n_L$. The grey-scale histogram is normalised and regarded as a probability distribution:

$$p_i = \frac{n_i}{N}, \quad p_i \geq 0, \quad \sum_{i=1}^{L} p_i = 1. \tag{A.1}$$

The pixels are divided into 2 classes C_0 and C_1, i.e., background and foreground/object, divided by a threshold at level k. C_0 denotes the pixels with levels $[1, ..., k]$ and C_1

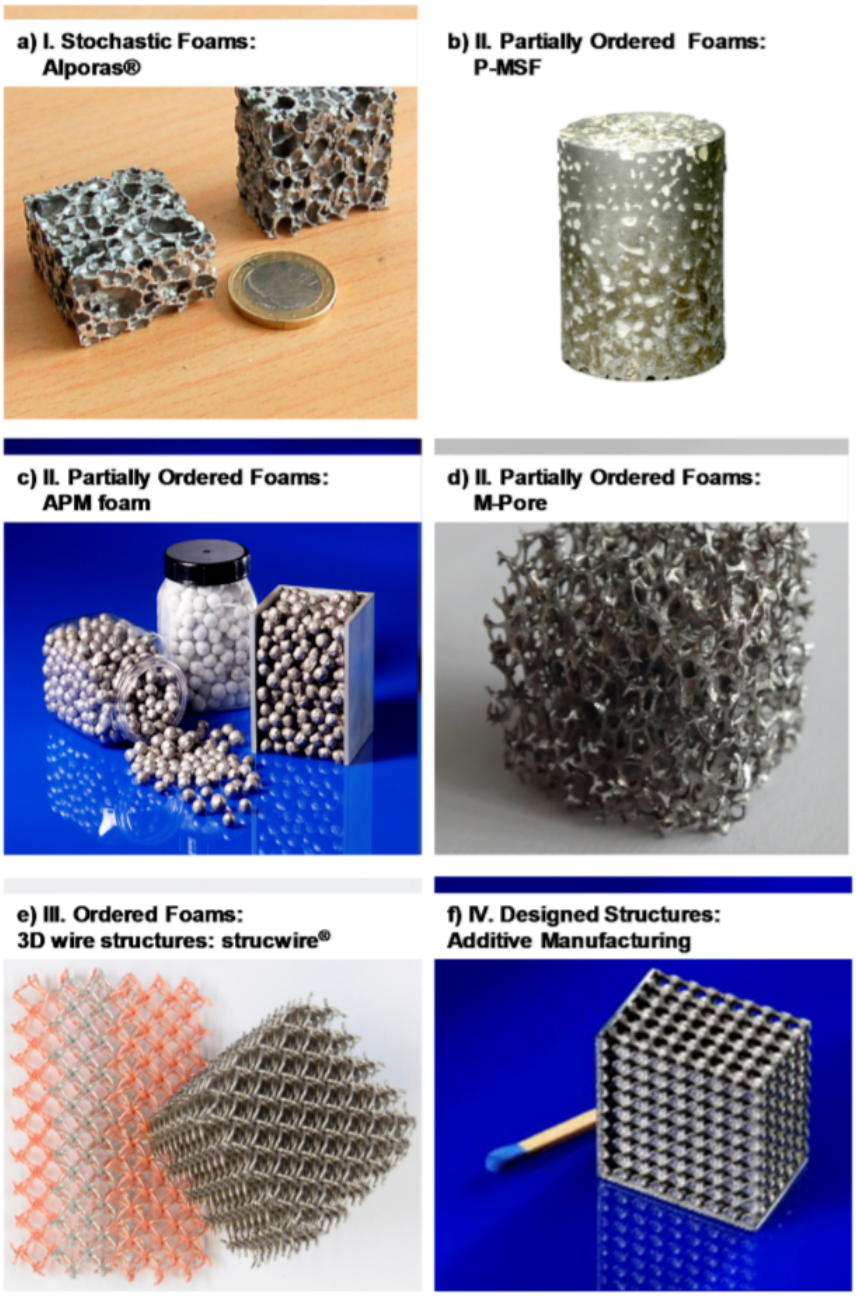

Figure A.3: Exemplary images of the different foams' classes, which illustrate the level of order and structural control [30]. a) Alporas foam; b) P-MSF foam; c) APM foam; d) M-Pore foam; e) Structwire; Additevely manufactured 3D lattice structure.

indicates pixels with levels $[k+1, ..., L]$. Then, the probability of a class occurring is given by

$$w_0 = \sum_{i=1}^{k} p_i = w(k), \tag{A.2}$$

$$w_1 = \sum_{i=k+1}^{L} p_i = 1 - w(k), \tag{A.3}$$

where w_0 is the probability of occurrence of class C_0 and w_1 the probability of C_1. The class mean levels are determined using

$$\mu_0 = \sum_{i=1}^{k} \frac{ip_i}{w_0} = \frac{\mu(k)}{w(k)}, \tag{A.4}$$

$$\mu_1 = \sum_{i=k+1}^{L} \frac{ip_i}{w_1}, \tag{A.5}$$

where μ_0 is the mean of class C_0 and μ_1 is the mean of class C_1.

$$w(k) = \sum_{i=1}^{k} p_i \tag{A.6}$$

$$u(k) = \sum_{i=1}^{k} ip_i \tag{A.7}$$

are the zero and first order cumulative moments of the histogram up to level k. The total mean level of the original picture is given by

$$\mu_{\mathrm{T}} = \mu(L) = \sum_{i=1}^{L} ip_i, \tag{A.8}$$

which can be verified, for any choice of k, by:

$$w_0\mu_0 + w_1\mu_1 = \mu_{\mathrm{T}}, \quad w_o + w_1 = 1. \tag{A.9}$$

Finally, the class variances are calculated as

$$\sigma_0^2 = \sum_{i=1}^{k} (i - \mu_0)^2 \frac{p_i}{w_0} \tag{A.10}$$

$$\sigma_1^2 = \sum_{i=k+1}^{L} (i - \mu_1)^2 \frac{p_i}{w_1} \tag{A.11}$$

To evaluate the threshold at a level k, the following discriminant criterion measures, i.e., measures of class separability, are introduced:

$$\lambda = \frac{\sigma_{\mathrm{B}}^2}{\sigma_{\mathrm{W}}^2}, \quad \kappa = \frac{\sigma_{\mathrm{T}}^2}{\sigma_{\mathrm{W}}^2}, \quad \eta = \frac{\sigma_{\mathrm{B}}^2}{\sigma_{\mathrm{T}}^2}, \tag{A.12}$$

where

$$\sigma_W^2 = w_0\sigma_0^2 + w_1\sigma_1^2, \tag{A.13}$$

$$\sigma_B^2 = w_0(\mu_0 - \mu_T)^2 + w_1(\mu_1 - \mu_T)^2 = w_0w_1(\mu_1 - \mu_0)^2, \tag{A.14}$$

due to Equation A.9 and

$$\sigma_T^2 = \sum_{i=1}^{L}(i - \mu_T)^2 p_i \tag{A.15}$$

are the within-class variance, the between-class variance and the total variance of levels, respectively. The problem of obtaining an ideal threshold k is reduced to an optimization problem that searches for a value of k which maximizes one of the criterions mentioned above. For a reason of simplicity, η is adopted to study the separability of the threshold, i.e., how well the classes are separated by the threshold. Therefore, the optimal threshold maximizes η or, equivalently, σ_B^2.

A.3 Equipment

A SkyScan 1275 scanner (Bruker μCT, Belgium) from TEMA (Centre for Mechanical Technology and Automation (TEMA), Department of Mechanical Engineering, Universidade de Aveiro) was used to obtain the scans used in this dissertation (Fig.A.4).

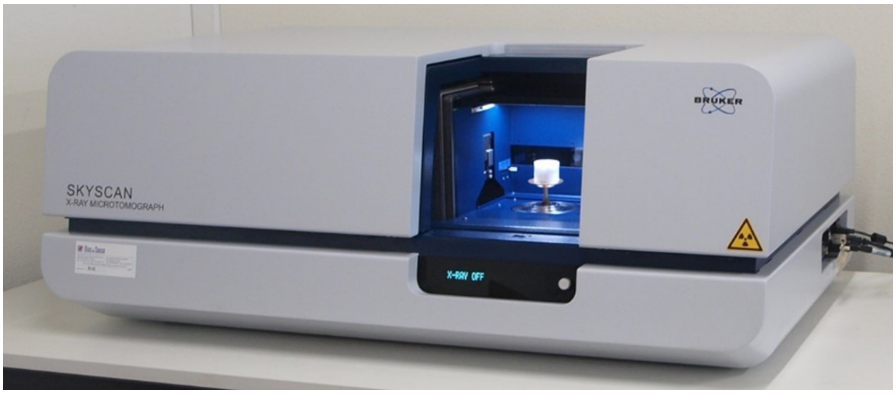

Figure A.4: SkyScan 1275 (Bruker μCT, Belgium) from TEMA.

A.4 Face Quality

The quality of a face of a 3D boundary mesh is calculated as [65]

$$\eta = K\frac{inscribed\ radius}{circumscribed\ radius}, \tag{A.16}$$

where inscribed radius is equal to the radius of the largest circumference that fits inside a triangle, circumscribed radius means the radius of the circumference that contains the triangle vertices and K has been chosen so that the equilateral triangle has $\eta = 1$, which is the preferred configuration of each face and that maximizes the relationship between radii (Fig. A.5).

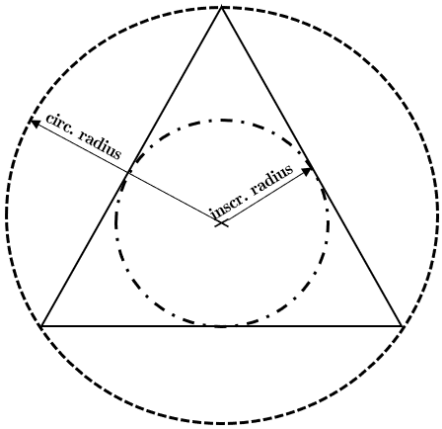

Figure A.5: Measurements for the quality factor [65].

A.5 Representative Unit-Cells (RUC)

Representative Unit-Cell (RUC) models try to recreate the different foams with a simplified structure which can be periodically repeated to construct foams of different sizes. For this reason, they are far less detailed than the models based on μCT scans, but are simpler and require less processing power. Eight different types of RUCs were considered in this work (Fig. A.6): Four for the closed cell-foams, Solid Closed Kelvin Cells (CL), Surface Kelvin cells, Solid Closed Weaire-Phelan (CL) cells and Surface Weaire-Phelan cells, and four for the open-cell foams, Solid Open Kelvin cells (OP), Wire Kelvin cells, Solid Open Weaire-Phelan (OP) cells and Wire Weaire-Phelan cells [19, 20, 96].

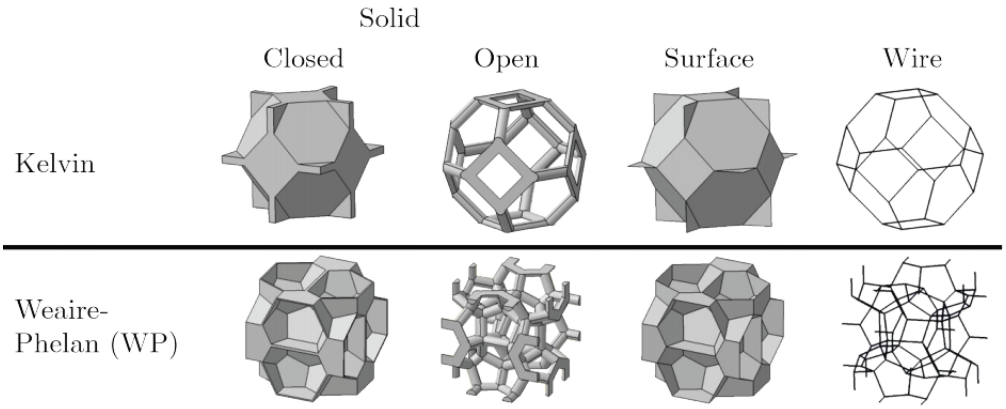

Figure A.6: Different types of representative unit-cells.

A.6 Marching Cubes 33

The Marching Cubes 33 algorithm (MC33) is an improved version of the Marching Cubes algorithm (MC) and is used for the reconstruction of isosurfaces from volumetric datasets, i.e., from 3D arrays of data [17, 57]. It uses the images obtained with the μCT

to create a surface representation.

This technique uses a divide-and-conquer approach to locate the surface in a logical cube from eight pixels, four from one 2D slice and four from another adjacent slice/image (Fig. A.7). The algorithm determines how the surface intersects this cube and then moves, marches, to the next cube. First, to find how the surface intersects the cubes, the vertices which have a data value equal or higher than the value of the surface are inside the surface and are assigned with a 1. Vertices with values below the surface are on the outside are assigned with a 0. Therefore, the surface intersects the cubes edges where one vertex is outside the surface and another is inside. With this assumption, the surface and the location of the intersection can be found by a linear interpolation. In addition, knowing there are eight vertices in a cube and two possible states for each cube, there can be 256 ways ($2^8 = 256$) a surface intersects a cube. For this reason, a look up table can be created to document all forms of intersection. Because of two symmetries of the cube, the number of patterns is reduced from 256 to 14.

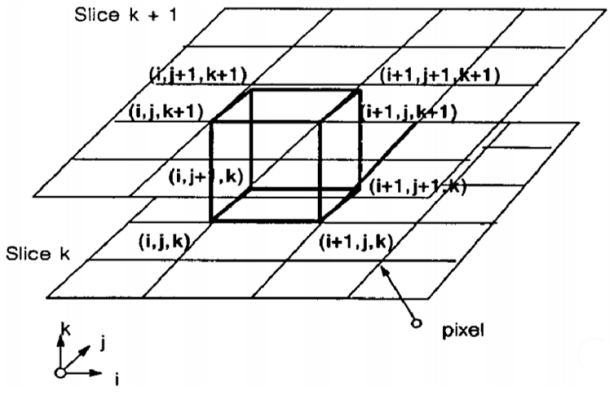

Figure A.7: Marching Cubes grid [57].

Up to this point, the MC and MC33 algorithms behave in the same manner, however, the latter uses a trilinear variation over the cube as an extension to the linear variation along an edge. Because of it, the look up table is constituted by 33 patterns (MC 33) instead of 14 (Fig. A.8). It manages to improve some problems regarding hole creation and takes into consideration internal and face ambiguities which are not considered by the original method, therefore, increasing the number of patterns, already considering the symmetries, to 33, hence the name [17].

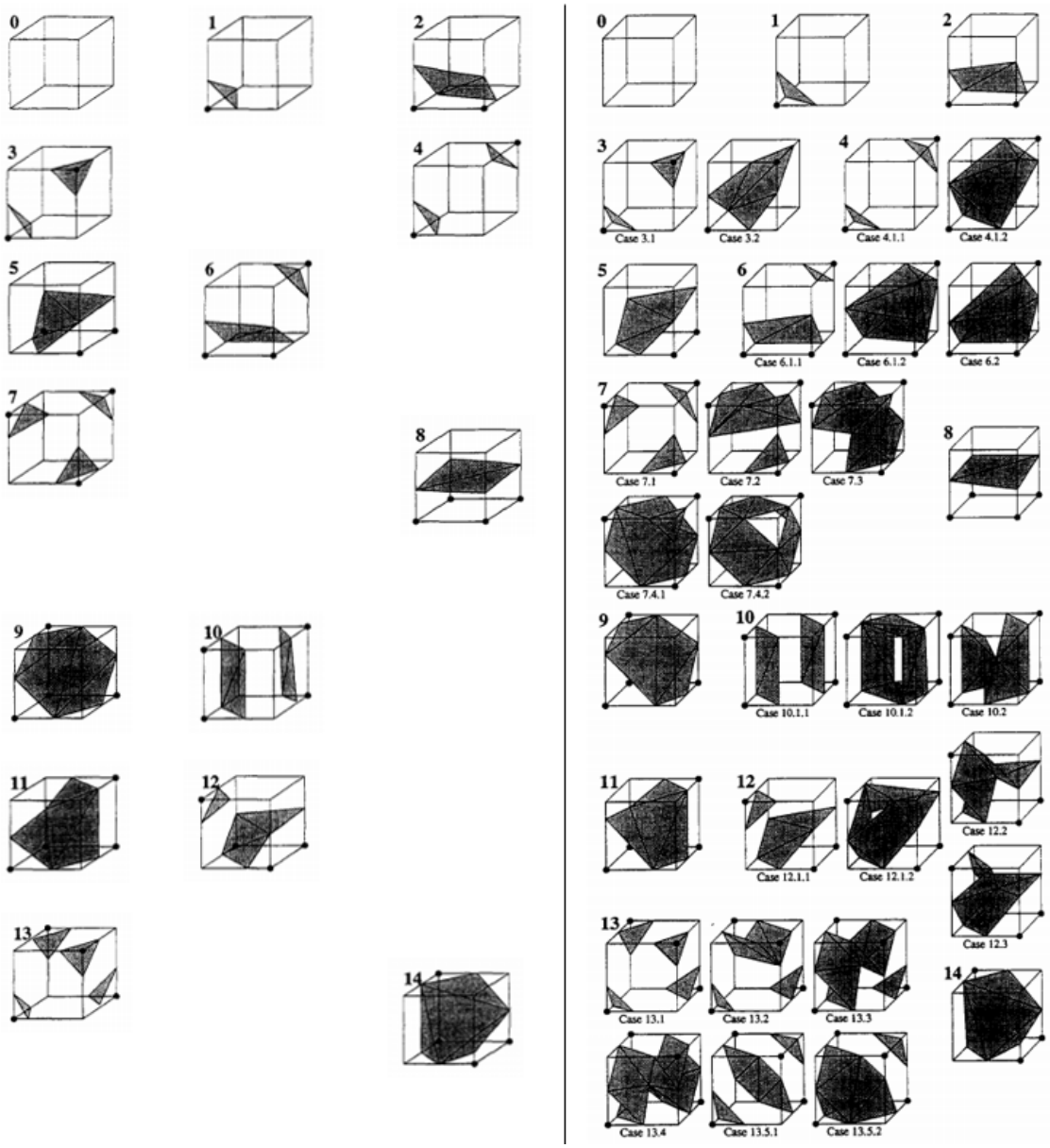

Figure A.8: Original look up table on the left (MC) and new MC33 look up table on the right [17].

Bibliography

[1] F. García-Moreno. Commercial applications of metal foams: Their properties and production. *Materials*, 9(2), 2016.

[2] J. Banhart. Manufacture, characterisation and application of cellular metals and metal foams. *Progress in Materials Science*, 46(6):559–632, 2001.

[3] H. Nakajima. Fabrication, properties and application of porous metals with directional pores. *Progress in Materials Science*, 52(7):1091–1173, 2007.

[4] J Banhart, J Baumeister, and M Weber. Powder Metallurgical Technology for the Production of Metallic Foams. Technical report, 1995.

[5] L. J. Gibson and M. F. Ashby. *Cellular solids: Structure and properties, second edition*. Cambridge University Press, 2014.

[6] A. C. Kak, M. Slaney, and G. Wang. Principles of Computerized Tomographic Imaging. *Medical Physics*, 29(1):107–107, 2002.

[7] V. Sharma, F. Zivic, N. Grujovic, N. Babcsan, and J. Babcsan. Numerical modeling and experimental behavior of closed-cell aluminum foam fabricated by the gas blowing method under compressive loading. *Materials*, 12(10), 2019.

[8] A. Chaturvedi, S. Bhatkar, P. S. Sarkar, S. Chaturvedi, and M. K. Gupta. 3D geometric modeling of aluminum based foam using micro computed tomography technique. *Materials Today: Proceedings*, 18:4151–4156, 2019.

[9] I. Kozma and I. Zsoldos. CT-based tests and finite element simulation for failure analysis of syntactic foams. *Engineering Failure Analysis*, 104:371–378, 2019.

[10] A. Ghazi, P. Berke, C. Tiago, and T. J. Massart. Computed tomography based modelling of the behaviour of closed cell metallic foams using a shell approximation. *Materials and Design*, 194:108866, 2020.

[11] Y. Hangai, R. Yamaguchi, S. Takahashi, T. Utsunomiya, O. Kuwazuru, and N. Yoshikawa. Deformation behavior estimation of aluminum foam by X-ray CT image-based finite element analysis. *Metallurgical and Materials Transactions A: Physical Metallurgy and Materials Science*, 44(4):1880–1886, 2013.

[12] D. Miedzińska, T. Niezgoda, and R. Gieleta. Numerical and experimental aluminum foam microstructure testing with the use of computed tomography. *Computational Materials Science*, 64:90–95, 2012.

[13] C. Veyhl, I. V. Belova, G. E. Murch, and T. Fiedler. Finite element analysis of the mechanical properties of cellular aluminium based on micro-computed tomography. *Materials Science and Engineering A*, 528(13-14):4550–4555, 2011.

[14] Y. Chen, R. Das, and M. Battley. Finite element analysis of the compressive and shear responses of structural foams using computed tomography. *Composite Structures*, 159:784–799, 2017.

[15] E. N. Landis and D. T. Keane. X-ray microtomography. *Materials Characterization*, 61(12):1305–1316, 2010.

[16] B. Leszczyński, A. Gancarczyk, A. Wróbel, M. Piątek, J. Łojewska, A. Kołodziej, and R. Pędrys. Global and Local Thresholding Methods Applied to X-ray Microtomographic Analysis of Metallic Foams. *Journal of Nondestructive Evaluation*, 35(2):1–9, 2016.

[17] E. V. Chernyaev. Marching Cubes 33: Construction of Topologically Correct Isosurfaces. In *GRAPHICON '95*, Saint-Petersburg, Russia, 1995. Protvino.

[18] P. Cignoni, C. Rocchini, and R. Scopigno. Metro: Measuring Error on Simplified Surfaces. *Computer Graphics Forum*, 17(2):167–174, 1998.

[19] J. Aquino, I. Duarte, and J. Dias-de-Oliveira. Modelling and effective properties prediction of metal foams. *Science and Technology of Materials*, 30(1):43–49, 2018.

[20] J. Aquino. Methods for the prediction of effective properties of metal foams. Technical report, University of Aveiro, 2016.

[21] L. J. Gibson and M. F. Ashby. *Cellular materials in nature and medicine*. Cambridge University Press, 2010.

[22] M. Garcia-Avila, M. Portanova, and A. Rabiei. Ballistic performance of composite metal foams. *Composite Structures*, 125:202–211, 2015.

[23] J. Marx, M. Portanova, and A. Rabiei. A study on blast and fragment resistance of composite metal foams through experimental and modeling approaches. *Composite Structures*, 194:652–661, 2018.

[24] H. P. Degischer and B. Kriszt. *Handbook of Cellular Metals - Production, Processing, Applications*. Wiley, 2002.

[25] I. Duarte, T. Fiedler, L. Krstulović-Opara, and M. Vesenjak. Brief Review on Experimental and Computational Techniques for Characterization of Cellular Metals. *Metals*, 10(6):726, 2020.

[26] M. Ashby, A. Evans, N. Fleck, L. Gibson, J. Hutchinson, H. Wadley, and F. Delale. Metal Foams: A Design Guide. *Applied Mechanics Reviews*, 54(6):B105–B106, 2001.

[27] J. Banhart and H. W. Seeliger. Aluminium foam sandwich panels: Manufacture, metallurgy and applications. *Advanced Engineering Materials*, 10(9):793–802, 2008.

[28] I. Duarte, M. Vesenjak, L. Krstulović-Opara, I. Anžel, and J. M. F. Ferreira. Manufacturing and bending behaviour of in situ foam-filled aluminium alloy tubes. *Materials and Design*, 66(PB):532–544, 2015.

[29] Haydn N.G. Wadley. Multifunctional periodic cellular metals. *Philosophical Transactions of the Royal Society A: Mathematical, Physical and Engineering Sciences*, 364(1838):31–68, 2006.

[30] D. Lehmhus, M. Vesenjak, S. de Schampheleire, and T. Fiedler. From stochastic foam to designed structure: Balancing cost and performance of cellular metals. *Materials*, 10(8), 2017.

[31] S. Hong, C. Sanchez, H. Du, and N. Kim. Fabrication of 3D Printed Metal Structures by Use of High-Viscosity Cu Paste and a Screw Extruder. *Journal of Electronic Materials*, 44(3):836–841, 2015.

[32] N. Gupta, S. E. Zeltmann, V. Shunmugasamy, and D. Pinisetty. Applications of polymer matrix syntactic foams. *JOM*, 66(2):245–254, 2014.

[33] B. Vengatachalam, R. Huang, L. H. Poh, Z. Liu, Q. Qin, and S. Swaddiwudhipong. Initial yield behaviour of closed-cell aluminium foams in biaxial loading. *International Journal of Mechanical Sciences*, 191:106063, 2021.

[34] I. Duarte, M. Vesenjak, L. Krstulović-Opara, and Z. Ren. Crush performance of multifunctional hybrid foams based on an aluminium alloy open-cell foam skeleton. *Polymer Testing*, 67:246–256, 2018.

[35] I. Duarte, M. Vesenjak, and M. J. Vide. Automated Continuous Production Line of Parts Made of Metallic Foams. *Metals*, 9(5):531, 2019.

[36] M. Vesenjak, I. Duarte, J. Baumeister, H. Göhler, L. Krstulović-Opara, and Z. Ren. Bending performance evaluation of aluminium alloy tubes filled with different cellular metal cores. *Composite Structures*, 234:111748, 2020.

[37] I. Duarte, N. Peixinho, A. Andrade-Campos, and R. Valente. Special Issue on Cellular Materials. *Science and Technology of Materials*, 30(1):1–3, 2018.

[38] M. F. Ashby. The properties of foams and lattices. *Philosophical Transactions of the Royal Society A: Mathematical, Physical and Engineering Sciences*, 364(1838):15–30, 2006.

[39] P. Viot, E. Plougonven, and D. Bernard. Microtomography on polypropylene foam under dynamic loading: 3D analysis of bead morphology evolution. *Composites Part A: Applied Science and Manufacturing*, 39(8):1266–1281, 2008.

[40] C. Appoloni, C. Fernandes, M. Innocentini, and Á. Macedo. Ceramic foams porous microstructure characterization by X-ray microtomography. *Materials Research*, 7(4):557–564, 2004.

[41] M. Saadatfar, F. Garcia-Moreno, S. Hutzler, A. P. Sheppard, M. A. Knackstedt, J. Banhart, and D. Weaire. Imaging of metallic foams using X-ray micro-CT. *Colloids and Surfaces A: Physicochemical and Engineering Aspects*, 344(1-3):107–112, 2009.

[42] N. Babcsan, S. Beke, G. Szamel, T. Borzsonyi, B. Szabo, R. Mokso, C. Kadar, and J. B. Kiss. Characterisation of ALUHAB Aluminium Foams with Micro-CT. *Procedia Materials Science*, 4:69–74, 2014.

[43] S. Calvo, D. Beugre, M. Crine, A. Léonard, P. Marchot, and D. Toye. Phase distribution measurements in metallic foam packing using X-ray radiography and micro-tomography. *Chemical Engineering and Processing: Process Intensification*, 48(5):1030–1039, 2009.

[44] O. B. Olurin, M. Arnold, C. Körner, and R. F. Singer. The investigation of morphometric parameters of aluminium foams using micro-computed tomography. *Materials Science and Engineering A*, 328(1):334–343, 2002.

[45] Bruker. Manual for Bruker-microCT CT-Analyser v. 1.13, 2013.

[46] W. Burger and M. J. Burge. *Digital Image Processing an Algorithmic Introduction Using Java*. Springer, 2016.

[47] J. Zhang, C. H. Yan, C. K. Chui, and S. H. Ong. Fast segmentation of bone in CT images using 3D adaptive thresholding. *Computers in Biology and Medicine*, 40(2):231–236, 2010.

[48] N. Otsu. A Threshold Selection Method from Gray-Level Histograms. *IEEE Transactions on Systems, Man, and Cybernetics*, 9(1):62–66, 1979.

[49] D. Y. Huang and C. H. Wang. Optimal multi-level thresholding using a two-stage Otsu optimization approach. *Pattern Recognition Letters*, 30(3):275–284, 2009.

[50] P Cignoni, M Callieri, M Corsini, M Dellepiane, F Ganovelli, and G Ranzuglia. MeshLab: An open-source mesh processing tool. In *6th Eurographics Italian Chapter Conference 2008 - Proceedings*, pages 129–136, 2008.

[51] C. C. Kai, G. Jacob, and T. Mei. Interface between CAD and rapid prototyping systems. Part 2: LMI - An improved interface. *International Journal of Advanced Manufacturing Technology*, 13(8):571–576, 1997.

[52] M. Szilvási-Nagy and G. Mátyási. Analysis of STL Files. In *Mathematical and Computer Modelling*, 2003.

[53] L. Piegl. On NURBS: A Survey. *IEEE Computer Graphics and Applications*, 11(1):55–71, 1991.

[54] K. S. Lee and S. H. Kim. Non-uniform deformation of an STL model satisfying error criteria. *CAD Computer Aided Design*, 42(3):238–247, 2010.

[55] K. F. Leong, C. K. Chua, and Y. M. Ng. A study of stereolithography file errors and repair. Part 1. Generic solution. *International Journal of Advanced Manufacturing Technology*, 12(6):407–414, 1996.

[56] K. F. Leong, C. K. Chua, and Y. M. Ng. A study of stereolithography file errors and repair. Part 2. Special cases. *International Journal of Advanced Manufacturing Technology*, 12(6):415–422, 1996.

[57] W. E. Lorensen and H. E. Cline. Marching cubes: A high resolution 3D surface construction algorithm. In *Proceedings of the 14th Annual Conference on Computer Graphics and Interactive Techniques, SIGGRAPH 1987*, pages 163–169, New York, New York, USA, aug 1987. Association for Computing Machinery, Inc.

[58] H. Hoppe. New quadric metric for simplifying meshes with appearance attributes. In *Proceedings of the IEEE Visualization Conference*, pages 59–66. IEEE, 1999.

[59] M. Garland and P. S. Heckbert. Surface simplification using quadric error metrics. In *Proceedings of the 24th Annual Conference on Computer Graphics and Interactive Techniques, SIGGRAPH 1997*, 1997.

[60] J. Rossignac and P. Borrel. Multi-resolution 3D approximations for rendering complex scenes. In *Modeling in Computer Graphics*, pages 455–465. Springer Berlin Heidelberg, 1993.

[61] W. J. Schroeder, J. A. Zarge, and W. E. Lorensen. Decimation of triangle meshes. In *Proceedings of the 19th annual conference on Computer graphics and interactive techniques - SIGGRAPH '92*, pages 65–70, New York, New York, USA, 1992. Association for Computing Machinery (ACM).

[62] Y. Li and Q. Zhu. A new mesh simplification algorithm based on quadric error metrics. In *Proceedings - 2008 International Conference on Advanced Computer Theory and Engineering, ICACTE 2008*, pages 528–532, 2008.

[63] G. Taubin. A Signal Processing Approach To Fair Surface Design. *Signal Processing*, 1995.

[64] G. Taubin. Curve and surface smoothing without shrinkage. *IEEE International Conference on Computer Vision*, pages 852–857, 1995.

[65] J. F. Remacle, C. Geuzaine, G. Compère, and E. Marchandise. High-quality surface remeshing using harmonic maps. *International Journal for Numerical Methods in Engineering*, 83(4):403–425, 2010.

[66] M. Meyer, M. Desbrun, P. Schröder, and A. H. Barr. Discrete Differential-Geometry Operators for Triangulated 2-Manifolds. In *Visualization and Mathematics III*, pages 35–37. Springer, 2003.

[67] H. Borouchaki and P. J. Frey. Simplification of surface mesh using Hausdorff envelope. *Computer Methods in Applied Mechanics and Engineering*, 194(48-49):4864–4884, 2005.

[68] I. Duarte, M. Vesenjak, and L. Krstulović-Opara. Variation of Quasi-static and Dynamic Compressive Properties in Single Aluminium-alloy Foam Block. *Procedia Materials Science*, 4:157–162, 2014.

[69] R. Chan and M. Nakamura. Mechanical Properties of Plastic Foams. *Journal of Cellular Plastics*, 5(2):112–118, 1969.

[70] J. M. Lederman. The prediction of the tensile properties of flexible foams. *Journal of Applied Polymer Science*, 15(3):693–703, 1971.

[71] P. Barma, M. B. Rhodes, and R. Salovey. Mechanical properties of particulate-filled polyurethane foams. *Journal of Applied Physics*, 49(10):4985–4991, 1978.

[72] G. Menges and F. Knipschild. Estimation of mechanical properties for rigid polyurethane foams. *Polymer Engineering and Science*, 15(8):623–627, 1975.

[73] W. E. Warren and A. M. Kraynik. The linear elastic properties of open-cell foams. *Journal of Applied Mechanics, Transactions ASME*, 55(2):341–346, 1988.

[74] R. M. Christensen. Mechanics of low density materials. *Journal of the Mechanics and Physics of Solids*, 34(6):563–578, 1986.

[75] W. E. Warren and A. M. Kraynik. Foam mechanics: the linear elastic response of two-dimensional spatiallly periodic cellular materials. *Mechanics of Materials*, 6(1):27–37, 1987.

[76] A. N. Gent and A. G. Thomas. The deformation of foamed elastic materials. *Journal of Applied Polymer Science*, 1(1):107–113, 1959.

[77] W.L. Ko. Deformations of Foamed Elastomers. *Journal of Cellular Plastics*, 1(1):45–50, 1965.

[78] W. Voigt. Ueber die Beziehung zwischen den beiden Elasticitätsconstanten isotroper Körper. *Annalen der Physik*, 274(12):573–587, 1889.

[79] A. Reuss. Berechnung der Fließgrenze von Mischkristallen auf Grund der Plastizitätsbedingung für Einkristalle . *ZAMM - Zeitschrift für Angewandte Mathematik und Mechanik*, 9(1):49–58, 1929.

[80] J. Dias-de-Oliveira. Modelação Micromecânica do Comportamento de Materiais Compósitos de Matriz de Alumínio. Technical report, University of Aveiro, 2006.

[81] A. G. Dement'ev and O. G. Tarakanov. Effect of cellular structure on the mechanical properties of plastic foams. *Polymer Mechanics*, 6(4):519–525, 1970.

[82] W. E. Warren and A. M. Kraynik. Linear elastic behavior of a low-density kelvin foam with open cells. *Journal of Applied Mechanics, Transactions ASME*, 64(4):787–794, 1997.

[83] H. X. Zhu, J. F. Knott, and N. J. Mills. Analysis of the elastic properties of open-cell foams with tetrakaidecahedral cells. *Journal of the Mechanics and Physics of Solids*, 45(3):319–325, 1997.

[84] G.W. Renz, R., Ehrenstein. Calculation of deformation of cellular plastics by applying the finite element method. *Cellular Polymers*, pages 1:5–13, 1982.

[85] R. M. Christensen. Mechanics of cellular and other low-density materials. *International Journal of Solids and Structures*, 37(1-2):93–104, 2000.

[86] N. J. Mills and H. X. Zhu. The high strain compression of closed-cell polymer foams. *Journal of the Mechanics and Physics of Solids*, 47(3):669–695, 1999.

[87] C. Chen, T. J. Lu, and N. A. Fleck. Effect of imperfections on the yielding of two-dimensional foams. *Journal of the Mechanics and Physics of Solids*, 47(11):2235–2272, 1999.

[88] A. P. Roberts and E. J. Garboczi. Elastic moduli of model random three-dimensional closed-cell cellular solids. *Acta Materialia*, 49(2):189–197, 2001.

[89] Y. X. Gan, C. Chen, and Y. P. Shen. Three-dimensional modeling of the mechanical property of linearly elastic open cell foams. *International Journal of Solids and Structures*, 42(26):6628–6642, 2005.

[90] A. E. Simone and L. J. Gibson. Effects of solid distribution on the stiffness and strength of metallic foams. *Acta Materialia*, 46(6):2139–2150, 1998.

[91] E. Marchandise, G. Compère, M. Willemet, G. Bricteux, C. Geuzaine, and J. F. Remacle. Quality meshing based on STL triangulations for biomedical simulations. *International Journal for Numerical Methods in Biomedical Engineering*, 26(7):876–889, 2010.

[92] Helmut J. Bohm. A Short Introduction to Basic Aspects of Continuum Micromechanics. *Composites*, 1998.

[93] M. Kirca, A. Gül, E. Ekinci, F. Yardim, and A. Mugan. Computational modeling of micro-cellular carbon foams. *Finite Elements in Analysis and Design*, 44(1-2):45–52, 2007.

[94] W. Y. Jang, W. Y. Hsieh, C. C. Miao, and Y. C. Yen. Microstructure and mechanical properties of ALPORAS closed-cell aluminium foam. *Materials Characterization*, 107:228–238, 2015.

[95] F. Triawan, K. Kishimoto, T. Adachi, K. Inaba, T. Nakamura, and T. Hashimura. The elastic behavior of aluminum alloy foam under uniaxial loading and bending conditions. *Acta Materialia*, 60(6-7):3084–3093, 2012.

[96] T. Daxner, R. Bitsche, and H. J. Böhm. Space-Filling Polyhedra as Mechanical Models for Solidified Dry Foams. *Materials Transactions*, 47:2213–2218, 2006.

[97] N. Dowling. *Mechanical Behavior of Materials - Engineering Methods for Deformation, Fracture and Fatigue*. Pearson Education, 4 edition, 2012.

[98] J. Banhart. Metal foams: Production and stability. *Advanced Engineering Materials*, 8(9):781–794, 2006.

[99] F. Von Zeppelin, M. Hirscher, H. Stanzick, and J. Banhart. Desorption of hydrogen from blowing agents used for foaming metals. *Composites Science and Technology*, 63(16):2293–2300, 2003.

[100] I. Duarte and J. Banhart. A study of aluminium foam formation - Kinetics and microstructure. *Acta Materialia*, 48(9):2349–2362, 2000.

[101] F. Baumgärtner, I. Duarte, and J. Banhart. Industrialization of Powder Compact Toaming Process. *Advanced Engineering Materials*, 2(4):168–174, 2000.

[102] I. Duarte and M. Oliveira. Aluminium Alloy Foams: Production and Properties. In Katsuyoshi Kondoh, editor, *Powder Metallurgy*. InTech, 2012.

[103] T. Y. Goh, S. N. Basah, H. Yazid, M. J. Aziz Safar, and F. S. Ahmad Saad. Performance analysis of image thresholding: Otsu technique. *Measurement: Journal of the International Measurement Confederation*, 114:298–307, 2018.